Alma Mater Studiorum · Università di Bologna

SCUOLA DI SCIENZE

Corso di Laurea in Fisica del Sistema Terra

ANALYSIS OF A MESOSCALE CYCLONE IN THE ADRIATIC SEA

Relatore:
Prof.
Vincenzo Levizzani

Correlatore:
Prof.
Mario Marcello Miglietta

Presentata da:
Federico Buscemi

Sessione II
Anno Accademico 2020/2021

Abstract

In the evening of November 12, 2019, an exceptional high tide - the second most intense since sea level data are recorded - hit the city of Venice and the entire lagoon, flooding and damaging a large part of the historical center. The causes of this event are due to a small mesoscale cyclonic structure characterized by a warm core, grown in the central Adriatic, which, moving towards the Northwest, strengthened and passed over the Venice lagoon. The passage of the cyclone was anticipated by intense Bora, which turned into Sirocco first and Libeccio afterward, causing the sudden rise of the sea level in the lagoon. This work investigates the factors that determined the development of the cyclone, as well as the characteristics of its particular structure. For this purpose, simulations were carried out with the WRF-ARW model, with initial and boundary conditions supplied by the global GFS model. Three simulations with different starting times were performed, each initialized with a different analysis of the GFS model. The results were compared on the basis of the prediction of the minimum sea level pressure value and of the trajectory of the cyclone. The simulation whose results are closest to the data observed by the meteorological stations is identified, and the factors that have contributed the most to the development of the cyclone are searched for. The interaction between a strong potential vorticity anomaly at 300 hPa and the advection of warm, humid air in the lower layers was the main factor responsible for the cyclone development. The pre-existence of positive cyclonic vorticity, resulting from the convergence of the Sirocco and Bora winds in the northern Adriatic, also made the environment favorable to

the cyclone development. Therefore it appears as the cyclone developed by a baroclinic instability process typical of extra-tropical cyclones, but with much smaller dimensions and characteristics.

Sommario

La sera del 12 Novembre 2019 un'alta marea eccezionale - la seconda più intensa da quando si raccolgono i dati del livello del mare - ha colpito la città di Venezia e l'intera laguna, inondando e danneggiando buona parte del centro storico. Le cause di questo evento di portata storica sono da imputare a una piccola struttura ciclonica alla mesoscala a cuore caldo, nata sul medio Adriatico, che, spostandosi verso Nordovest, si è rinforzata ed è transitata sulla laguna di Venezia. In laguna, il passaggio del ciclone è stato anticipato da intensi venti di Bora, poi ruotati a Scirocco prima e Libeccio in un secondo tempo, provocando l'innalzamento repentino del livello dell'acqua in laguna. In questo lavoro si sono ricercati i fattori che hanno determinato la nascita e lo sviluppo del ciclone, nonché le caratteristiche di questa struttura particolare. A tal fine sono state svolte simulazioni con il modello WRF-ARW, con dati iniziali e al contorno forniti dal modello globale GFS. Sono state svolte tre simulazioni con diverso orario di inizio, ciascuna inizializzata con una diversa analisi del modello GFS. I risultati sono stati confrontati sulla base della previsione del valore minimo di pressione sul livello del mare e della traiettoria del ciclone. È stata individuata la simulazione i cui risultati si avvicinano maggiormente ai dati osservati, e vengono ricercati i fattori che hanno concorso maggiormente allo sviluppo del ciclone. L'interazione tra una forte anomalia di vorticità potenziale a 300 hPa e l'avvezione di aria calda e umida nei bassi strati è stato il fattore principale responsabile dello sviluppo del ciclone. La pre-esistenza di vorticità ciclonica positiva, scaturita dalla convergenza dei venti di Scirocco e Bora sul Nord Adriatico, ha reso inoltre l'ambiente

favorevole allo sviluppo del ciclone. Quindi esso appare come un ciclone nato da un processo di instabilità baroclina tipico dei cicloni extra-tropicali, ma con dimensioni molto ridotte e caratteristiche atipiche.

Contents

List of Figures

List of Figures

Introduction

In recent years the word *extreme* has been widely used and abused in meteorology, especially after the mediatic boom that this matter has been experiencing in recent years, due to the increasingly sensible effects of climate change on every day life. However, the word *extreme* does not seem completely out of context in the November 12, 2019 floods that affected Venice municipality and its lagoon. *Extreme* was the high tide that hits the city of Venice, with 189 cm of sea level reached at Punta della Salute - Canale della Giudecca (CPSM et al., 2020), the second highest value since the data are collected. *Extreme* were also the damages that unfortunately the city center of Venice experienced in this event. Although the adjective *extreme* may be excessive to describe the atmospheric conditions that characterized the event, certainly the adjective *rare* looks suitable in the description of the cyclonic structure analysed in this work.

Violent phenomena associated with cyclonic systems are not unusual in the Mediterranean area. For example, tropical-like cyclones or medicanes, small-scale warm core cyclonic systems self-sustained by heat and moisture fluxes from the sea surface and latent heat released by convection (Miglietta and Rotunno, 2019), occasionally occur in the Mediterranean; also, large extra-tropical cyclones sometimes undergo explosive cyclogenesis, causing widespread damage (e.g. Vaia storm (Davolio et al., 2020)). For the Adriatic Sea in particular, Horvath et al. (2008) grouped the cyclones in different categories, depending on their origin and evolution. However, the characteristics and dynamics that led to the formation and deepening, as well as the trajectory of the

November 12, 2019 case do not appear so common in the Adriatic Sea.

The cyclone under study appears as a hybrid cyclone, with a warm core confined in the low levels and a cold upper level trough. As it is discussed in the following, the mechanisms that determined its formation are those typical of the baroclinic instability, which characterizes extra-tropical cyclones. However, the warm core and the reduced scale of the cyclone are more typical characteristics of tropical-like structures that are occasionally observed in the Mediterranean area. Furthermore, the trajectory assumed in its development phase does not fit the classification proposed by Horvath et al. (2008) for Adriatic cyclogenesis.

For these reasons it was decided to study this cyclone more in depth. The determination of the development mechanism and the study of the characteristics of the cyclone represent the aim of the present study. By carrying out the simulations with the WRF-ARW model it was also possible to evaluate the predictability of a cyclone of this type. Surely there is still a long way to proceed in this field, especially as regards the initial and boundary data provided to limited area models, which, despite the increasingly high resolutions reached in the recent years, still face with problems in the difficult prediction of such small structures. Although the model skill was generally appropriate for the simulation of the cyclone from a meteorological perspective (cyclone track missed by few tens of km and depth underestimated by few hPa), it is not sufficient in terms of impact. In fact, even a small deviation of the track or an underestimation of the cyclone depth may deeply affect the simulation of the wave and tide, with dramatic consequences in terms of costs and impact to human activities.

Such considerations make clear the need for a progress in terms of prediction of the impact of the cyclone, which will be possible only integrating the atmospheric modelling with the ocean and wave modeling system, so that all the different forcings are kept together in a unified framework. The work is introduced by chapters 1 and 2, which consist respectively of an overview of cyclones, both of tropical and extra-tropical type,

and of a general look to the characteristics of the numerical weather prediction models; in chapter 3, models and data used in the work are described, including the tools for post-processing; the analysis is presented in chapters 4 and 5: in chapter 4 observations are analysed, while in chapter 5 the control simulations and sensitivity tests are examined. After studying more specifically the fields related to convection and the role of vorticity, in chapter 6 the results are commented and the conclusions of the work are drawn.

Chapter 1

Cyclones

A *cyclone* is a region of the atmosphere in which pressure values are lower than those of the surrounding regions at the same level. It is represented on a synoptic chart as a set of isobars at a specified altitude level (or a set of isolines of geopotential height at a specified pressure level) which enclose relatively low values of pressure (or altitude) (World Meteorological Organization WMO, 1992). In a cyclone, air flows around the pressure minimum counterclockwise in the Northern Hemisphere, clockwise in the Southern Hemisphere.

Many different dynamical mechanisms contribute to the formation of cyclones. Thus, they are classified into several families with respect to the formation dynamics and their physical features.

In this chapter the main classifications of cyclones and their structure will be analysed. The first part will deal with large-scale extratropical weather systems and their associated mesoscale fronts. In the second part a particular form of cyclone typical of the Tropics, i.e. the tropical cyclones, is discussed.

1.1 Extratropical Cyclones

Extratropical cyclones are large rotating weather systems that occur in the extratropics (north of 30°N in the Northern Hemisphere). They take on a great variety of forms, depending on factors such as the background flow in which they are embedded, the availability of moisture and the characteristics of the underlying surface (Wallace and Hobbs, 2006).

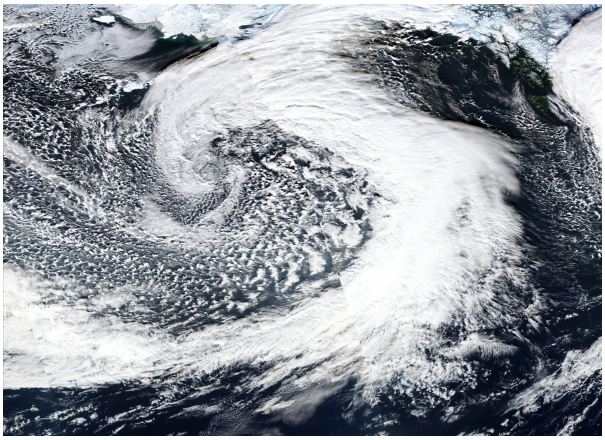

Figure 1.1: *Extratropical cyclone near the Gulf of Alaska - December 14, 2018 (NASA, 2018)*

It is rare to observe these systems on synoptic maps or in satellite images as simple circular vortices (Figure 1.1). In fact, they generally appear highly asymmetric in shape, with the most intense winds and temperature gradients concentrated along narrow bands called *fronts*. Furthermore, these systems are generally *baroclinic*. An atmosphere in which density depends on both the temperature T and the pressure p, $\rho = \rho(p, T)$, is referred to as a *baroclinic atmosphere*. In a baroclinic atmosphere the geostrophic wind generally has a vertical shear, and this shear is related to the horizontal temperature gradient by the *thermal wind equation*:

$$\frac{\partial \mathbf{V_g}}{\partial \ln p} = -\frac{R}{f}\,\mathbf{k} \times \nabla_{\mathbf{p}} T \tag{1.1}$$

where $\mathbf{V_g} = (u_g, v_g)$ is the geostrophic wind vector, p is the pressure, R is the ideal gas

constant for dry air, f is the Coriolis parameter, $\mathbf{k}$ is the unit vertical vector, $\nabla_{\mathbf{p}} T$ is the horizontal gradient of air temperature along an isobaric surface (Holton, 1992). In such an atmospheric background, the amplitudes and phases of the geopotential perturbations and the velocity of flows both vary with altitude. This complexity is partly due to the presence of a mean flow that varies slowly at planetary scales and which is itself highly baroclinic.

Furthermore, this planetary-scale flow is influenced by orography and contrasts caused by differences in temperature between continents and oceans, so that it is strongly longitude dependent. Figure 1.2 shows this characteristic, as it represents the 1958-1997 mean zonal wind at 200 hPa level for the winter period in the Northern Hemisphere: two wind maxima (*jets*) can be found east of the Asian and Northern American continents, remarking the influence of the orography on the zonal wind.

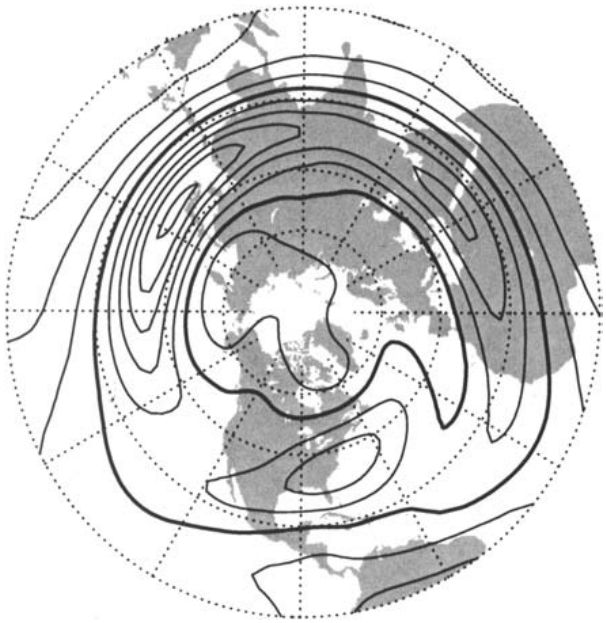

Figure 1.2: *Mean zonal wind at the 200 hPa level for December-February averaged for years 1958-1997. Contour interval 10 m s^{-1} (heavy contour, 20 m s^{-1}). (Based on NCEP/NCAR reanalyses; as cited in Holton (2004))*

Since the mean zonal wind and temperature fields satisfy the thermal wind relationship (Equation 1.1), the maximum zonal wind speed in the Northern Hemisphere is much larger in the winter than in the summer. Looking vertically at the troposphere, the maximum of the zonal wind lies below the tropopause (the boundary between the troposphere and the stratosphere) at the latitude where the integrated thermal wind over the whole troposphere is maximum.

In both hemispheres it is located between 30° and 35° of latitude during winter, and between 40° and 45° during summer (Holton, 1992).

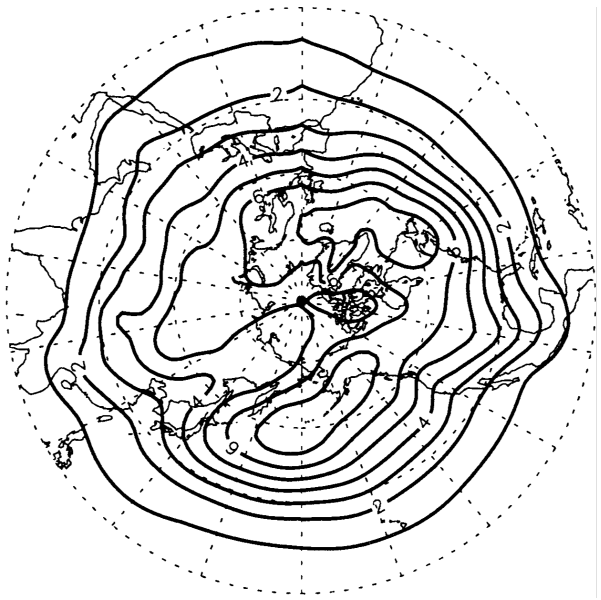

Figure 1.3: *Bandpass statistics from the NCEP-NCAR reanalysis. Standard deviations of SLP (contour 1 hPa). (Chang et al., 2002)*

Synoptic-scale disturbances tend to develop preferentially in the regions of maximum time-mean zonal winds and to propagate downstream along storm tracks that approximately follow the jet axes, as it can be seen in Figure 1.3. Higher numbers indicate higher variances in sea level pressure, i.e. regions where the passage of cyclones occurs more frequently.

It is a common observation in fluid dynamics that jets in which strong velocity shears occur may be unstable with respect to small perturbations. Hence, any small disturbances introduced into the jet will tend to amplify, taking energy from the jet as it grows. Most synoptic-scale systems in mid-latitudes appear to evolve as the result of an instability of the jet stream flow. This instability, called *baroclinic instability*, depends on the meridional temperature gradient, particularly at the surface. Hence, through the thermal wind relationship (Eq. 1.1), baroclinic instability depends on vertical shear and tends to occur in the region of the polar frontal zone.

The atmospheric setup created in the upper troposphere by the jet stream features and the consequent divergence of the flows, determines a response from the lower levels, i.e. a convergence develops underneath. The phases that determine the formation of a

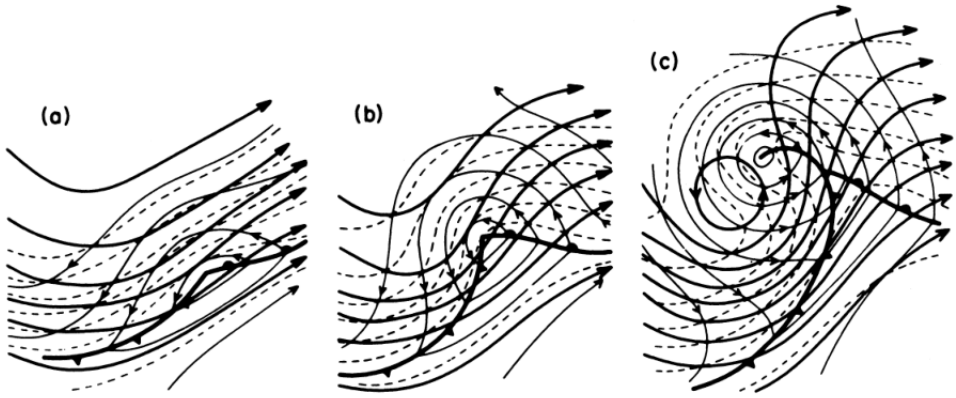

Figure 1.4: *500 hPa contours (heavy solid lines), 1000 hPa contours (thin lines) and 1000-500 hPa thickness (dashed lines) for a developing baroclinic cyclone (Holton, 1992).*

typically baroclinic cyclone are shown in figure 1.4. In the development phase of the cyclone, the interaction between the flow of the upper levels and of the lower levels takes place; there is a strong cold advection west of the trough in the lower levels, with a weaker warm advection to the east. The zones of thermal discontinuity correspond to the warm and cold fronts, rotating around the cyclone.

Cold fronts tend to be faster, mainly due to the higher density of cold air which pushes away warmer air from the lower levels. This fast movement increases convergence along the front; furthermore, the slope of a cold front is greater. This results in a more vertical motion and deep convection, with precipitations most often located along and ahead of the cold front boundary, since the strongest lifting is near the cold front boundary. While it is not always the case, there is a reduction of precipitations behind a cold front. *Warm fronts*, in contrast to the behaviour of heavier colder air, tend to move slower above colder air, mixing out the very shallow cool air at the warm front surface boundary. It is a slower process for warm air to erode cooler air than it takes for cold air to undercut warm air, thus warm fronts tend to move slower than cold fronts. Since warm air is less dense than cooler air, warm air easily lifts over the top of the slope of cooler air (*isentropic lifting*). Thus, clouds and widespread moderate precipitations are common in the region

preceding the surface warm front passage, where the cool air is located. Because of the different velocity, the cold front overtakes the warm front over time. The front, produced as a result of this process, is called *occluded front*. In such a situation, the cold front overtakes the two air masses that make up the warm front environment. In the warm front, warm air is advected over cool air. When the occluded front overtakes the warm front environment, the occluded front will lift above both of these air masses.

Figure 1.5 shows the occluded, cold and warm fronts. The occluded front is the front closest to the low pressure center. As the occluded front matures, the cold and warm fronts will lose their identity once they are too far from the low center and what will remain is a weakening low center along with an occluded front. There is often precipitation along an occluded front from cumulonimbus or nimbostratus clouds. Wind changes direction as the front passes and the temperature either warms or cools. After the cold front passes, the sky is usually clearer, and the air is drier.

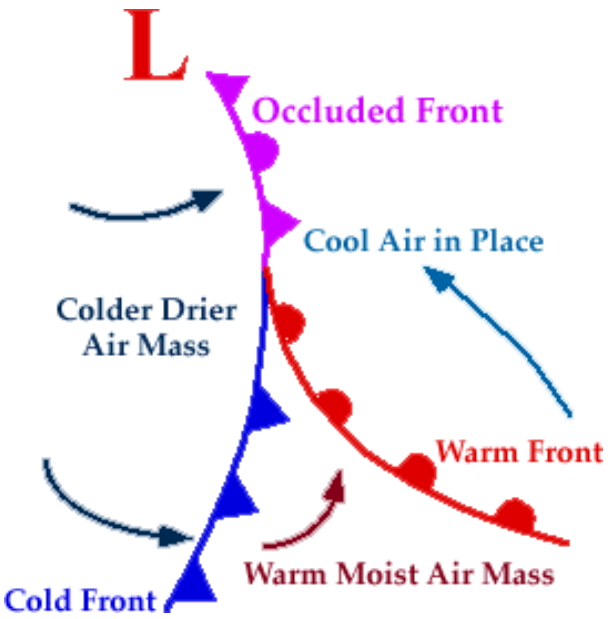

Figure 1.5: *Fronts associated to an extratropical cyclone. [University of Illinois, 2010]*

Turning back to the second drawing of figure 1.4, the southerly wind component to the east of the low advects warm air northward while the northerly component to the west of the low advects colder air southward. The strengthening of the east-west temperature contrasts in the lower tropospheric temperature field leads to a weakening of the North-South temperature gradient in the background field on which the wave is

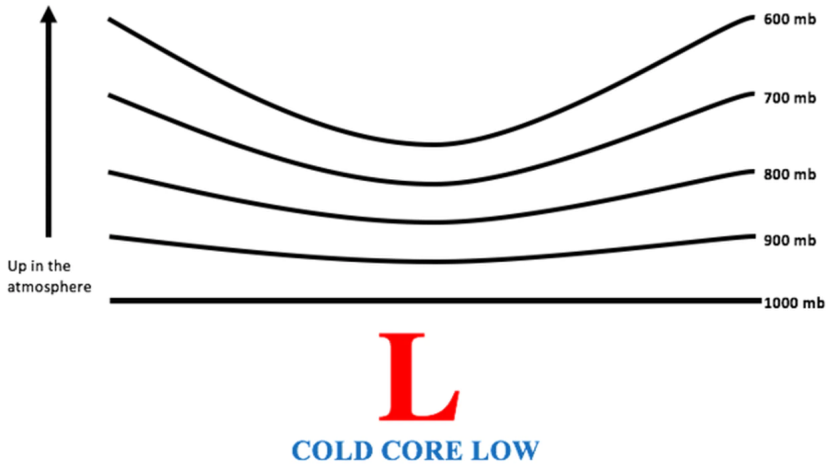

Figure 1.6: *Schematic representation of a cold core low cross section. (Reardon, 2016)*

growing. As the surface low intensifies, the winds around it strengthen, resulting in a considerable rise in horizontal temperature advection. In the last phase of development, the surface low aligns with the trough at 500 hPa, and the 1000 hPa height, the 500 hPa height and the 1000-500 hPa thickness contours come into alignment with each other, resulting in a weakening of the horizontal temperature advection. We therefore move from a strongly baroclinic pattern to a more *barotropic* one. This transition from a situation with strong thermal contrasts near to the surface low to one with weaker temperature gradients, marks the end of the intensification phase in the life of a cyclone.

Extratropical cyclones are characterized by an upper-level cold core. This is justified by the relationship between geopotential and temperature in the hypsometric equation:

$$\frac{\partial \Phi}{\partial p} = \frac{-RT}{p} \tag{1.2}$$

where Φ is the geopotential, whose variation with respect to pressure is directly proportional to the temperature T (Wallace and Hobbs, 2006). What derives from equation 1.2

can be observed in figure 1.6, in which the cross section of an extratropical cyclone is schematically represented. At the center of the cyclone the constant pressure curves are closer to each other. From equation 1.2 we deduce that the thickness of an atmospheric layer is directly proportional to the mean temperature of the layer, therefore a smaller thickness means colder air in the core of an extratropical cyclone.

1.2 Tropical cyclones

Tropical cyclones are smaller in scale and more axi-symmetric than their extratropical counterparts and tend to be longer lived and more intense. Tropical cyclones with wind gusts that exceed 32 m s^{-1} are also called *hurricanes* or *typhoons*, depending on the region where they formed; those characterized by wind gusts between 17 and 32 m / s are classified as *tropical storms*; those with weaker winds are classified as *tropical depressions*. A tropical cyclone is characterized by a warm core with relatively calm winds, free of deep convective clouds, surrounded by a wall of rapidly rotating clouds (Wallace and Hobbs, 2006).

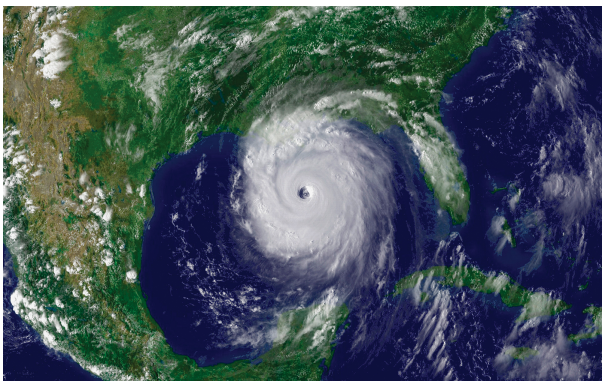

Figure 1.7: *Satellite image of hurricane Katrina, one of the strongest hurricanes to ever hit the USA coasts. (NOAA, 2005)*

In contrast to extratropical cyclones, which derive their potential energy from the ambient meridional temperature gradient, tropical cyclones derive their potential energy through latent and sensitive heat fluxes at the air-sea interface. They develop from mesoscale convective systems and acquire a rotational component in cyclostrophic balance with the pressure field.

The extraordinary pressure values

recorded in the eye of a tropical cyclone at the lower tropospheric levels are due to the warm - and consequently low density - overlying air. In figure 1.7 a satellite image of hurricane Katrina is shown. *Katrina* deepened in the Gulf of Mexico and hit the USA coasts in August 2005, causing a great deal of damage and unfortunately also many deaths in the affected states. A characteristic of tropical cyclones - that can also be observed from satellite - is the eye that distinguishes these systems. Within the eye, wind speeds are very weak and a thermal inversion is often present at the top of the boundary layer, with warm, moist air below and hot, dry air above, with temperatures as high as 30°C at the 2-3 Km level and relative humidities well below 50%. The extraordinary heat and dryness of the air located inside the eye indicate that the air has subsided over a path several kilometers thick.

Figure 1.8 shows a simplified model representing a tropical cyclone structure. Air spirals into the storm in the boundary layer and rises in rain bands and in the ring of deep convection surrounding the eyewall, where rainfall rates range up to 50 mm h^{-1} (Wallace and Hobbs, 2006). The low-level radial inflow is strongest just outside the ring of clouds surrounding the eyewall and it drops to near zero at the eyewall itself, while the tangential component of the flow is strongest right at the eyewall. The outflow from the interior of the storm is strongest near the level of the cloud tops. Away from the eyewall the circulation at cloud-top level is mainly weakly anticyclonic and it is often axi-asymmetric. The winds in tropical cyclones are a superposition of the forward motion of the storm and the cyclonic circulation around it. Hence, wind speeds tend to be higher to the right (left) of cyclone tracks in the Northern (Southern) Hemisphere and low-level convergence

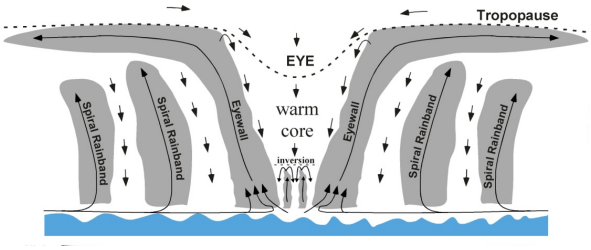

Figure 1.8: *Simplified tropical cyclone structure. (Yu, 2019)*

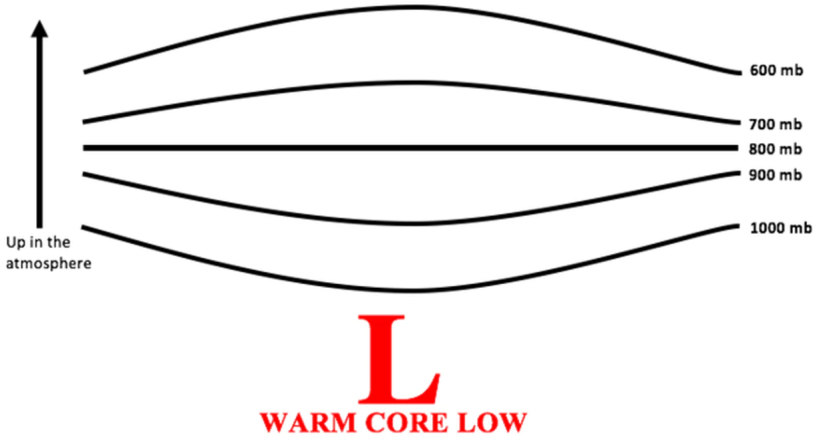

Figure 1.9: *Schematic representation of a warm core low cross section. (Reardon, 2016)*

and ascent tend to be enhanced in the right (left) forward quadrant. Beyond the ring of deep convection encircling the eyewall, much convection in tropical cyclones is concentrated in spiral rain bands that exhibit characteristics similar to those of squall line storms.

Basically all tropical cyclones form in certain regions of the outer tropics, where the following features are found: Coriolis force is small but appreciable; sea surface temperature is sufficiently high (SST $\geqslant 26.5°C$); vertical wind shear between upper and lower troposphere is weak enough to enable the vortex to develop.
The transformation of a non-rotating mesoscale convective system into a tropical cyclone requires time for the converging low-level inflow to concentrate the ambient vorticity. A deep atmospheric column within the system needs to be moistened, eliminating the mid-tropospheric minimum in equivalent potential temperature, thereby inhibiting the development of evaporatively cooled downdrafts.

As the core finally begins to warm in response to the heating and moistening of the inflow air by air-sea fluxes, pressure surfaces bulge upward in the upper troposphere, inducing an unbalanced outward pressure gradient force at that level. A schematic view of this typical tropical cyclones pressure setup can be seen in figure 1.9, in contrast to

the cold core low setup shown in figure 1.6. Thus, upper tropospheric divergence, in turn, induces outflow, which causes sea-level pressure to drop. The radial sea-level pressure gradient drives an inflow of boundary-layer air, which acquires rotation due to the action of the Coriolis force. The fluxes of latent and sensible heat from the underlying ocean surface increase in response to the increasing surface wind speed. Stronger fluxes lead to stronger heating within the storm, forcing stronger upper level divergence, and so on.

Tropical cyclones require several days in order to reach their peak intensity. They typically tend to track westward for a week or so, and then recurve poleward around the western boundary of the subtropical anticyclones. Typical rates of movement are on the order of 5-10 m s^{-1} (Wallace and Hobbs, 2006). As a storm drifts westward and poleward it may vary in intensity from one day to the next as it encounters different environmental conditions and undergoes changes in its own internal structure. Eventually, tropical cyclones either drift to higher latitudes where the sea surface temperatures are too cool to sustain them or they encounter land. Storms that make landfall are radically transformed within a matter of hours. In the absence of latent heat fluxes from the air-sea interface, the extreme low pressure within the eye cannot be sustained.

The greatest damage caused by tropical cyclones is concentrated along the coasts where the storm landfall occurs, often in combination with *storm surges* from the sea. Storm surges are the result of a sum of factors: a wind-driven onshore current, which, in combination with wind stress, pushes water against the shore and raises sea level to several meters; wind waves and swells that carry additional shoreward momentum; river runoff flowing into bays; a hydrostatic component, in which the depression of sea-level pressure is compensated by a rise in sea level (about 1 m sea-level rise per 100 hPa depression of sea-level pressure (Wallace and Hobbs, 2006)); astronomical tides, which may serve to exacerbate the severity of the storm surge, as we will see in the analysis of

the event that is subject of this work.

Chapter 2

Numerical weather prediction models

A model is a set of equations and other mathematical relationships that represent physical phenomena. A mathematical model is created with the purpose of providing predictions about the future state of a phenomenon or system. Generally, a model describes the probable evolution of a phenomenon or a system on the basis of initial data (*initial conditions*) provided by the user (*input*) by returning final data (*output*). The effectiveness of the model can then be measured by comparing the final data with the observed result of the evolution of the phenomenon or system.

In meteorology, numerical weather prediction models solve a set of equations, called *primitive equations*, based on current physical and chemical knowledge. Starting from the initial conditions, i.e. meteorological observations across the globe, one can therefore predict the future state of the atmosphere. The ever-increasing detail and length in time of these predictions are largely due to increasing computing power and improving numerical weather prediction models that run on them. In fact, the first numerical weather prediction (NWP) models used simplified versions of the complete equations of motion and were applied only to small geographical areas. If in 1949 a one-layer

model began to be used (Charney, 1950), the first six-vertical-layer primitive equation model became operational only in 1966 (Shuman and Hovermale, 1968) thanks to the improvement of the computers on which the models ran. In 1980 the first global models arrived (Sela, 1980), while in the 1990's the first mesoscale models were developed, with ever greater and long-term prediction resolutions, up to the present day.

Nowadays, NWP models can be divided into two categories: *General Circulation Models* (GCMs), which daily make predictions of the entire atmosphere over the globe, with a horizontal resolution of the order of tens of kilometers in medium time range (¡ three weeks); they supply their output data as initial and boundary conditions to the other category, the *Limited Area Models* (LAMs), which cover only a small geographical portion, with a higher horizontal resolution, which can reach hundreds of meters; using greater computing power, these models are only run on short-time ranges (usually no more than five days). They are used to provide a more accurate forecast, which also takes into account local factors influenced by orography, as well as to better simulate small-scale phenomena.

2.1 Primitive equations

The equations introduced into numerical weather prediction models, called primitive equations and solved to obtain the forecast of the atmosphere future state, are the following (from Holton (2004)):

$$\frac{D\boldsymbol{U}}{Dt} = -2\boldsymbol{\Omega} \times \boldsymbol{U} - \frac{1}{\rho}\nabla p + \boldsymbol{g} + \boldsymbol{F_r} \qquad \text{Momentum Equations} \tag{2.1a}$$

$$\frac{1}{\rho}\frac{D\rho}{Dt} + \boldsymbol{\nabla} \cdot \boldsymbol{U} = 0 \qquad \text{Continuity Equation} \tag{2.1b}$$

$$c_v\frac{DT}{Dt} + L\frac{Dq}{Dt} + p\frac{D\alpha}{Dt} = \dot{Q} \qquad \text{Energy Conservation Equation} \tag{2.1c}$$

$$\frac{Dq}{Dt} = \dot{P}_q \qquad \text{Humidity Conservation Equation} \tag{2.1d}$$

$$p\alpha = R_d T_v \qquad \text{State Equation} \tag{2.1e}$$

where $\boldsymbol{U}$ is the velocity vector, $\boldsymbol{\Omega}$ is the angular velocity of the Earth, ρ is the density, p the pressure of the environment, $\boldsymbol{g}$ is the gravity term, $\boldsymbol{F_r}$ are the frictional forces, c_v is the specific heat of dry air at constant volume, T is the ambient temperature, L is the latent heat, q is the water vapor mixing ratio, α is the specific volume, $\dot{Q}$ is the diabatic heating rate, $\dot{P}_q$ is the sum of all the source and sink rate terms of q in the atmospheric columns, R_d is the gas constant for dry air and T_v is the virtual temperature.

The scale analysis allows to apply some approximations: the hydrostatic approximation

$$\frac{\partial p}{\partial z} = -\rho g \tag{2.2}$$

usually used in GCMs and LAMs with grid spacing greater than 7-8 Km, and the geostrophic approximation

$$\boldsymbol{V_g} = \boldsymbol{k} \times \frac{1}{\rho f}\nabla p \tag{2.3}$$

where $\mathbf{V}_g$ is the geostrophic wind vector.

2.2 Parameterization

Model resolution refers to horizontal and vertical scales that can be resolved or reproduced by numerical models. Since the more this resolution increases, the more is the demand for computing power, at some point the number of computations that can be performed becomes limited even for the fastest computers. To carry the computations, the atmosphere is represented in a three-dimensional set of points, called a grid, which covers the region of interest. At each point the state of the atmosphere is represented. The smaller the distance between each point, the higher the resolution of the model. However, even for denser grids, there will always be structures that are small enough not to be captured by the model. These structures are for example sea breezes, thunderstorms and snow bands, but there are also even smaller structures that cannot be represented by a numerical model. However, solving these processes is of paramount importance for a correct weather forecast. In this context, parameterization, i.e. the procedure by which these processes difficult to be solved are represented, becomes of fundamental importance.

2.2.1 Radiation

Radiation is the propagation of energy through electromagnetic waves. Solar radiation is the fundamental energy source for the Earth and the atmosphere, the uneven distribution of which reaching the Earth leads to different heating and horizontal gradients that guide the atmospheric circulation. The radiation can be of shortwave or longwave type: the first comes directly from the Sun and can be absorbed by surfaces or by atmospheric gases, or scattered, while longwave radiation is the radiation emitted by the surfaces and the Earth's atmosphere. The emission spectrum is very broad, with the radiation being emitted at different wavelengths. The mathematical treatment of all these processes would be excessively heavy if it were to be carried out for each line of the radiation spectrum. Then it is divided into different frequency bands, where each of them has a

different ability to interact with particles and atmospheric gases.

2.2.2 Convection

Atmospheric moist convection results from the radiative cooling of the atmosphere, surface fluxes, forcing by large-scale motions, and buoyancy associated with water phase changes. It is a process that occurs at different spatial and temporal scales: shallow convective cells or individual deep convective cells are observable, ranging from a few kilometers to hundreds of kilometers in extension, of short duration (a few hours or even minutes) or longer (up to a few days). From this we understand the importance of convection in atmospheric processes and how challenging its representation in models is.

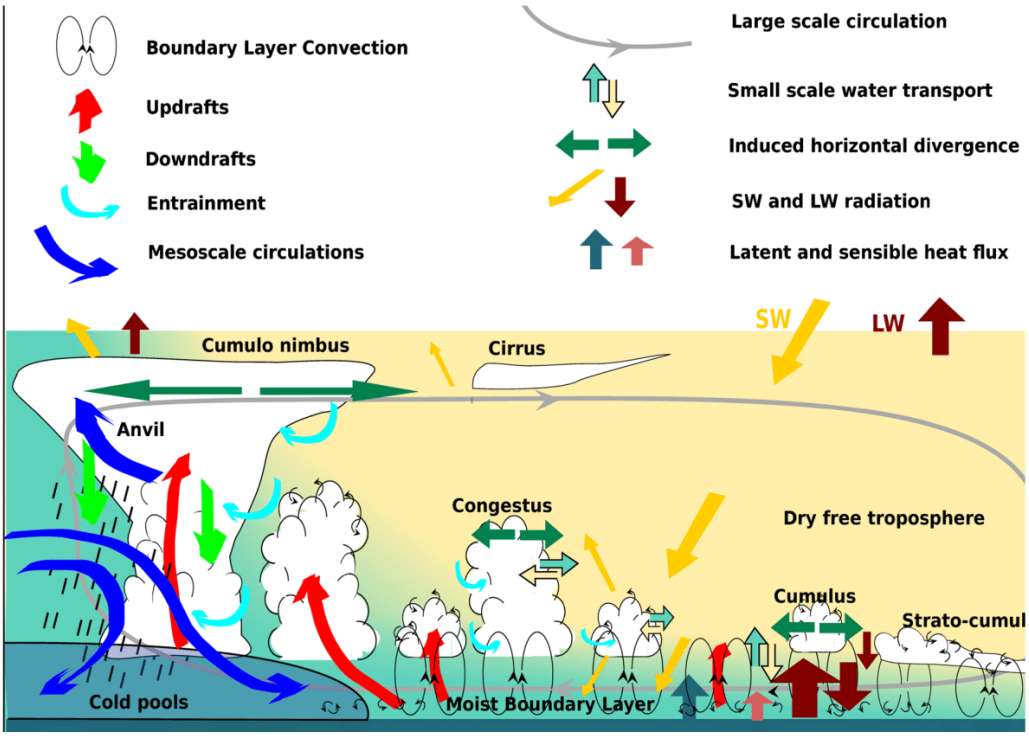

Figure 2.1: *Various aspects of atmospheric convection and its interaction with radiation, humidity, surface fluxes and large-scale circulation targeted by parameterization developments. - Source: (Rio et al., 2019)*

Most of the parameterizations currently in use are updated schemes built in the 1980's and 1990's. They are mainly based on the mass-flux approach, which aims to explicitly represent the underlying convective physical processes, breaking down the atmospheric column into different components (updrafts, downdrafts, subsiding environment). However, many difficulties remain, pushing the scientific community to find new solutions, such as the introduction of cloud-resolving models or large-eddy simulations in each atmospheric column, or machine learning methods. (Rio et al., 2019)

2.2.3 Clouds

Cloud parameterization must consider numerous processes, many of which are governed by stochastic equations, which take place at microscopic scales. In fact, a cloud is an aggregate of very small water droplets, ice crystals or a mixture of both. With the exception of some particular cases, clouds are confined to the troposphere and are mainly formed by vertical motions originating from air heating or by forced ascent on obstacles of different types, or by large-scale vertical motions. When a cloud is at temperatures below 0°C it mainly consists of supercooled water droplets down to about -10°C in case of stratiform clouds, down to about -25°C in case of convective clouds. Between one of the two threshold temperatures and the temperature of -38.5°C, both water droplets and ice crystals are found in the cloud. Below -38.5°C, clouds are mainly made up of ice crystals.

Cloud droplets can originate through heterogeneous nucleation processes, with the interaction between the droplets and aerosol particles - i.e. *Cloud Condensation Nuclei* (CCN) - in supersaturation conditions, or through a homogeneous nucleation process, that takes place at temperatures below -38.5°C and without the aid of aerosol particles. Subsequently, droplets can grow in many different ways and become drops, raindrops, graupels or hail, with processes still not very understood. From these processes derives the necessity and, in any case, the difficulty in the correct representation of cloud processes.

2.2.4 Turbulence

Turbulent phenomena are frequent in the *Planetary Boundary Layer* (PBL), where atmospheric motions are influenced by the presence and characteristics of the Earth's surface and the biosphere. Its height can vary from a few meters up to a few kilometers and is characterized by time scales of the order of one hour. Such turbulent motions are difficult to analyse mathematically, due to the stochastic nature of the mixing processes, and different parametrization schemes have been developed in recent years and implemented in numerical models.

2.2.5 Land-Surface models

Land Surface Models (LSMs) use quantitative methods to simulate the biogeochemical, hydrological and energy cycles that take place at the interface between the Earth's surface and the atmosphere. The surface sensible heat and surface latent heat fluxes, and the short-wave upward reflected and long-wave upward radiation emitted are simulated. These provide lower boundary conditions for vertical motions.

2.3 Numerical methods

A system of differential equations is referred to as an initial value problem when the solution depends not only on boundary conditions but also on the values of the unknown fields or their derivatives at some initial time. Weather forecasting is a primary example of a nonlinear initial value problem. Owing to its nonlinearity, the equations of motion are complicated to analyse. However, it is possible to use simpler linearized prototype equations which correspond to different numerical methods.

A method used in almost all NWP models is the *Finite Difference Methods* (FDMs). FDMs are discretization methods for solving differential equations by approximating them with difference equations, in which the derivatives are approximated up to the desired

order. In this way nonlinear equations can be converted into systems of linear equations, which can be solved with matrix algebra techniques. There are two methods for solving equations: *explicit methods*, which solve the equations in a forward way, knowing the current approximate value of the solution and moving it on in time and space; *implicit methods*, which find a solution by solving the equation involving both the current and future state of the system. The implicit methods are stable, but more complicated to handle because they solve the equations in all grid point directions at the same time and this becomes excessively expensive in terms of computing power. They also cannot be used in the presence of nonlinear terms. Semi-implicit schemes in which the linear terms are treated implicitly and the nonlinear terms explicitly have become popular in modern forecasting models.

An alternative approach is represented by the *spectral method*, in which the spatial variations of the dependent variables are represented in terms of finite series of orthogonal functions, called *basis functions*. For the spherical earth the appropriate basis functions are the spherical harmonics. Spectral methods are more accurate than low-resolution FDMs, such as in global circulation models. However, they have quite a few problems when there are many components of spherical harmonics, due to the nonlinear nature of the advection terms.

Currently, NWP models are based on the approximate primitive equations observed previously. However, the vertical coordinate, generally considered terrain-following, is defined for example as:

$$\sigma = \frac{p}{p_s} \tag{2.4}$$

where p is the pressure and p_s is the pressure at the surface, with $\sigma = 1$ on the ground and 0 on the top. In this way the primitive equations are solved in a particular type of grid on which the variables are not all predicted on the grid points but rather are placed in different points (e.g. scalar variables at the center of the control volumes and velocity

or momentum variables at the cell faces). Such a grid is called "staggered". A vertical staggered grid has narrower levels near the ground and more distant near the top of the model, due to the higher resolution required in the lower atmosphere.

Chapter 3

Analysis tools

In this chapter, the tools used in the analysis will be presented and described.

3.1 WRF-ARW model

The Weather Research and Forecasting (WRF) Model is a mesoscale numerical weather prediction system designed for both atmospheric research and operational forecasting applications. It consists of two dynamical cores, a data assimilation system, and a software architecture that supports parallel computing and system extensibility. The model serves a wide range of meteorological applications at different spatial scales, from tens of meters to thousands of kilometers. WRF was developed in the late 1990's from the joint effort between the National Center for Atmospheric Research (NCAR), the National Oceanic and Atmospheric Administration (represented by the National Centers for Environmental Prediction (NCEP) and the Earth System Research Laboratory), the U.S. Air Force, the Naval Research Laboratory, the University of Oklahoma, and the Federal Aviation Administration (FAA) (Skamarock et al., 2019).

The WRF model can produce simulations based on actual atmospheric conditions (i.e. from observations and analyses) or idealized conditions. The two dynamical cores that

constitute the model are the Advanced Research WRF (ARW) and the Nonhydrostatic Mesoscale WRF Model (NMM): the first is used for atmospheric research and the simulation of real or idealized cases, while the second for operational forecasting. WRF solves the governing Euler equations of motion in non-hydrostatic way (a hydrostatic option is however usable) with terrain-following vertical hybrid coordinates based on a normalized atmospheric pressure. The Arakawa C-grid staggers the horizontal grid points, so that temperature and horizontal wind fields are horizontally shifted; the vertical component of velocity is also staggered vertically with respect to the other fields. Time integration is done using second and third order Runge-Kutta schemes, while spatial discretization is performed with second and sixth order advection schemes.

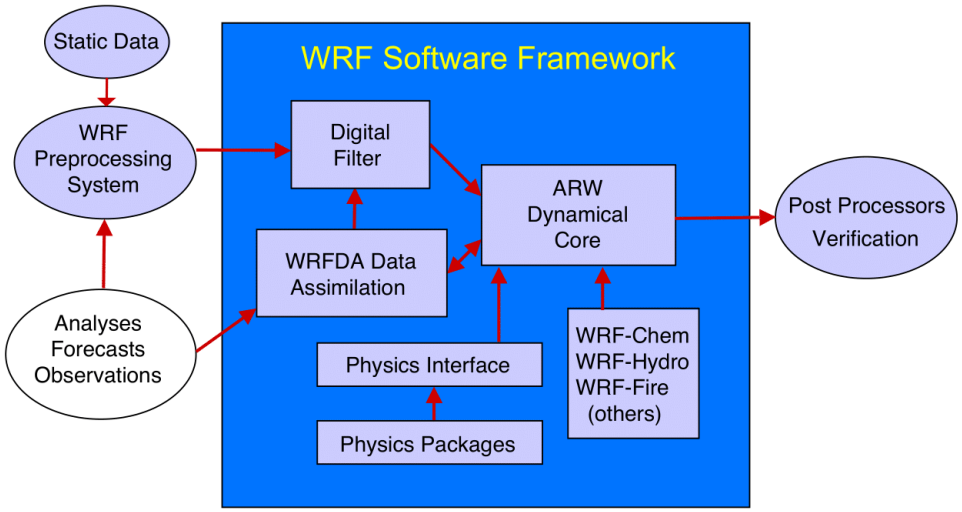

Figure 3.1: *Advanced Research WRF system components - Source: (Skamarock et al., 2019)*

For what concerns the simulation of real cases, the WRF model simulation consists of two steps: the WRF Pre-processing System (WPS), which creates the grid and defines the initial and lower boundary conditions, and the ARW model, in which the model solves the atmospheric equations.

The WPS is composed of three programs: *geogrid.exe*, which produces the domain and configures the geographic data (topography and map projection); *ungrib.exe*, which

extracts the data useful for initialization from the fields produced by the global models (ECMWF or GFS, among the best known) in GRIB format (General Regularly-distributed Information in Binary form); *metgrid.exe*, which horizontally interpolates the meteorological fields, using the previously processed data. WPS settings can be changed in the *namelist.wps* file, where one can also create multiple nested domains with fine-resolution grid inside the main parent domain. Nested domains can communicate in two different ways: one-way nesting, when information flows only from the parent domain to the smaller nested domain, and two-way nesting, when the parent domain and the nested have mutual feedback during simulation, with information that passes from the outermost domain to the innermost one and vice versa.

In the second step, the *real.exe* and *wrf.exe* programs are run, created after the initial configuration of the model. Their output will depend on the settings previously chosen in the namelist.input file, where various parameters can be changed, e.g. starting and ending run time, domain parameters, type of physics and microphysics and more. Once the two files have been executed, the output files are generated, which are then processed with graphics tools useful in viewing the data obtained.

3.2 GFS model

The input data used as initial and boundary conditions are provided by the Global Forecast System (GFS) model, a global numerical weather prediction system containing also variational analysis run by the U.S. National Weather Service (NWS). The GFS model runs four times a day, and produces forecasts for up to 16 days in advance. The forecast component uses the Finite Volume Cubed Sphere (FV3) dynamical core with a resolution of 13 Km. In the vertical, the model is divided into 127 vertical levels. It produces forecast output every hour for the first 120 hours, then every 3 hours for days 5-16 (EMC-NCEP-NOAA, 2021). GFS model data were downloaded from the NCEP

Products Inventory (NCEP-NOAA, 2021b).

3.3 ERA5 reanalysis

The reanalysis data, here used first to observe the geopotential height fields at 500 hPa and mean sea level pressure, then to make a comparison with the WRF model simulations, come from the European Center for Medium-Range Weather Forecasts (ECMWF) Reanalysis 5th Generation (ERA5) model. The data coverage of ERA5, combined with the observed data, is global; the atmosphere is divided with a 30 Km spacing horizontal grid and into 137 hybrid sigma/pressure vertical levels from the surface up to a height of 80 Km. The released ERA5 data are available from 1979 up to 3 months from real time with assured quality, and up to 5 days from real time with non-validated quality. The datasets were produced on behalf of Copernicus Climate Change Service (C3S) and were downloaded from the Climate Data Store (CDS) (NCEP-NOAA, 2021a).

3.4 CPSM and ISPRA stations network

The observed data analysed in chapter 4 were acquired by the integrated weather-tidal networks of the *Centro Previsioni e Segnalazioni Maree del Comune di Venezia* (CPSM) of the Municipality of Venice, and of the *Istituto Superiore per la Ricerca e la Protezione Ambientale (ISPRA)*. The real-time data and the historical series of all 42 stations in the Venice lagoon are published online (www.venezia.isprambiente.it, www.comune.venezia.it/maree).

The CPSM stations measure the tide levels by means of floating hydrometers, collecting and transmitting the data to the central office via a control unit equipped with a data logger.

Figure 3.2: *CPSM and ISPRA integrated tidal network stations; on the right, an enlargement of the Venice stations. - Source: (CPSM et al., 2020)*

Some of these stations also record weather data, being equipped with a digital barometer, shielded thermo-hygrometer, solar radiation sensor, three-cup anemometer and wind vane, and rain gauge. The ISPRA stations also collect tide level data and some of them also weather data, which are in turn transmitted to the central offices. The data is then available online at five-minute intervals. Tide levels data are then assimilated by the wave models to improve the forecast of high tides in the Venice Lagoon (CPSM et al., 2020).

It must be specified that near Punta della Salute in Venice there are two tidal stations, one on the Giudecca Canal and one on the Grand Canal, both with the wording *Punta della Salute*. In this work, only the data of the Giudecca Canal station are considered.

In addition, the two meteorological and tidal stations "Piattaforma CNR" and "Meda Abate", located in the open sea at 16 and 40 km respectively from the Venetian coast, are hosted on sites of the CNR-ISMAR of Venice.

3.5 NCL

The graphical visualization of the simulation results (post-processing) is achieved in large part by the NCAR Command Language (NCL), a product of the Computational & Information Systems Laboratory at the National Center for Atmospheric Research (NCAR).

NCL is a free interpreted language designed specifically for scientific data processing and visualization. It can read and write many file formats, including NetCDF, HDF, binary and ASCII data, and also can read formats such as GRIB1, GRIB2, shapefiles and other file types (UCAR/NCAR/CISL/VETS, 2016). It features a modern programming language, which includes types, variables, operators, expressions, conditional statements, loops, and functions and procedures (over 600).

NCL runs on UNIX-based operating systems. In the present study version 6.6.2 was used, installed and executed via shell on the Beowulf cluster of ISAC-CNR, Lecce (CNR-ISAC, 2019) to visualize the NetCDF output files from the WRF-ARW model.

3.6 MATLAB

The elaborations of the observed data and the associated charts were carried out with MATLAB, abbreviation of "MATrix LABoratory". It is a proprietary multi-paradigm programming language and numeric computing environment developed by MathWorks. It allows the manipulation of matrices and vectors, and the implementation of algorithms. Furthermore, MATLAB has built-in graphics features to allow the visualization of numerical results in two and/or three-dimensional plots.

3.7 Satellite images

The satellite images shown in chapter 4 are obtained by the Spinning Enhanced Visible and InfraRed Imager (SEVIRI) radiometer, on board the Meteosat Second Generation (MSG) and managed by the European Organization for the Exploitation of Meteorological Satellites (EUMETSAT). SEVIRI acquires atmospheric data in twelve spectral channels. They consist of eight channels in the thermal infrared (IR), one channel in the Near-IR (NIR), two in the Visible and one high-resolution in the Visible (HRV) (Aminou, 2002). Using channels that absorb ozone, water vapor and carbon dioxide, the characteristics of atmospheric air masses can be analysed and a three-dimensional view of the atmosphere can be reconstructed.

3.8 Google Earth

Google Earth is the most popular virtual globe software. It uses satellite images obtained from terrestrial remote sensing, aerial photographs and typographic data, stored in a Geographic Information System (GIS) platform. It is an open source software distributed by the Google LLC company.

In addition to displaying information, the software allows the individual user to enter additional information. Keyhole Markup Language (KML) is used to manage geospatial data in three dimensions.

In the chapter 4 Google Earth is used to indicate the position on the maps of the weather and tidal stations used in the work. In the chapter 5 it was used to create the *kmz* (Keyhole Markup language Zipped) file, in order to create the shapefile used for the analysis.

Chapter 4

Case study: observed data and analysis

On November 12, 2019 an exceptional high tide hit the city of Venice (Italy) and its entire lagoon, causing major damages to the buildings and to the historical artworks of the city. The highest sea level value in the city was 189 cm, reached at the tidal station of Punta della Salute (Canale della Giudecca side). This is the second highest value ever recorded since 1872, the year in which data began to be collected, just 5 cm below the absolute record of 194 cm, reached on November 4, 1966. (CPSM et al., 2020)

This chapter explores the reasons that caused the record tide, showing both meteorological and astronomical contributions, and then analyses the data observed by the weather-tidal stations, including the time series of the main meteorological quantities.

4.1 Meteorological analysis

In the days just before the event, the Mediterranean basin was affected by a number of lows, within a wide upper-level trough extending from the North Atlantic area up to North Africa coastlines. Figure 4.1 shows the maps of the mean sea level pressure

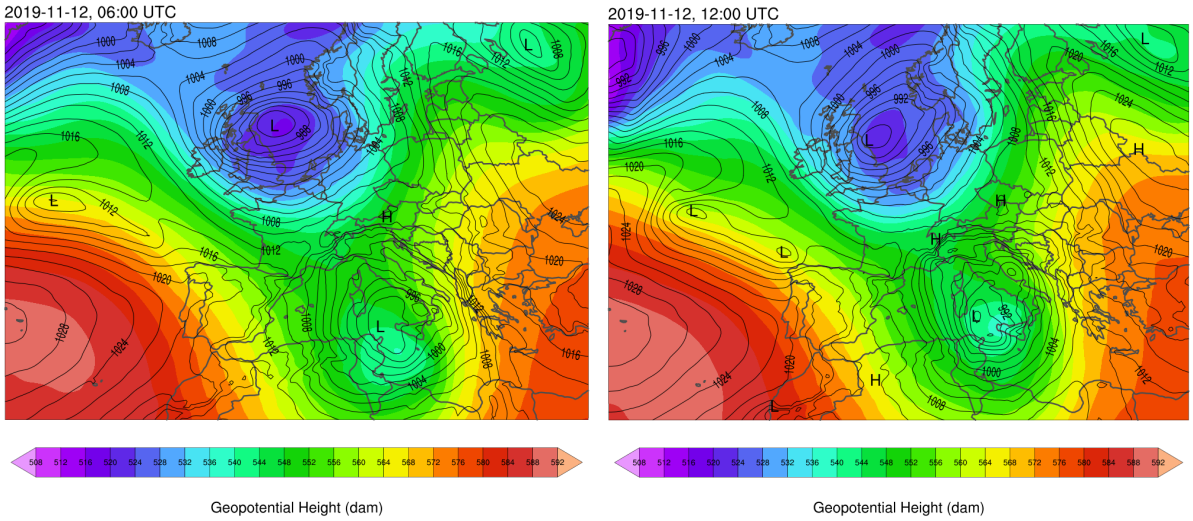

(a) (b)

Figure 4.1: *ERA5 Reanalysis - Mean sea level pressure field (black lines) and 500 hPa geopotential height (colours) at* a) *06:00 UTC and* b) *12:00 UTC of November 12, 2019.*

and geopotential height fields relative to the day of the event, respectively at 06:00 UTC (figure 4.1(a)) and at 12:00 UTC (figure 4.1(b)). They were derived from the ERA5 reanalysis data (Hersbach et al., 2018). Two prevailing systems can be noted: the Azores anticyclone to the west, in the Atlantic, and a cyclonic vortex positioned in the North Sea, between the British islands and Scandinavia. A corridor of low pressures at sea level is visible at the interface between the two weather systems: finding conditions of marked baroclinicity, these disturbances evolve into more structured low pressures and, transported by the jet stream towards southern Europe, are the reason for humid and perturbed flows on the central part of the Mediterranean basin. A cyclonic circulation is indeed present on the Mediterranean.

In this configuration, a secondary minimum arises from the cyclonic circulation over Sicily. It can already be seen from figure 4.1(b), positioned on the middle Adriatic off the coast of Abruzzo.

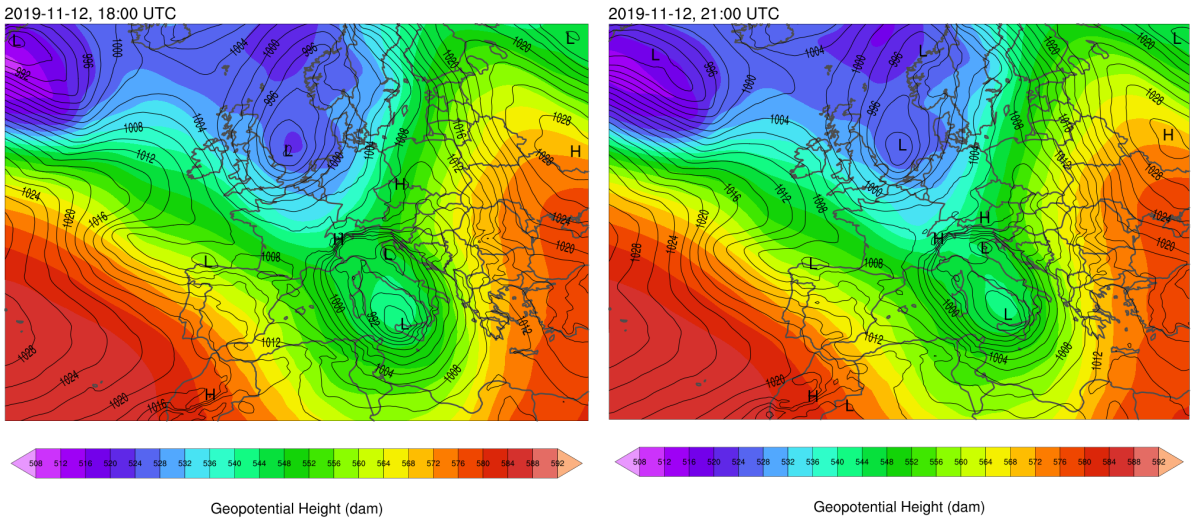

(a) *12/11/2019 - 18:00 UTC.* (b) *12/11/2019 - 21:00 UTC.*

Figure 4.2: *ERA5 Reanalysis - Mean sea level pressure field (black lines) and 500 hPa geopotential height (colours) at* a) *18:00 UTC and* b) *21:00 UTC of November 12, 2019.*

Six hours later (figure 4.2(a)) we observe the northwestward movement of the minimum towards the Venetian lagoon and the *landfall*, which from the reanalysis takes place at around 21:00 UTC (figure 4.2(b)). It is a rather spatially confined structure with very fast dynamics: at 00:00 UTC of November 13 (figure 4.3) only a few traces of the cyclone (a weak trough) remain on the mainland.

The presence of another anticyclonic pattern on the Eastern Europe, in addition to the one in the Atlantic, causes the persistence of the low on Southern Europe.

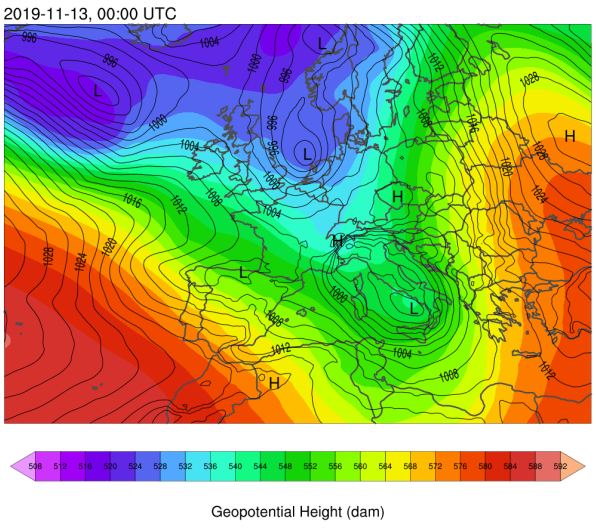

Figure 4.3: *ERA5 Reanalysis - Mean sea level pressure field (black lines) and 500 hPa geopotential height (colors). 13/11/2019 - 00:00 UTC.*

Consequently, the Sirocco winds on the Adriatic, activated by the Tyrrhenian low pressure, are intense, persistent and further amplified by the channeling effect between the mountain ranges of the Apennines to the west and the Dinaric Alps to the east (Cavaleri et al., 2020). The Bora wind that instead bursts from the North-East involves the northern area of the Adriatic Sea, carrying cooler and drier air.

Figure 4.4 shows the 10 m wind field predicted by the MOLOCH model (source: https://www.isac.cnr.it/dinamica/projects/forecasts/index.html) in the simulation initialised at 00:00 UTC of November 12, 2019 with GFS analysis/forecasts. The strong winds blowing around the Tyrrhenian minimum, positioned between Sardinia and Sicily, and the two wind patterns in the Adriatic described above are clearly visible in figure 4.4(a) at 12:00 UTC.

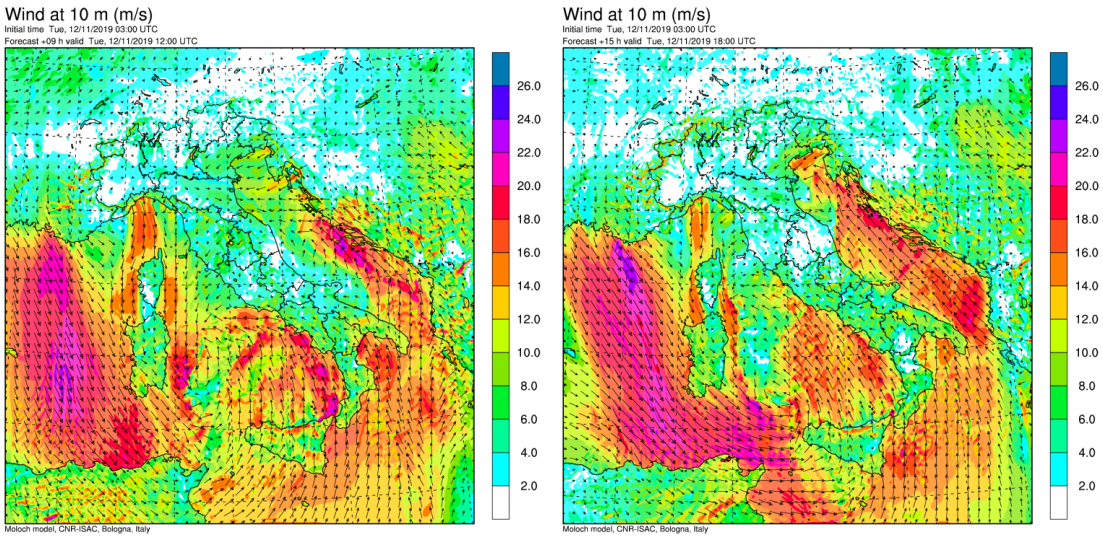

(a) *Valid for 12/11/2019 - 12:00 UTC.* (b) *Valid for 12/11/2019 - 18:00 UTC.*

Figure 4.4: *MOLOCH model forecast - Wind at 10 m (m/s). Initialization 12/11/2019 - 03:00 UTC.*

While the situation does not evolve much in the Tyrrhenian Sea, in contrast in the Adriatic it evolves fast. The deepening of a pressure minimum in the Adriatic Sea

determines the intensification of the winds around it, as it can be seen in the forecast for 18:00 UTC (figure 4.4(b)). The convergence between the strong Sirocco and Bora winds are evidence of a cyclonic circulation, confined in a limited area.

For this reason it is not easy to identify the cyclone from satellite images. The images of the SEVIRI radiometer (Spinning Enhanced Visible and Infrared Imager) onboard the Meteosat Second Generation (Schmid, 2000) were extracted; in this case those of channel 9 detect the infrared radiation emitted at a wavelength of 10.8 μm (appropriate since the event occurred exclusively at night). In addition to the small size of the cyclonic structure, also the presence of high clouds in the area, make its observation from satellite very complicated to interpret. However, the structure is visible in a single shot at 20:00 UTC as shown in figure 4.5.

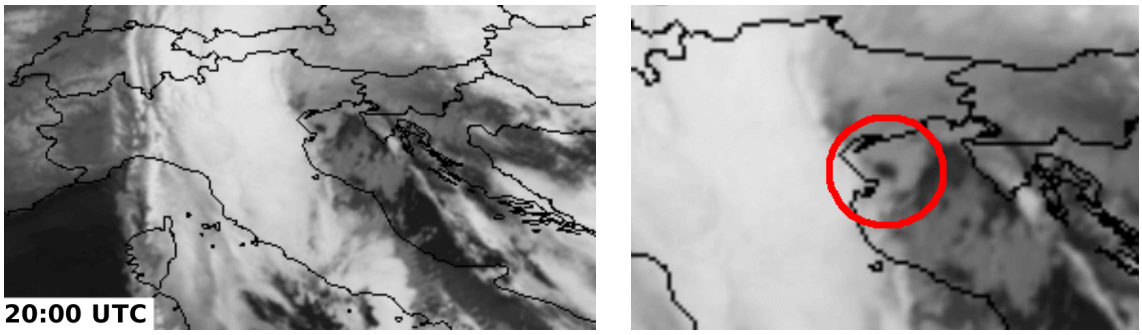

(a) (b)

Figure 4.5: *SEVIRI Channel 9 - Infrared emitted radiation at 10.8 μm at 20:00 UTC of November 12, 2019* - a) *The small cyclonic structure appears after the passage of high clouds north to the Po delta;* b) *the red circle highlights the eye of the storm. (Source: EUMETSAT, 2021)*

Darker colors indicate higher brightness temperatures, lighter colors mean lower brightness temperatures (higher clouds). From the first image (figure 4.5(a)) it is possible to observe the passage of high clouds associated with the main depression system located in the Tyrrhenian Sea. However, at this time it is also possible to observe the small

secondary cyclonic structure in the sea north of the Po delta, whose eye is visible and highlighted in figure 4.5(b). It is surrounded by low clouds and there seems to be no trace of deep convection near it.

A cyclonic system so small but at the same time so intense, as we will see later, has triggered a series of forcing that have contributed to the rise of the sea level in the Venice lagoon, as we will see in the next paragraph.

4.2 The high tide: storm surge and astronomical tide

The event of November 12, 2019 will be remembered for the exceptional tide that hit the Venice lagoon and for the record sea level values reached that evening. The main cause is a meteorological factor, i.e. the *storm surge*, the phenomenon of sea level rise in coastal areas due to the passage of a cyclone. There are five processes that contribute most to the storm surge: the atmospheric pressure effect, the direct wind effect, the effect of waves, the effect of the earth's rotation, the effect of rainfall. The first is the so-called *inverse barometric effect*, the rise in sea level in the areas affected by a drop in atmospheric pressure and the descent instead in the areas affected by an increase in atmospheric pressure. In general, it is difficult to separate this effect from the second on the list, that of *direct wind*, which is also related to pressure. The approach of a cyclone to coastal areas determines an increase in wind: in case the latter blows towards the coast, tends to push and accumulate sea water, thus causing an increase in its level. As the wind increases, so do the *waves*, which are responsible for a significant transport of water, especially near the coast. The *Earth's rotation* contributes to the storm surge as it accelerates the sea current to the right in the Northern Hemisphere. Hence, if there is a coastline on the right of the cyclone, then the sea level will rise. The effect of *rainfall* is the last in the list: it is an effect that mainly affects the areas of river mouths, especially

estuarine mouths (Harris, 1963). This is therefore not the case in Venice, a city that stands on a lagoon that covers an area of about 550 Km^2. The lagoon is characterized by a complex system of islands, salt flats and canals, as a result of both natural and anthropogenic processes. Astronomical tides and winds (Sirocco from the southeast and Bora from the northeast) are the main factors responsible for the circulation of water within this system (Rizzetto and Tosi, 2012). In our case study, a blocked meteorological situation favoured the persistence of the Sirocco winds, causing the average sea level to rise (CPSM et al., 2020). On November 12, the pre-conditions were already favorable to the flooding of the Venetian lagoon. In fact, the combination of meteorological and astronomical contributions caused a sharp rise in sea level. Observing the sea level heights

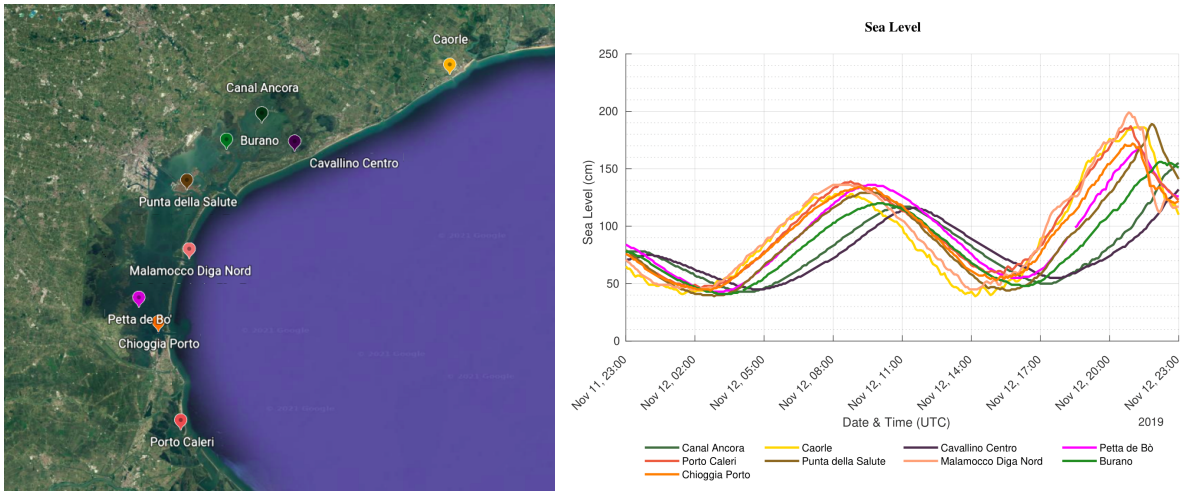

(a) (b)

Figure 4.6: *(a) Tidal stations selected from CPSM and ISPRA network and (b) relative sea level data for November 12, 2019. Each station has a different color associated with it.*

in figure 4.6(b), obtained from data recorded by the tidal stations selected by the CPSM and ISPRA network, whose geographical positions are shown in figure 4.6(a), two peaks in the sea level can be seen on the day of the event. They correspond to the semidiurnal cycle of the astronomical tide. The time shift with which the morning tide spreads inside

the lagoon can be noted, with the stations located further north reaching their peak a few hours later than the southernmost stations, with lower values than in the latter. The temporal delay is certainly due to the different propagation of the tide in the lagoon, while the lower peaks of the northern stations are attributable both to the friction of the shallow waters (Ferla et al., 2007) and to the Bora wind which hinders the flow of the high tide to the North. In the second high tide that occurs in the evening hours, much higher levels are reached than in the morning, with very high peaks (i.e. Malamocco Diga Nord 199 cm; Punta della Salute, located in the center of Venice, 189 cm). Again, there is a temporal delay between the southern, central and northern stations, but there is also the steep drop in the level of the southern stations, and the slower but constant rise in the northern stations. This can be attributed to the change in wind direction accompanied by strong southwesterly gusts that push the sea water northeastward.

As mentioned before, the high tide event was exceptional mainly thanks to the overlapping of the meteorological and astronomical contributions. Figure 4.7 shows the sea level data recorded by the Punta della Salute station, in the center of Venice (black line), the contribution of the astronomical tide (dashed blue line) and the difference between these two contributions, the residual value (red line), which corresponds to the purely meteorological contribution. The so-called "good luck in bad", which avoided a disastrous tide to the city of Venice on other occasions, for example in the historic high tide of November 4,

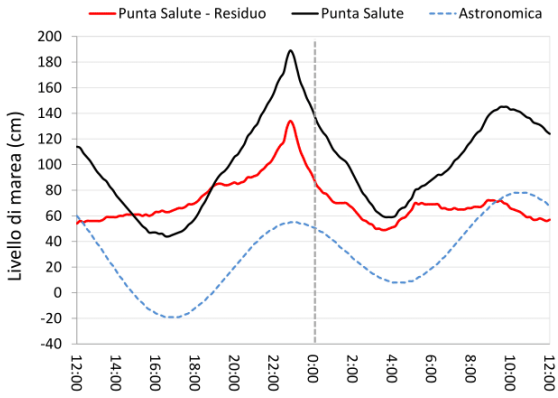

Figure 4.7: *Sea level recorded at Venice - Punta della Salute tide gauge (black line), astronomical tide (blue dashed line) and residual value (red line) between 12:00 (UTC+1) of November 12th and 12:00 (UTC+1) of November 13, 2019. Source: (CPSM et al., 2020)*

1966 (194 cm, absolute record for the city of Venice) or in the violent *Vaia storm* of October 29, 2018 (156 cm), did not occur this time and determined the occurrence of an exceptional tide in a wind setup generally unfavourable to exceptional tides, i.e. without strong and long lasting Sirocco winds which are usually responsible for high tides in the city of Venice. The wind setup and the other meteorological variables observed by the CPSM and ISPRA weather station network are discussed in the next section.

4.3 Observed weather data analysis

To understand the causes that led to the occurrence of a high tide event of such a magnitude, it is necessary to analyse the meteorological data observed by weather stations on that day. As already said, the event was exceptional from a tidal point of view, but also from a meteorological point of view, due to the rarity of the phenomenon that affected the entire Venice lagoon. Before going into the data analysis, we focus on the weather stations that have been selected and that are part of the CPSM and ISPRA station network (Figure 4.8). In addition to the stations in and around Venice and the other lagoon stations, the presence of weather stations in the open sea (*Piattaforma CNR* and *Meda Abate*) as well as those farther away from the lagoon (*Padova Meteo* and *Foce Po*) is essential to better understand the characteristics of the cyclone of November 12 and to understand as precisely as possible its path. Especially the *Foce Po*, *Meda Abate* and *Piattaforma CNR* stations are very useful because they give an idea of the cyclone features before it reaches the Venice lagoon, since it has risen along the Adriatic with a roughly Southeast-Northwest motion. Unfortunately the *Meda Abate* station that day transmitted its data intermittently, so intervals without data are present in the graphs. *Padova Meteo*, despite being located farther west, was also inserted to trace the path of the cyclone in the final phase following the transit in the lagoon. Figure 4.8(b) shows the detail of the Venice weather stations, which in figure 4.8(a) look superimposed due to

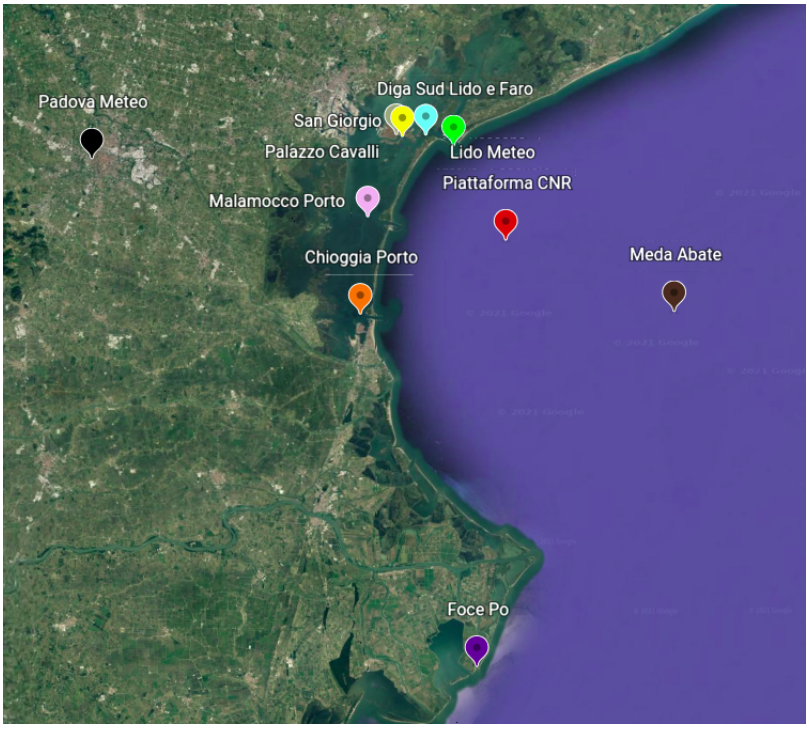

(a)

(b)

Figure 4.8: *Weather stations selected from CPSM and ISPRA network* - a) *Spatial distribution of weather stations in the lagoon;* b) *Zoom on the center of Venice to better visualize the city stations - Each station has a different color associated with it.*

their proximity to each other. All the stations located in the city (or at least very close to the city) were selected for the variety of information that their data provide despite the proximity among them. *Palazzo Cavalli* is right in the headquarters of the *Centro Previsioni e Segnalazioni Maree* (CPSM) of the Municipality of Venice, located on the Grand Canal.

Another urban station is *San Giorgio*, which resides on the island of San Giorgio Maggiore, located in front of Piazza San Marco. The other two weather stations in the figure, i.e. *Lido Meteo* and *Diga Sud Lido e Faro*, despite being in the immediate vicinity of the historic center of Venice, are not really urban stations. However, their position is strategic for the purposes of the analysis due to their proximity to the open sea.

4.3.1 Sea level pressure

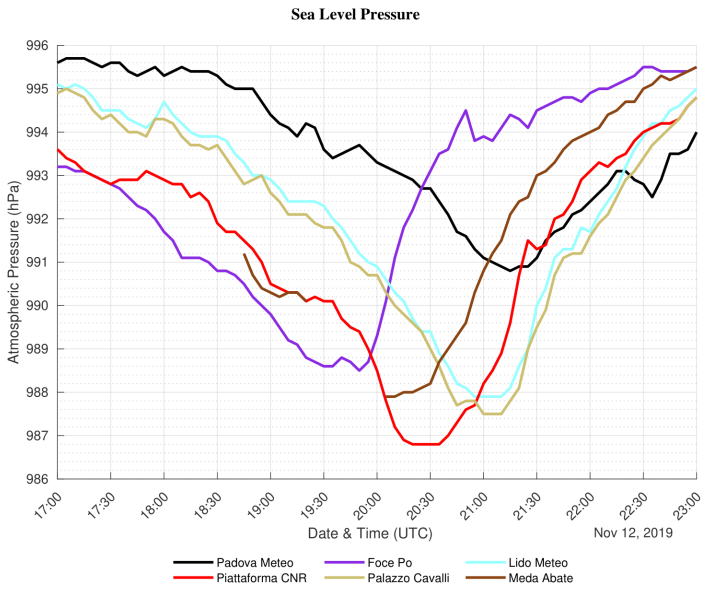

Figure 4.9: *Sea level pressure recorded by weather stations during the cyclone passage.*

First, the sea level pressure recorded by the stations with a barometer is analysed. Figure 4.9 shows the trend in the six hours that include the cyclone transit in the lagoon. From the minimum value reached by each detection point, one can guess the path taken by the cyclone. The first station to reach its minimum value is Foce Po, the southernmost station of all, between 19:30 and 20:00 UTC, given the Southeast-Northwest movement of the cyclone.

The second station to reach its minimum value is Meda Abate, around or shortly after 20:00 UTC, while the pressure drop continues in the other stations, with the exception of Foce Po, where a strong increase is observed. Around 20:30 UTC the Piattaforma CNR station records a pressure value of 986.8 hPa, the absolute minimum among all the stations. Subsequently, the cyclonic structure approaches the lagoon, as the lowest values in Palazzo Cavalli and Lido Meteo are recorded simultaneously around 21:00 UTC, but with a value of about 1 hPa higher than in the Piattaforma CNR station. In Padova Meteo a minimum slightly below 991 hPa is recorded at around 21:15 UTC.

4.3.2 Temperature and humidity

Figure 4.10 plots the air temperature (T), dew point temperature (Td) and relative humidity (RH) values. In order to better understand the timing of the cyclone transit in the weather station area, sea level pressure values are reported in the lower panel. The weather stations examined are: Piattaforma CNR, San Giorgio and Palazzo Cavalli, the only ones for which temperature and humidity data are available. Among these three, only the Piattaforma CNR and Palazzo Cavalli stations also record the pressure data. However, given the proximity between the stations of Palazzo Cavalli and San Giorgio (see

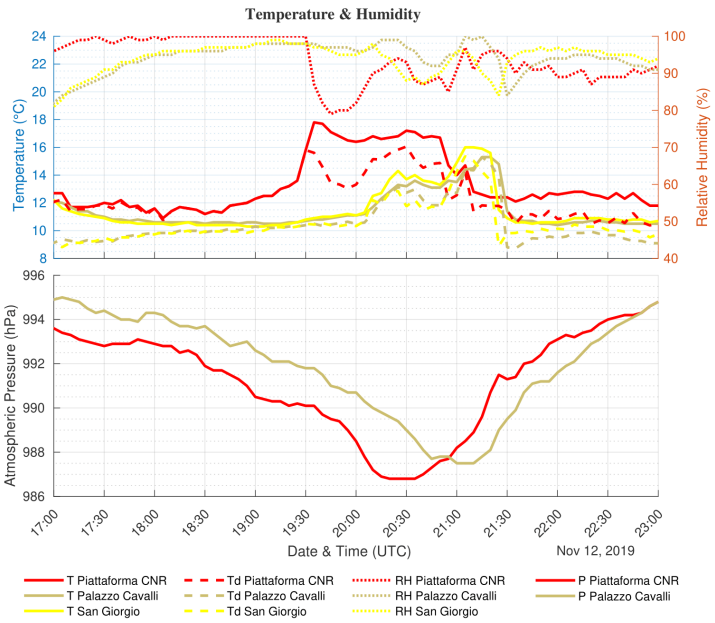

Figure 4.10: *Air temperature (T, solid line), dew point temperature (Td, wide dashed line) and relative humidity (RH, narrow dashed line). Sea level pressure trend is in the graph below.*

figure 4.8(b)), it is reasonable that the sea level pressure data in Palazzo Cavalli can be applied to the San Giorgio weather station. What can be observed in figure 4.10 is the trend of the variables between 17:00 and 23:00 UTC on November 12. In the hours preceding the arrival of the cyclonic structure, the stations record temperature values between 10 and 12°C, with high relative humidity values. The humidity especially in the Piattaforma CNR station is near saturation, conditions certainly amplified by the position of the station (open sea). The situation changes quickly after 19:30 UTC, about an hour before the minimum pressure value is recorded: the air temperature rises quickly until it reaches almost 18°C, an increase of about 6°C in about an hour. Together with the increase of air temperature, the dew point temperature also increases and reaches almost 16°C, reflecting a change in the air mass. Half an hour later there is a drop of about 1.5°C in air temperature and more than 2°C in dew point temperature. Subsequently, the air temperature settles around 17°C, while the dew point temperature slightly increases again, settling, with various fluctuations, around 15°C. This happens until around 21:00 UTC, when the atmospheric pressure starts to increase and temperature and humidity return to values similar to those recorded before 19:30 UTC. The same dynamics occur in Venice, shifted by about 30 minutes with respect to the Piattaforma CNR. In both the stations of Palazzo Cavalli and San Giorgio the only difference with respect to the trend in the open sea is that the temperature increase occurs in two phases (for a total of about 5°C compared to the previous values, almost comparable to the increase at Piattaforma CNR). Around 21:30 UTC when atmospheric pressure starts to increase, temperature and humidity values return to the initial values. The passage of a rather compact structure seems to occur, given the strongly local features that the variations in temperature and humidity apparently assume. The change of air mass seems to take place only during the passage of the cyclone, with characteristics very different characteristics from the pre-existing air mass (warmer and humid air).

4.3.3 Wind

Wind played a fundamental role in the evolution of this event, since from its variations in intensity and direction valuable information is obtained on the movement and characteristics of the cyclone. Furthermore, the areas affected by the high tide changed according to its direction and intensity. So hereafter we analyse in detail the data recorded by the weather stations located in and around the lagoon.

In figure 4.11 it is possible to observe the trend of speed (top) and direction (bottom) of the wind from 11:00 UTC to 23:00 UTC on November 12. First of all, observing the period prior to the approach of the cyclone (up to about 18:30 UTC) we can see a rather uniform wind direction for all the stations from the North-Northeast. The speeds, net of turbulent fluctuations, are on average sustained, especially in the open sea (Piattaforma CNR) or in the most exposed coastal areas (Chioggia Porto), with winds on average between 10 and 15 m/s. Winds around 10 m/s are recorded in the Venice area (San Giorgio and Diga Sud Lido e Faro), around 7 m/s at Foce Po while winds of less than 5 m/s are reported by Padova Meteo. The situation changes starting from 18:30 UTC, when data from the Meda Abate station become available. Dealing exclusively with the wind direction, Meda Abate is the first station to indicate a rotation, in this case to the East-Southeast direction, while the other two stations of Foce Po and Padova Meteo undergo a rotation in the other direction, the first recording a wind increasingly westerly, the second mostly northwesterly. The intensities increase slightly in this time period, with speeds greater than 20 m/s recorded by the Chioggia Porto and Meda Abate stations.

From 20:00 UTC the sudden change of direction of the Chioggia Porto station is certainly noticeable, passing from a north direction to an east-northeast direction, in the meantime recording a rapid drop in wind speed, down to a value of less than 2 m/s! Around 21:00 UTC there are the greatest differences between the different anemometers: while the weather stations near Venice and Malamocco Porto, Piattaforma CNR and Meda Abate record south-southeasterlies, the southernmost Chioggia Porto and Foce Po

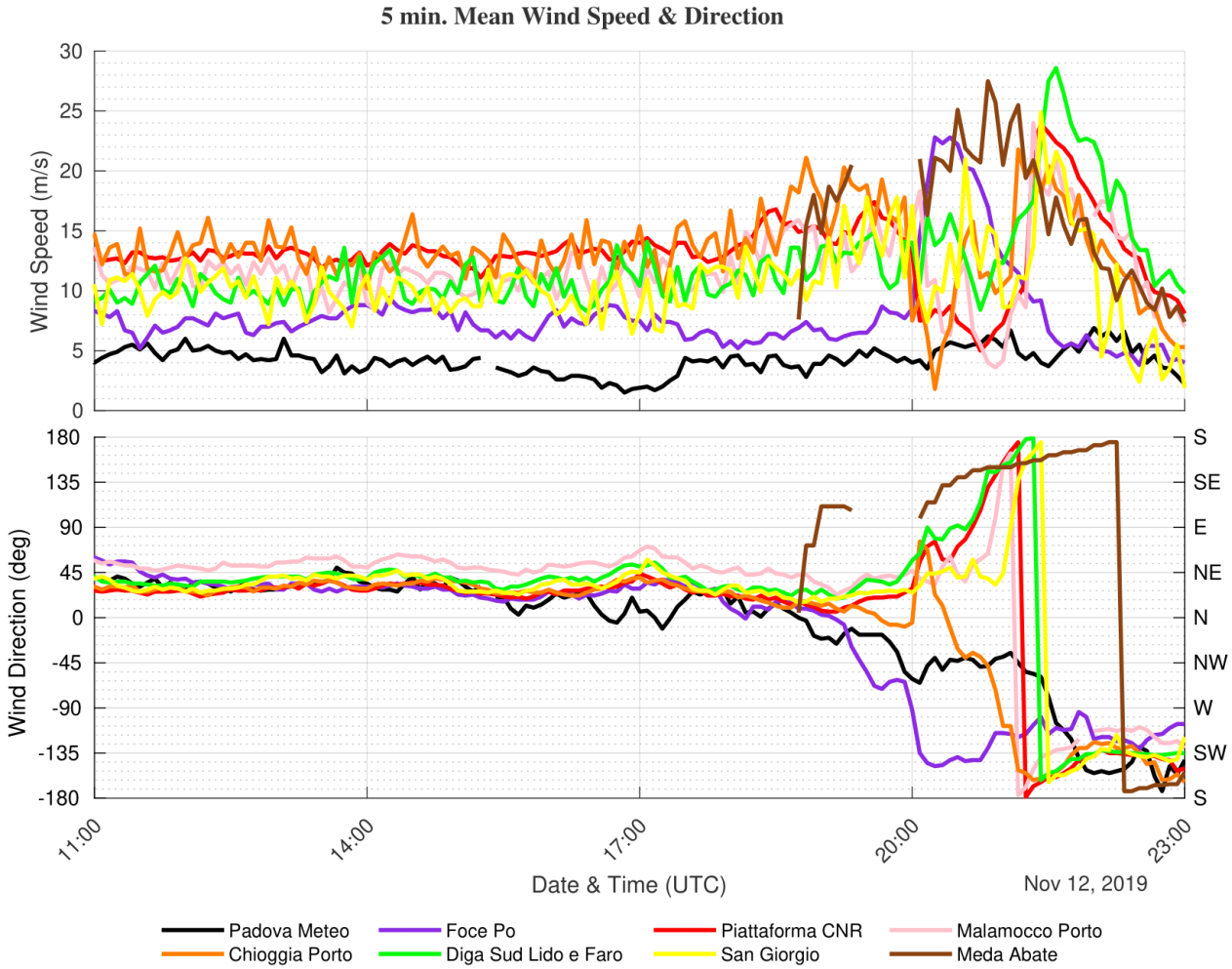

Figure 4.11: *Five minutes average wind speed (top) and direction (bottom) recorded by weather stations.*

stations record winds from the southwest. This direction will be reported by all weather stations after 21:00 UTC. Regarding wind speed, the peaks are reached by the Meda Abate station (more than 27 m/s from the south-southeast) and a little later by the weather stations in the center of the lagoon in conjunction with the wind rotation to the southwest direction, with a peak higher than 28 m/s at the Diga Sud Lido e Faro.

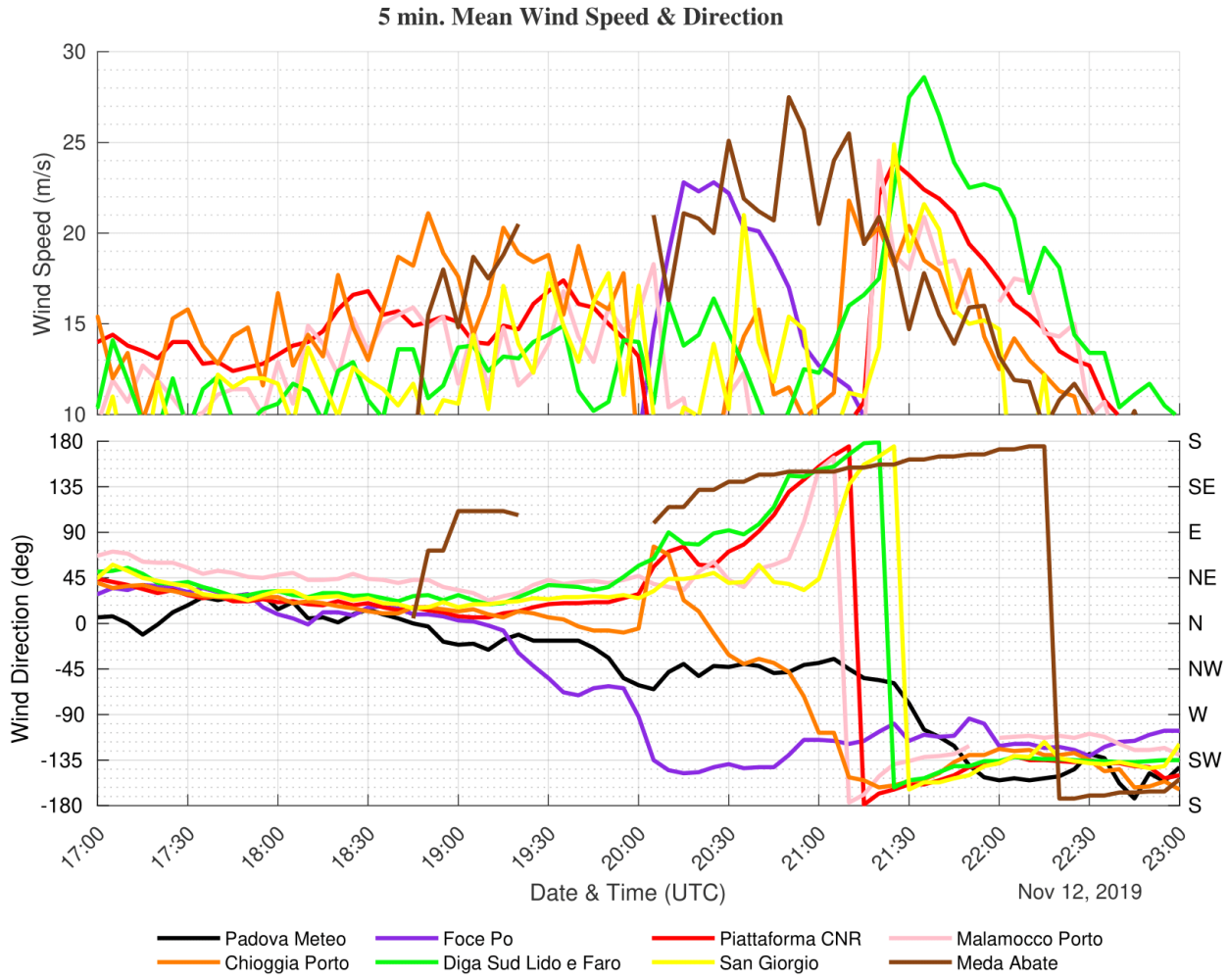

Figure 4.12: *Five minutes average wind speed peaks (top) and direction (bottom) recorded by weather stations.*

In figure 4.12 the wind peaks and their direction reached in the evening can be better visualized, with the highest speed values reached, after the wind rotation to the southwest, with the exception of the Meda Abate station. Padova Meteo data do not appear in the plot above, due to low wind speeds.

4.3.4 Sea Surface Temperature

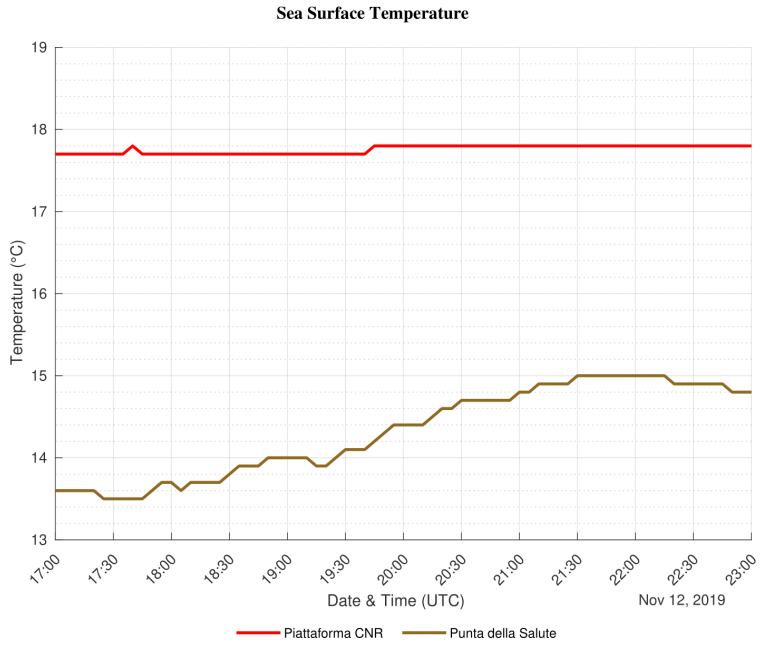

Figure 4.13: *Sea surface temperature trend at Piattaforma CNR and Punta della Salute.*

Figure 4.13 shows the sea surface temperature values recorded in the second part of the day of November 12 by the two stations of Piattaforma CNR and Punta della Salute, that is a station located in the open sea and an urban one that instead measures the water temperature data of the Grand Canal. We note the almost constant sea surface temperature of the waters of the Piattaforma CNR on a value just below 18°C and instead the increase in temperature, starting from about 18:00 UTC, recorded at Punta della Salute, from a value of about 13.5°C to a value of 15°C in less than four hours. The increase in temperature in the lagoon seems to be due to the increase in average wind speed and its rotation, which pushed warmer waters from the open sea into the lagoon, and consequently into the Grand Canal.

4.3.5 Map visualization of wind barbs and indicative cyclone path

In order to obtain a better visualization of wind data, maps with NCL have been created. Wind barbs for each weather station are reported on the maps. Figure 4.14

shows maps of six significant time steps.

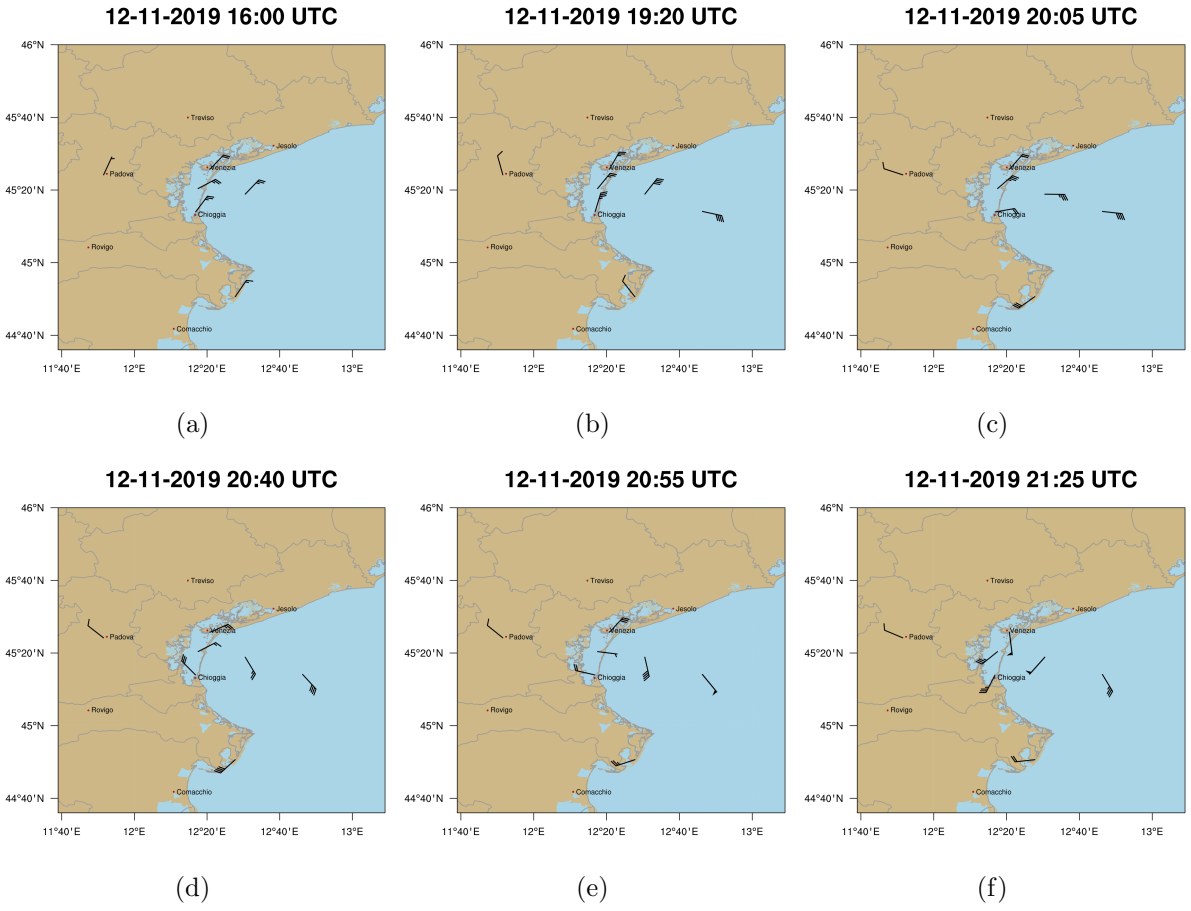

Figure 4.14: *Wind barbs on maps at six significant time steps during the cyclone transit.*

The first map referring to 16:00 UTC (figure 4.14(a)) shows a uniform situation before the approach of the cyclonic structure. The sustained Bora winds have been blowing for several hours and are still present in the afternoon, as is evident from the map. In the next time step of 19:20 UTC (figure 4.14(b)) we note the rotation of the wind in the open sea (Meda Abate) and on the Po delta, in opposite directions, while the Bora wind continues to blow in the lagoon. The presence of a cyclonic structure in the sea between the Meda Abate and Foce Po stations can be drawn. Moving on to the situation at 20:05 UTC (figure 4.14(c)), we observe the rotation to the eastern quadrants

in the Piattaforma CNR and Chioggia Porto stations, while in Foce Po the wind assumes a southwestern direction, a clear sign of the cyclone located on its north-eastern side. At 20:40 UTC (figure 4.14(d)) we note the sudden change in wind direction in the Chioggia Porto station and the anticlockwise rotation around the cyclone, which now seems to be positioned in front of the southern lagoon; its movement towards the northwest looks evident at 20:55 UTC (figure 4.14(e)), with the further rotation of the wind barbs and the drastic decrease in wind speed in the Malamocco Porto station. Finally, at 21:25 UTC (figure 4.14(f)) strong winds from the south-southwest can be seen in all the lagoon stations.

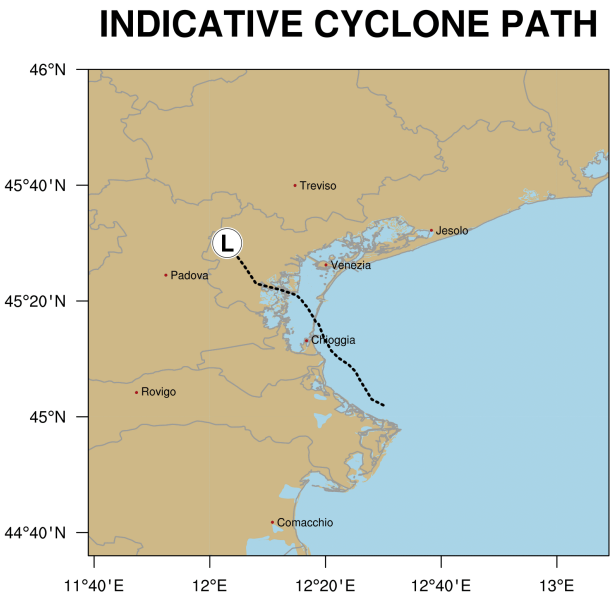

Figure 4.15: *Indicative cyclone path obtained from wind data.*

Based on the wind directions and speeds represented on these maps, the cyclone has been approximately positioned from the time it appears in front of Meda Abate and Foce Po stations until it recedes to the northwest on the Venetian Po valley. Its indicative path is shown in figure 4.15. From this approximate elaboration, carried out on the basis of the directions and intensities indicated by the wind barbs every 5 minutes, it can be said that the cyclone has assumed a trajectory with a southeast-northwest orientation in this landfall phase, crossing the central-southern part of the Venetian lagoon, i.e. passing to the southwest of the city of Venice. This is a slightly different trajectory compared to that in CPSM et al. (2020).

As can be seen in figure 4.16, at 21:55 UTC the cyclone is positioned southeast of the

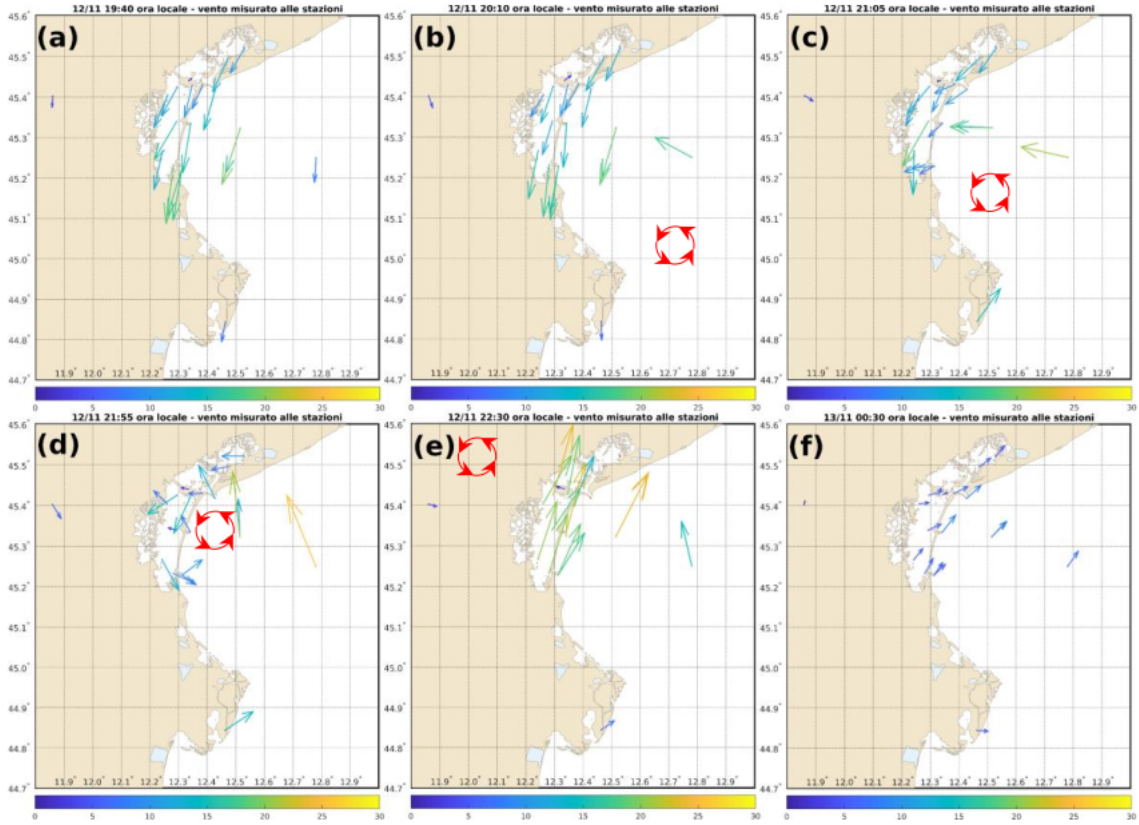

Figure 4.16: *Hypothetical position of the cyclone shown in the CPSM, ISPRA and CNR-ISMAR report. (CPSM et al., 2020)*

city of Venice, a few kilometers north of the elaboration presented in figure 4.15. However, the cyclone path pelaborated here appears to be the most consistent with the data of the selected weather stations. Although small, the difference is however considerable if we consider the impact that an inappropriate location of the cyclone by a few kilometers can bring in terms of accurate forecast of the timing and intensity of a high tide in the city.

Chapter 5

Numerical simulations

In order to study the atmospheric phenomenon responsible for the observed effects shown in the previous chapter, several simulations were carried out with the WRF model. We looked for the setting that led to a result as close as possible to the observations, also to understand if and how far in advance the event was predictable. It goes without saying how important it is to correctly predict such intense and localized phenomena, also in light of the constant increase in their intensity. In this chapter, therefore, the WRF model settings used to carry out the different simulations will be discussed, which will subsequently be compared with each other, analysing their outputs. Specifically, for each simulation, the lowest pressure value found in the area affected by the cyclone, the path of the cyclone itself (i.e. the location of the minimum pressure value in each time step), and the equivalent potential temperature field at 950 hPa will be analysed. After comparing the three different control runs, starting at different initial times, simulations in which the heat fluxes between the atmosphere and the surface have been turned off will be analysed, in order to evaluate how much they affect the deepening of the cyclone. Also, additional simulations are carried out changing the way convection is represented with respect to the control run. Finally, convection and vorticity outputs are analysed in detail, observing in the latter case how the forecast changes among the simulations.

5.1 WRF model settings

The simulations were run with the WRF-ARW model, configured, compiled and executed on the cluster of ISAC-CNR, Lecce (CNR-ISAC, 2019). Eight simulations are analysed in total and each one is named in order to be immediately recognizable. The first three simulations (*1112*, *1200*, *1212*) are considered as *control runs*, i.e. including the standard configuration used in the experiments with the full physics. They take their name from their starting day and time, respectively on November 11 at 12:00 UTC, on November 12 at 00:00 UTC and on November 12 at 12:00 UTC. The initial conditions are provided by the analysis issued by the global GFS model valid for the same starting time of the run, with a grid resolution of 0.25°. Subsequently, the boundary conditions from the same model were also provided from the GFS model forecasts every 3 hours for the entire duration of the run, again with a grid resolution of 0.25°.

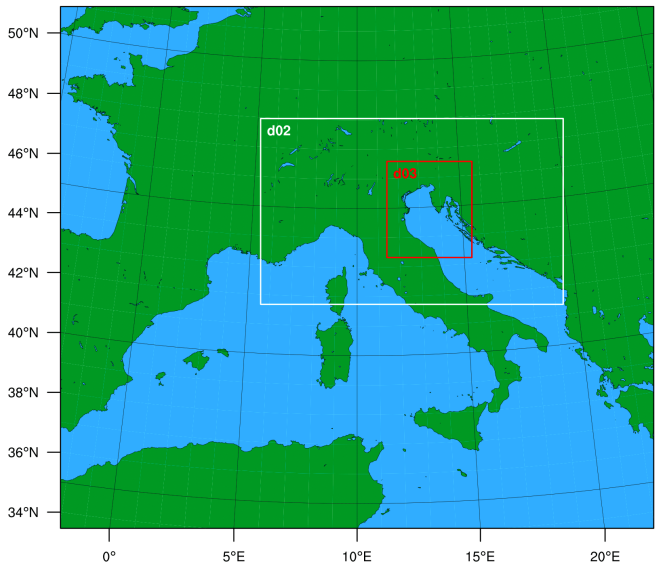

Figure 5.1: *WRF parent domain, with the two nested subdomains (*d02 *and* d03*).*

Figure 5.1 shows the geographical domains used for the simulations: in addition to the parent domain, with a grid spacing of 9 Km, two other subdomains d02 and d03 are inserted, respectively with a grid spacing of 3 and 1 Km. The higher resolution subdomain d03 focuses exclusively on the area affected by the cyclone during its most intense phase. The time step used for the integration is 36 seconds; it was however verified that variations in its value did not lead to significant changes in simulations results. The type of microphysics used is number 8, which corresponds to the *Thompson graupel*

scheme, with six classes of moisture species plus number concentration for ice as prognostic variables (Thompson et al., 2004). Fluxes of heat and moisture from the surface are activated. On the other hand, the feedback mechanisms from the nested subdomains to the parent ones are not activated (1-way nesting). About the vertical subdivision into levels of the atmosphere and soil, they have been divided into 34 and 4 levels respectively. In the end, the type of parameterization used for convection is the updated *Kain-Fritsch scheme* (Kain, 2004). This parameterization scheme is used in the larger domains at 9 and 3 Km grid spacing, while convection is explicitly solved in the smaller domain d03 at higher resolution. For each of the three control runs, another simulation was performed by deactivating the heat and moisture fluxes from the surface (*ISFFLX = 0*). The other parameters have not been changed. These three simulations fall under the denomination of *NF*. Run 1212 (considered as the closest to the observations, as we will see later in the analysis) is selected for additional analysis; for example, for this configuration the behavior of the model is analysed by explicitly solving convection in both subdomains d02 and d03 (*CP100* run) and in all domains (*CP000* run), keeping all the other parameters unchanged. Longwave radiation was treated with the Rapid Radiative Transfer Model (*ra_lw_physics = 1*), an accurate scheme using look-up tables that accounts for multiple bands, trace gases and microphysics species (Mlawer et al., 1997); shortwave radiation was instead parameterized with the Dudhia scheme (*ra_sw_physics = 1*), which consists of a simple downward integration allowing for efficient cloud and clear-sky absorption and scattering (Dudhia, 1989); the surface-layer was considered using a scheme (*sf_sfclay_physics = 1*) based on Monin-Obukhov with Carslon-Boland viscous sub-layer and standard similarity functions from look-up tables (Jiménez et al., 2012); for the land-surface the Noah Land-Surface Model was used (*sf_surface_physics = 2*), a unified NCEP/NCAR/AFWA scheme with soil temperature and moisture in four layers, fractional snow cover and frozen soil physics (Tewari et al., 2004); lastly, for the boundary layer the Yonsei University scheme was used (*bl_pbl_physics = 1*), in which the

entrainment (Hong et al., 2006) processes are explicitly treated.

Once the model settings have been presented, we move to the simulation analysis in the next section.

5.2 General cyclone analysis

Before comparing the different simulations carried out with the WRF model, the cyclone under consideration and the way the model outlines the meteorological dynamics in the area of interest are analysed.

To do this, we start by observing the map in figure 5.2, extrapolated from the 9 Km grid spacing domain of 1212 run and valid for November 12, 2019 at 18:00 UTC, which shows the sea level pressure and the 10 m wind direction and speed fields.

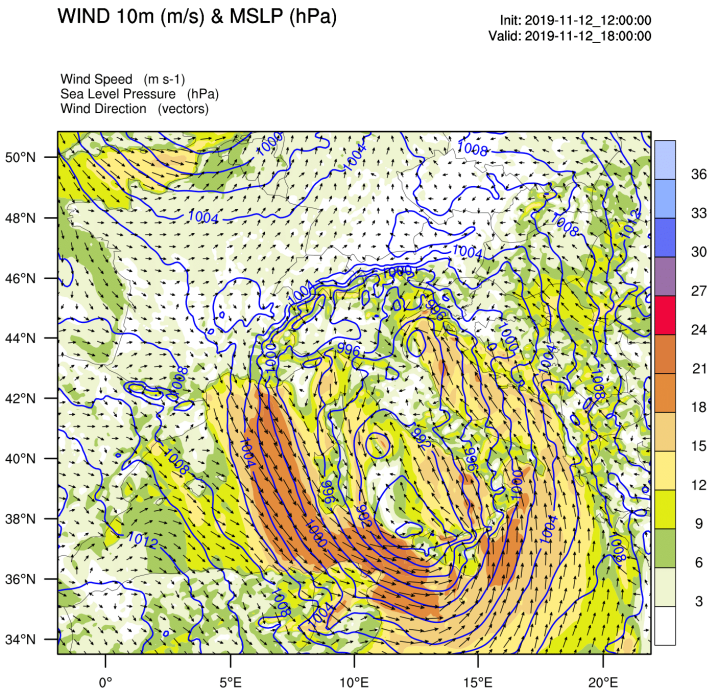

Figure 5.2: *WRF model, 1212 run - Mean sea level pressure (blue lines) and 10 m wind direction and speed (vectors and colours), valid for November 12, 2019 at 18:00 UTC - 9 Km grid spacing domain.*

A large cyclonic circulation is observed, with a minimum of about 988 hPa located on the southern Tyrrhenian Sea. Sea level pressure increases on North Africa and on the Iberian Peninsula, while in the northwest of the domain another cyclonic circulation is visible on the English Channel. A small cyclonic structure is instead found on the North Adriatic, identified as

the cyclone that is the object of the present work. Strong Mistral winds blow on the western side of the Tyrrhenian cyclonic circulation, with the wind that subsequently whirls around the minimum orienting from the southern quadrants on the Ionian Sea and from the south-east (Sirocco) on the Adriatic Sea. However, we observe the rotation of the winds around the minimum near the Po river mouth, with the Bora wind blowing on the Triveneto and the weak north-westerlies on the Emilia-Romagna. Hence, the simulation is consistent with large-scale analyses.

In figure 5.3 the same fields at the same time as in figure 5.2 are shown and processed, however, in the domains with higher resolution: the 3 Km grid spacing domain, with a focus on central and northern Italy, is shown above (figure 5.3(a)), while the 1 Km grid spacing domain, with a focus on the North Adriatic is presented below (figure 5.3(b)). Especially in the latter map the cyclone minimum is clearly visible with its lowest value below 992 hPa and the winds that blow around it, with speeds locally higher than 20 m/s. In this regard, note the strong convergence between the Sirocco and Bora winds near the minimum: the counterclockwise rotation indicates positive cyclonic vorticity (Holton, 2004).

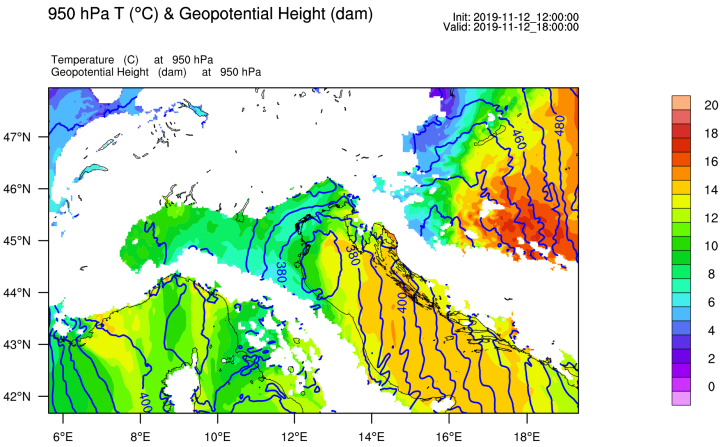

Figure 5.4: *WRF model, 1212 run - 950 hPa air temperature and geopotential height fields, valid for November 12, 2019 at 18:00 UTC - 3 Km grid spacing domain.*

Analysing the temperature and geopotential height at 950 hPa (figure 5.4), the cyclonic structure is observed to be immersed in milder air. Colder air enters the Po Valley from the northeast and is pushed against the northern slope of Tuscan-Emilian Apennines. Meanwhile a warm air tongue stretches

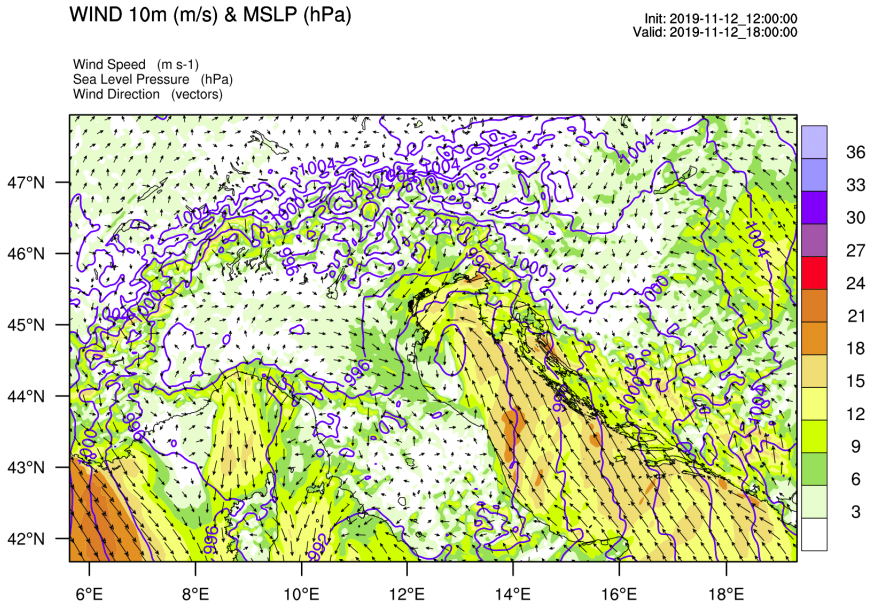

(a)

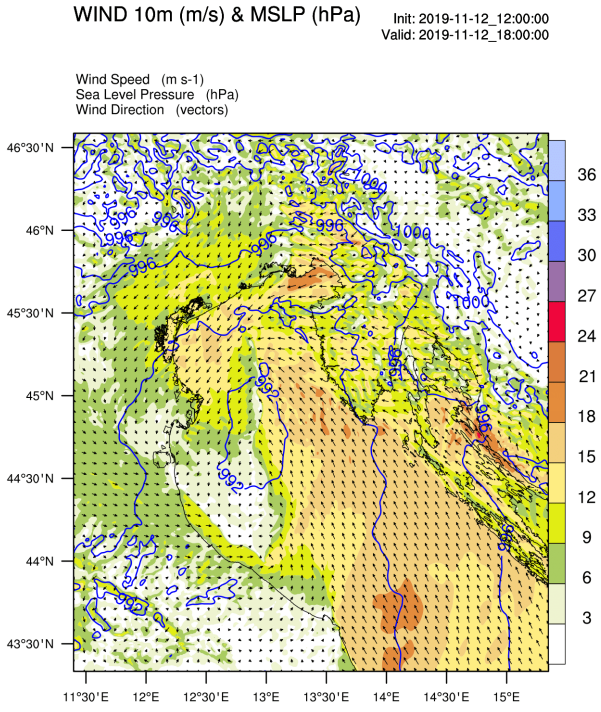

(b)

Figure 5.3: *WRF model, 1212 run - Mean sea level pressure (blue lines) and 10 m wind direction and speed (vectors and colours) , valid for November 12, 2019 at 18:00 UTC* - a) *3 Km and* b) *1 Km grid spacing domains.*

along the Adriatic, pushed by the southern winds that persist in the basin.

This configuration is even more evident two hours later at 850 hPa (figure 5.5), when the cyclone has moved farther northwest over the Venice lagoon. Here we can clearly observe the cyclonic structure that resides inside the milder air mass. Note the strong horizontal thermal gradient between the cold air drawn into the Po valley (with a minimum value approaching 0°C at 850 hPa) and the milder air in which the cyclone develops (with a maximum value around 8°C at 850 hPa). Warm air around the cyclone is evident even at 700 hPa (figure 5.6(a)), while the situation at 500 hPa (figure 5.6(b)) is less defined, with slightly milder air in correspondence with the Po valley and colder air flowing towards the North Adriatic from the southeast.

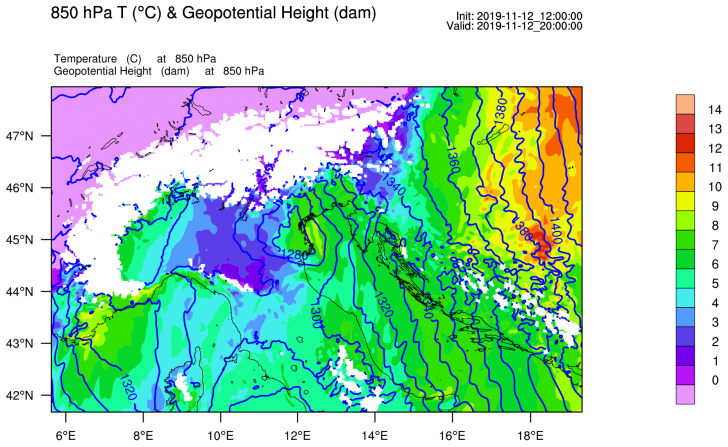

Figure 5.5: *WRF model, 1212 run - 850 hPa air temperature and geopotential height fields, valid for November 12, 2019 at 20:00 UTC - 3 Km grid spacing domain.*

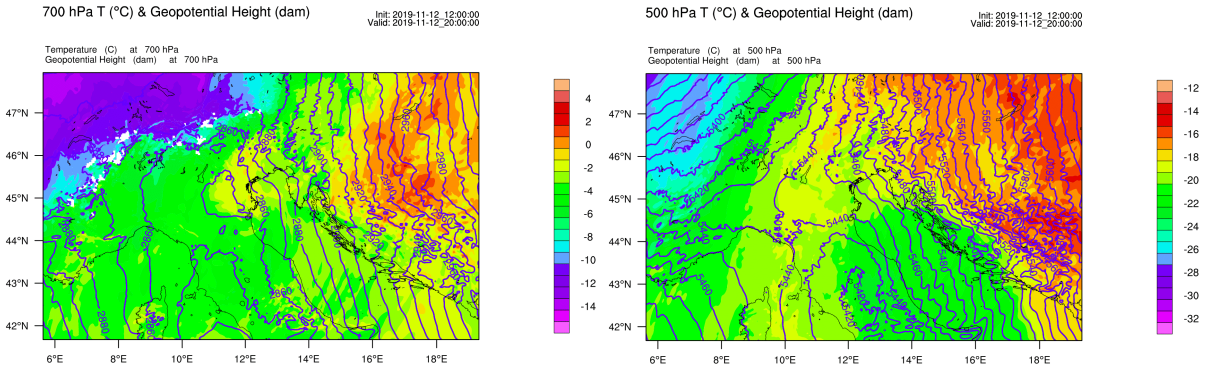

(a) *700 hPa* (b) *500 hPa*

Figure 5.6: *Air temperature and geopotential height fields at*)a) *700 hPa and* b) *500 hPa, valid for 20:00 UTC of November 12, 2019 - 1212 run, 3 Km grid spacing domain.*

From these considerations it can be deduced that the cyclone has a shallow warm core in the lower layers, while it is not well defined at the upper levels. We will explore whether the development of the cyclone is typical of some warm core cyclones occasionally observed at these latitudes (known as *tropical-like cyclones* or *medicanes*), in which a very important role is played by the surface heat fluxes and by the latent heat released by convection (Miglietta and Rotunno, 2019). However, this issue will be addressed only after having analysed and compared the three different control runs in the next section.

5.3 Control simulations comparison

In this section the control runs 1112, 1200 and 1212 are examined and compared with each other, in order to understand the skill of the cyclone forecast elaborated in the 36 hours prior to the event, depending on the initial and boundary conditions provided by the GFS model. For each simulation the lowest value of the sea level pressure is identified, as its geographic coordinates, in order to trace the trajectory of the cyclone.

Given the noise that the complex orography causes especially on the sea level pressure field, and given the presence of other sea level pressure minima in the larger domain, it was necessary to create a subdomain to consider only the mean sea level pressure data in the Adriatic Sea and the Po Valley, in order to exclude the mountain ranges and other barometric structures. To do this, a shapefile (*kmz* format file, transformed in *shp* format afterward through QGIS software) was created through the Google Earth software and subsequently introduced in the NCL scripts, where the data were masked outside the shapefile.

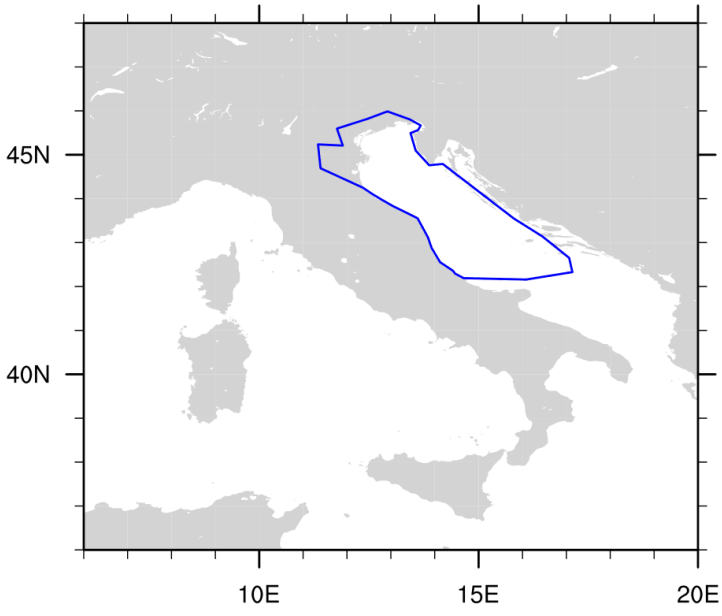

Figure 5.7: *NCL - Shapefile area is highlighted by the blue line.*

In figure 5.7 the area selected by the shapefile can be observed, highlighted by the blue line. The area was chosen to fall within the limits of the smallest 1 Km grid spacing subdomain and to exclude the disturbance sources. In fact, the blue line follows the Italian coastline and includes only the flat coastal parts of Triveneto and Romagna, in order to include the cyclone in the final part of its path.

5.3.1 Sea level pressure minimum

In this subsection the three control runs are compared on the basis of the minimum pressure value evolution. In this way it is possible to evaluate the simulation for which the minimum value is the closest to the real values observed by the weather stations.

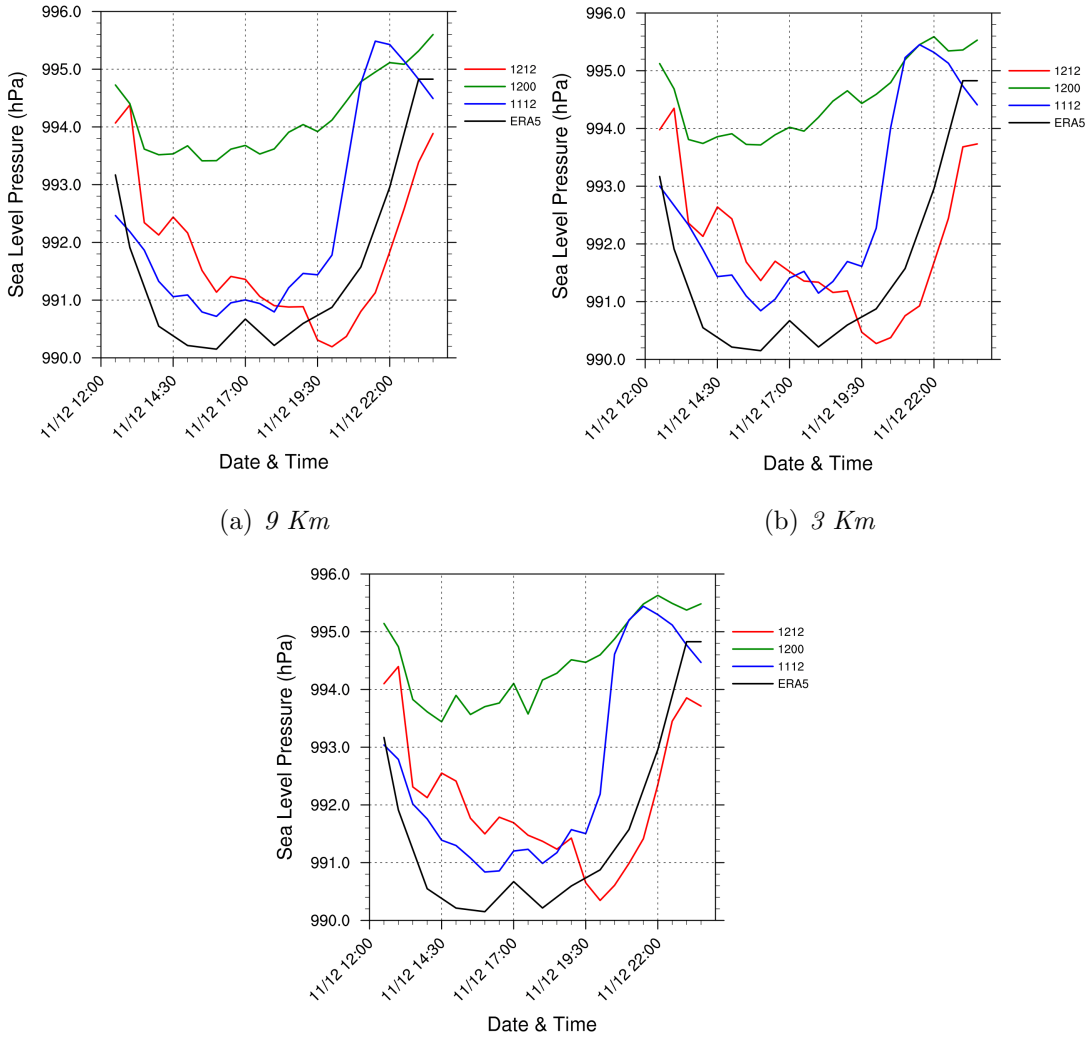

(a) *9 Km* (b) *3 Km*

(c) *1 Km*

Figure 5.8: *Minimum mean sea level pressure value found at* a) *9 Km grid spacing domain,* b) *3 Km grid spacing domain and* c) *1 Km grid spacing domain. - Control runs.*

Figure 5.8 shows the minimum sea level pressure value evolution from 12:00 to 23:30

UTC on November 12, 2019 for the 1112, 1200 and 1212 control runs, represented respectively by the blue, green and red lines, and for the ERA5 reanalysis, represented by the black line. The three panels refer to the three domains with different grid spacing. The lowest values are reached by the 1212 run, with sea level pressure values close to 990 hPa at 20:00 UTC. Values slightly lower than 991 hPa are instead reached by 1112 run, but with different timing compared to 1212 run: the minimum value is reached at around 16:00 UTC, then the pressure remains around those values until 18:00 UTC, to quickly rise again afterward. It is a different timing compared to 1212 run, in which the sea level pressure drops more or less constantly until it reaches the minimum value at 20:00 UTC. The 1200 run provides a different evolution, with the minimum value between 994 and 993.5 hPa reached around 15:00 UTC, followed by a gradual rise in pressure values. The ERA5 reanalysis trend is very close to the 1112 run, with pressure values however a little lower, being the minimum value almost 990 hPa, so it is more distant from the observed timing compared to the 1212 run.

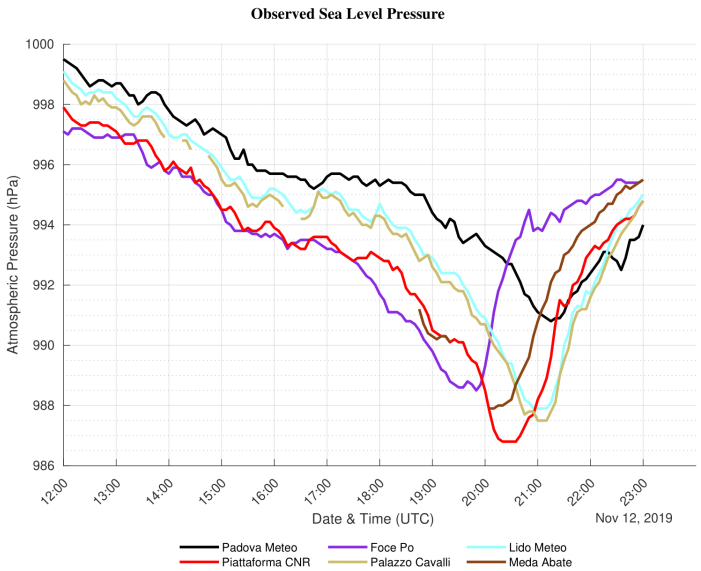

Figure 5.9: *Sea level pressure observed by weather stations.*

In fact, by comparing the simulations with the values actually observed by the weather stations (figure 5.9), the trend results in a generalized and constant decrease starting from 12:00 UTC in the latter, with the achievement of the minimum value in the lagoon between approximately 20:00 and 21:00 UTC; the trend and timing are very similar to those of the 1212 run. The values resulting from the

simulations (no lower than 990 hPa) are higher than those recorded in the lagoon (around 987 hPa). Not even the ERA5 reanalysis is able to reach similar values. We point out that the comparison takes place between the minimum value reached in the simulations by the cyclone and the punctual values recorded by weather stations, therefore values lower than 987 hPa (recorded at Piattaforma CNR) may have been actually reached.

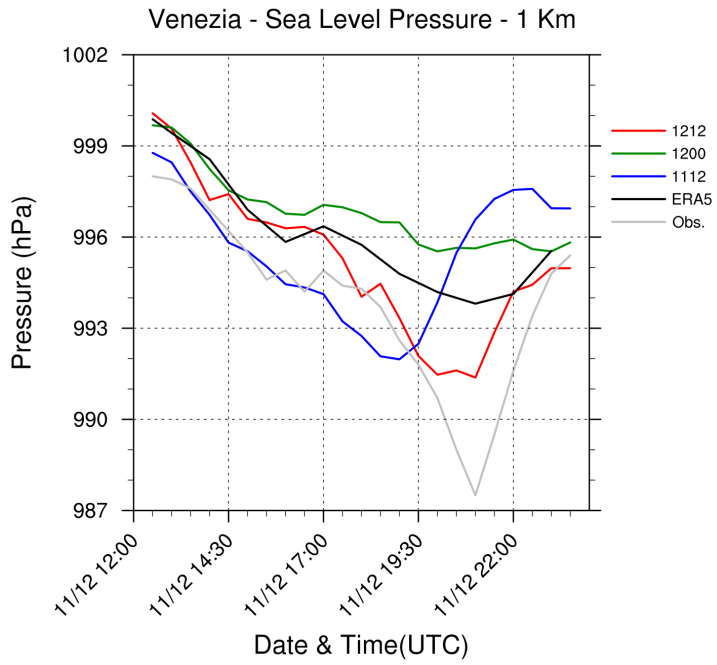

Figure 5.10: *Sea level pressure value at Venice - Control runs and observed value (Palazzo Cavalli weather station) - 1 Km grid spacing domain.*

As an example of comparison in fixed grid points, the sea level pressure data at the city of Venice in the 1 Km grid spacing simulations are shown in figure 5.10. Here the values are perfectly comparable since they are punctual data in any case: the gray line (*Obs.*) shows the data observed at the Palazzo Cavalli weather station in Venice, while the simulations refer to the grid point closest to the station. Here too it can be observed that the 1212 run is consistent with the observations, and the timing of the cyclone transit (the pressure minimum) almost coincides with the data. The overestimation of about 4 hPa remains, but the improvement with respect to the other runs and to the ERA5 reanalysis are evident.

A comparison between the sea level pressure observed at Palazzo Cavalli and that forecasted on the grid point closest to the city of Venice by the BOLAM and COSMO-LAMI limited area models, and by the global model of the ECMWF, was presented in

CPSM et al. (2020) and is shown in figure 5.11.

Also in this case, a fairly consistent trend is observed between the sea level pressure values observed and those predicted by the models, but the detail of the intensity of the cyclone is lost, which is fundamental for the correct forecast of wind intensity in the lagoon and for its impact. In fact, these models report a value that does not fall below 992 hPa, compared to an observed value of less than 988 hPa. This behaviour is consistent with that shown in the WRF-model runs, where a minimum value of about 991.5 hPa was recorded (figure 5.10). Hence, in all runs the sea level pressure value remains overestimated.

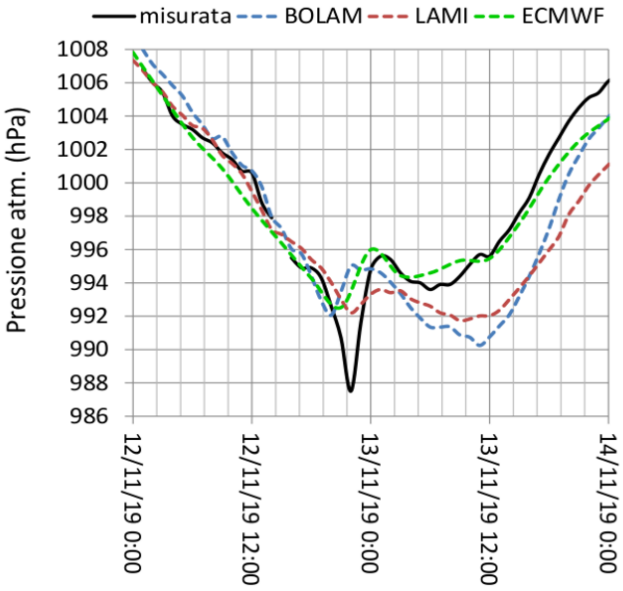

Figure 5.11: *Sea level pressure value at Venice - Forecasted value by the global model of ECMWF (green dashed line) and by the limited area models COSMO-LAMI (red dashed line) and BOLAM (blue dashed line). The observed value is recorded at Palazzo Cavalli (black solid line). Source: (CPSM et al., 2020)*

5.3.2 Cyclone tracking

By finding the geographic coordinates of each minimum value in each time step, the path taken by the cyclone, according to each simulation, can be obtained. The results for the three domains with different grid spacing are shown in figure 5.12.

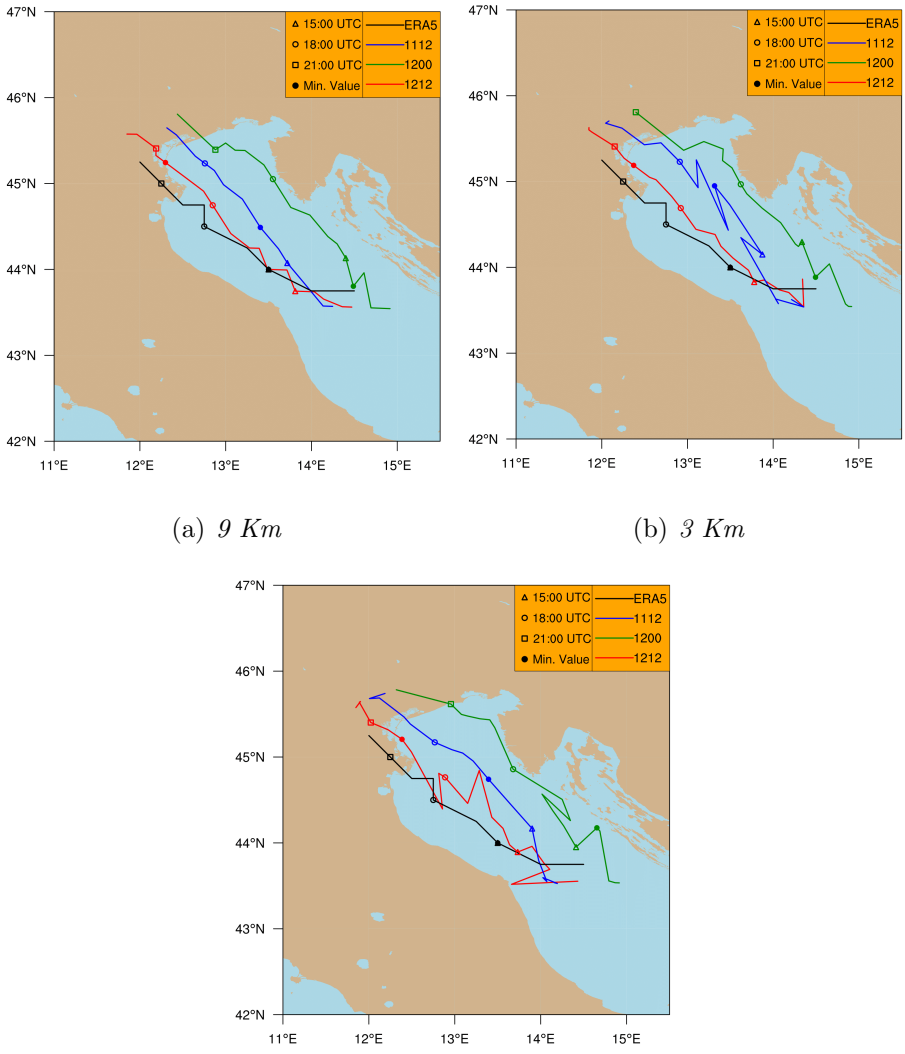

(a) *9 Km* (b) *3 Km*

(c) *1 Km*

Figure 5.12: *Cyclone track at* a) *9 Km grid spacing domain,* b) *3 Km grid spacing domain and* c) *1 Km grid spacing domain - Control runs and ERA5 reanalysis.*

They represent distinct scenarios: 1112 and 1212 runs see the cyclone entering the

Venetian lagoon, the first with a more eastern trajectory, that approaches the northern area of the lagoon, the second with a more western trajectory, which instead involves the southern area; 1200 run traces a much more eastern trajectory, with the cyclone moving near the coasts of Istria and concluding its path to the northeast of the lagoon; the ERA5 reanalysis, on the contrary, traces a more western trajectory than the WRF simulations, with the cyclone landfall on the Po river delta. Almost no differences are observed between the different domains: some spikes in the 3 and 1 Km grid spacing are probably because of the finer grid, in which contiguous points can assume values very close to each other at the same time.

An additional indication on the timing of the cyclone movement comes from the markers, each of which is associated with a different time as indicated in the legend. The marker with the filled circle, on the other hand, indicates the moment in which the lowest sea level pressure value of the entire time series is reached. Only the 1212 run is in good agreement with the movement timing of the cyclone. There are differences in the timing: the 1200 run sees a very early minimum value, probably also due to the proximity of the track to the mainland; ERA5 reanalysis and 1112 run also see a rather early minimum value in the open sea, while

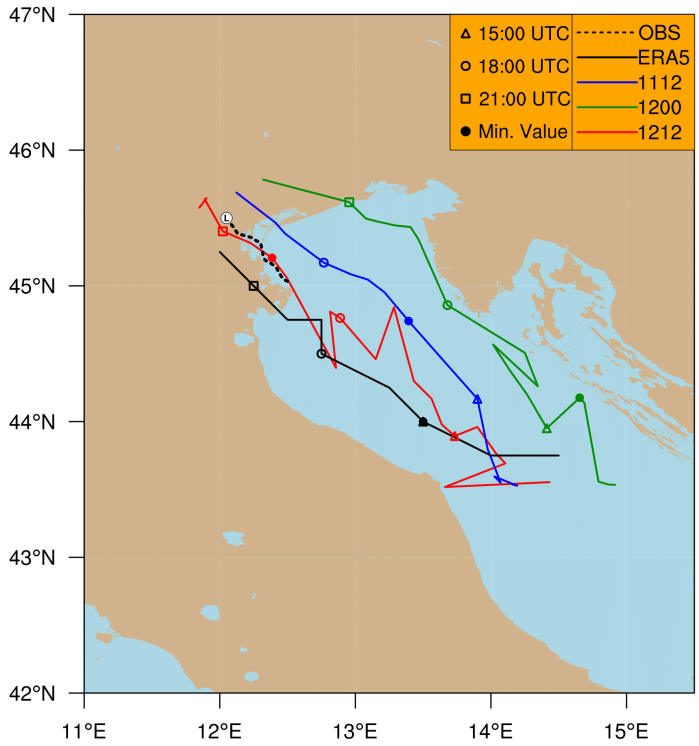

Figure 5.13: *Cyclone track at 1 Km grid spacing domain - Control runs, ERA5 reanalysis and indicative observed path.*

1212 run locates the lowest value right at the moment of cyclone entry into the lagoon.

In figure 5.13 are plotted the details of the trajectories of the control runs in the 1 Km grid spacing domain, that of the ERA5 reanalysis and that observed. It is immediately evident how the cyclone's trajectory from the 1212 run is similar to that obtained from the observations. The timing of the lowest sea level pressure value also seems to be in line with the observations shown in figure 5.9. More distant from the correct timing and positioning are the other simulations, and surprisingly also the ERA5 reanalysis. Therefore the 1212 run seems to be the simulation that comes closest to the observations of the phenomenon, both in the timing and in the strength of the cyclonic structure.

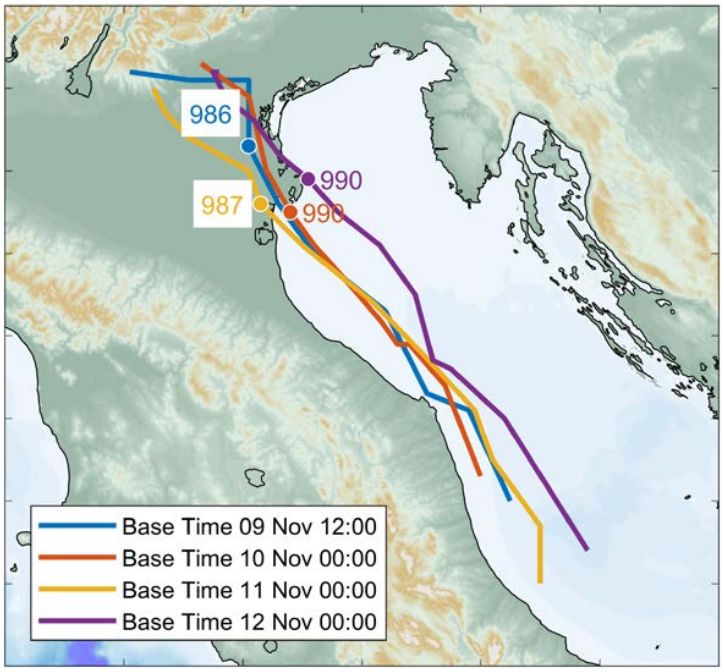

Figure 5.14: *Cyclone track for November 12 at 12:00-24:00 UTC according to the ECMWF forecasts (see legend for the base time) - Location (circle) and value (in hPa) of the sea level pressure minima are also shown. Source: (Cavaleri et al., 2020)*

For the sake of comparison, the cyclone tracks forecasted by the ECMWF global model are shown, as described in Cavaleri et al. (2020). Figure 5.14 shows four different trajectories, each associated with a different model output in the days preceding the event. Dates and times of the modeling releases are indicated in the legend. It can be observed that the model predicted a westernmost trajectory in the simulations started three days prior to the day of the event, and then positioned the cyclone more to the east in the run started at 00:00 UTC of November 12. At the same initialization time, the GFS-based WRF model run

gives the cyclone a much more eastern trajectory. Although the cyclone positioning by the last ECMWF run is closer to that elaborated with the observations, it is still slightly too western, compared to the 1212 run, which therefore hindcasts the closest trajectory to the observed one.

5.3.3 Equivalent Potential Temperature

In the discussion of this cyclonic structure the equivalent potential temperature (θ_e) is investigated in order to understand its characteristics, and in particular if the structure depends on convection and on air-sea fluxes, and if the warm core is actually powered by both of these factors, as it is for tropical-like cyclones, where a maximum of θ_e is observed in the cyclone core (Miglietta and Rotunno, 2019). In this regard, it is of fundamental importance to carry out simulations in which the air-sea heat fluxes are switched off, in order to understand more clearly the role of these factors in the intensification of the cyclonic structure.

The 950 hPa θ_e simulated by the three control runs for 18:00 UTC of November 12, 2019 is shown in figure 5.15. The highest resolution domain is used to provide more detail in the area affected by the cyclone. We observe two air masses that come into contact on the Northern Adriatic: a wide warm and humid air tongue moves northward along the Adriatic and comes into contact with colder and drier air that enters from the Northeast and invades the Po Valley, swirling around the western side of the cyclone. There does not seem to be an isolated maximum of θ_e in correspondence with the pressure minimum, but rather a large area of higher θ_e that contains the cyclonic structure at the inside. On the eastern part of the cyclone the maxima of θ_e can be noted, the position of which varies according to the trajectory of the cyclone.

Therefore, in the light of the results of the previous paragraph, there is a faster movement of the warm tongue for the 1112 run in figure 5.15(a), a more eastern trajectory

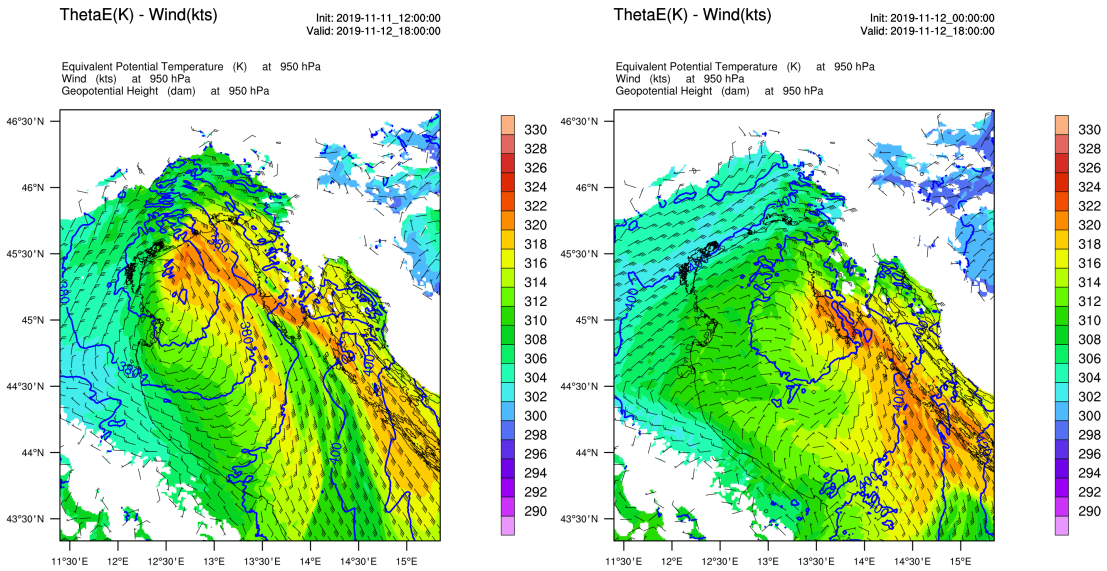

(a) *1112 run* (b) *1200 run*

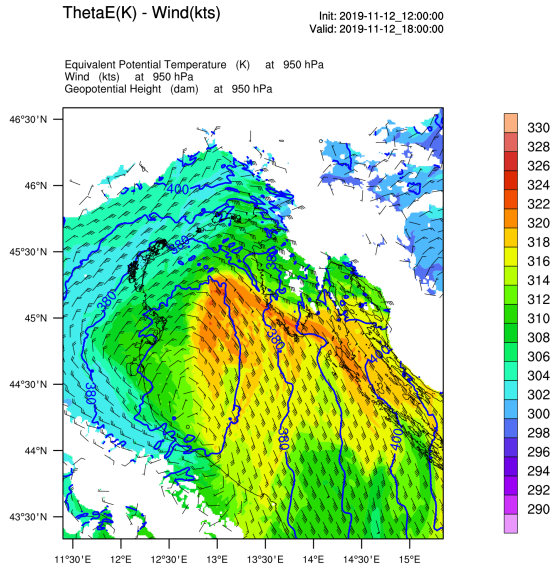

(c) *1212 run*

Figure 5.15: *Equivalent potential temperature (K), geopotential height (dam) and wind barbs at 950 hPa, forecasted by control runs - Valid for 18:00 UTC of November 12, 2019*

for the 1200 run in figure 5.15(b) while figure 5.15(c) shows that the warm tongue is positioned in the central of the northern Adriatic in the 1212 run. In all three cases, the warm and humid air seems to surround the cyclone, being followed to the south by the

incoming of air with lower θ_e values.

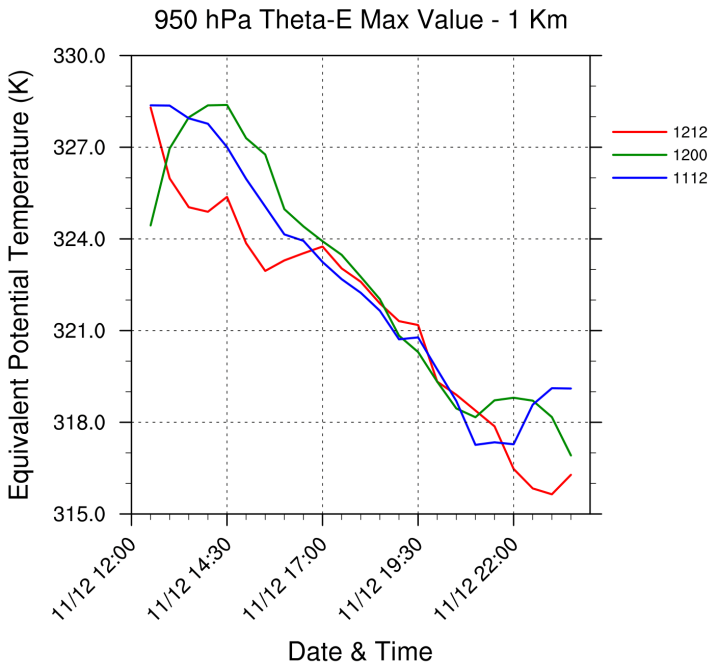

Figure 5.16: *θ_e maximum value trend (K) at 950 hPa - Control runs.*

To better analyse the evolution of the thermal field in the low levels, figure 5.16 shows the trend of the maximum value of θ_e in the domain considered for the three control runs. Apart from some discrepancies at the beginning of the considered time series, the predicted values are almost identical for all three simulations. The trend is very similar, with a decrease in the maximum value of about 10 K in 12 hours. The result is a reduction in temperature and humidity of the air as it moves northward along the Adriatic, probably due to the mixing with the cooler and drier environment that the air finds in its northward movement.

5.4 No-Fluxes simulations

In order to further investigate the factors that led to the deepening of the cyclone, three simulations were carried out (one for each control run) with the surface heat and moisture fluxes switched off. Given that the deepening of the cyclone takes place on the sea, it can be said that the air-sea interaction is turned off. The latter plays a fundamental role in the deepening of Mediterranean tropical-like cyclones, for the support they give to deep convection in terms of moist and warm air in the low levels, thus favouring a more

unstable environment. Therefore, if they are switched off and if the cyclonic structure depends on them, a marked increase in the minimum pressure values in the No-Fluxes simulations (NF) is expected. This sensitivity experiment is analysed with the same methods as the analysis in section 5.3, comparing the minimum pressure values found in the NF runs with those found in the control runs. The cyclone tracks and the maximum equivalent potential temperature values are then compared, considering only the 1 Km grid spacing domains, given the equality of the results among the three domains.

5.4.1 Sea level pressure minimum

The comparison between the control runs and the NF runs starts from the minimum sea level pressure value found in the time series of each simulation. The graph is shown in figure 5.17. Solid lines correspond to control runs, while dashed lines correspond to NF runs.

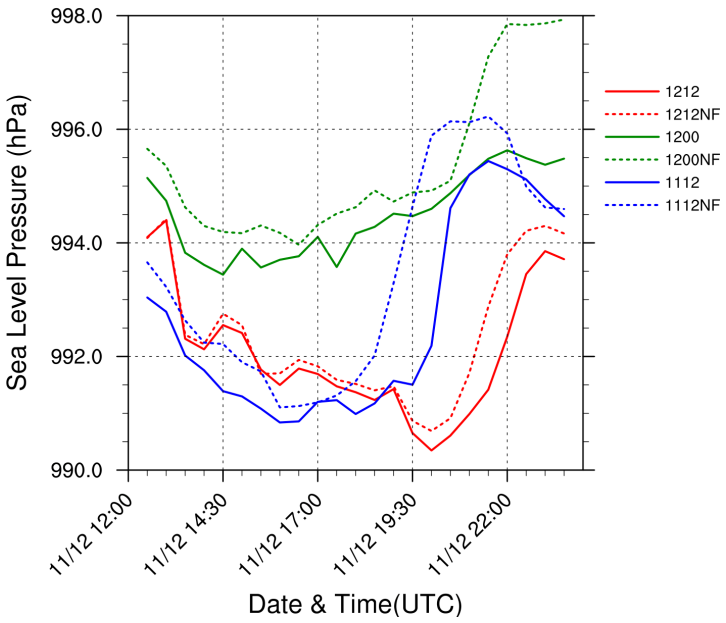

Figure 5.17: *Lowest mean sea level pressure value found at 1 Km grid spacing domain - Control and NF runs.*

Apart from switching off the fluxes, all other settings are unchanged, so they are the initialization and boundary data. The NF runs assume minimum sea level pressure values slightly higher than the control runs. For instance, the NF simulation of the 1212 run, the one most similar to the observed dynamics, assumes a higher value of only 0.5 hPa compared to the control run.

Note how the simulations with earlier starting time show greater

pressure difference between the control run and the corresponding NF run, compared to the 1212 run that starts at that time: this discrepancy is due to the longer time during which the fluxes are switched off. Anyway the discrepancy in minimum sea level pressure value of the 1112NF and 1200NF runs with the corresponding control runs remains very small, within at most a couple of hPa.

Thus the removal of the air-sea fluxes does not affect greatly the cyclone strengthening. It therefore seems that the dynamics of the cyclone are nearly independent of surface fluxes, making the hypothesis of a tropical-like nature of the cyclone not appropriate.

5.4.2 Cyclone tracking

Although the No-Fluxes simulations seem to underline the weak dependence of the cyclone on surface heat fluxes, it is interesting to observe how the trajectory of the cyclone varies with their suppression. In figure 5.18 the comparison between the NF trajectories and the control run can be observed.

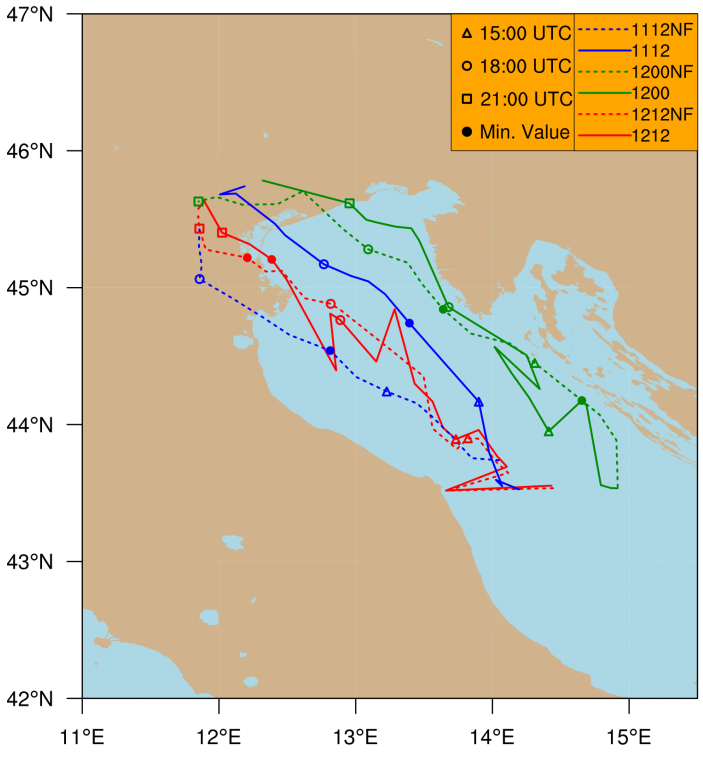

Figure 5.18: *Cyclone track at 1 Km grid spacing domain - Control and NF runs.*

1200NF and 1212NF runs seem not to undergo variations when the fluxes are switched off: the trajectories are almost overlapping. The 1112NF run cyclone track, on the other hand, is much more western than the 1112 control run, with the cyclone landfalling south of the Po

river delta; this trajectory is very close to that of the ERA5 reanalysis shown in figure 5.12. In this case, probably the earlier landfall is the cause of the anticipated increase of the minimum sea level pressure value of the 1112NF run, shown in figure 5.17.

5.4.3 Equivalent Potential Temperature

Once it has been observed that both the strength and the trajectory of the cyclone do not undergo large variations in the NF runs, we observe the time evolution of the maximum value of θ_e at 950 hPa to make a comparison with the control runs.

Figure 5.19 shows the trends of these values. Obviously, since the heat fluxes from surface are missing, the maximum values of θ_e are lower than those of the control runs of about 8 K. Less difference is found between the 1212NF run and the 1212 control run, due to the smaller time available for the departure from the control run.

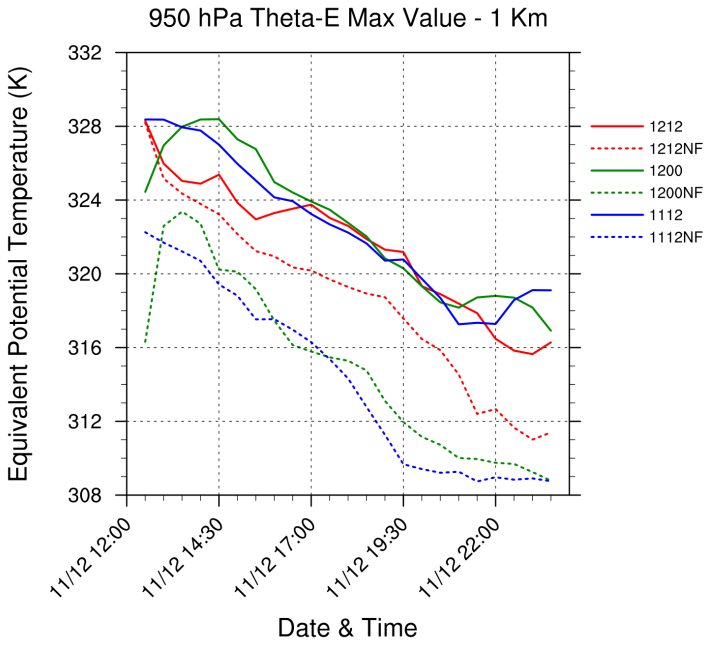

Figure 5.19: *θ_e maximum value trend (K) at 950 hPa at 1 Km grid spacing domain. - Control and NF runs.*

As there is a fairly marked difference between the NF and control run values, this indicates that the presence of sea surface fluxes is important to delay the decrease of θ_e in the warm advection, as it moves northward, However, as shown in figure 5.17, the impact on the cyclone intensification is only minor.

5.5 Cumulus physics simulations

Given the minor effects that switching off the heat and moisture surface fluxes has had on the cyclonic structure, the factors that led to the strengthening of the cyclone still remain to be understood.

We further explore the mechanism responsible for the cyclone intensification by analysing the convection around the cyclone. Considering the simulations in the two external grids are within or at the border of the *terra incognita* for cumulus parameterization, we perform two additional simulations with convection explicitly resolved also in the middle grid (CP100 parameters in the WRF namelist) or in all grids (CP000).

Since it has been widely demonstrated that the 1212 run is the closest to the observed evolution, the CP100 and CP000 simulations were carried out only with the initialization time of the 1212 run.

5.5.1 Sea level pressure minimum

The analysis of the CP100 and CP000 simulations begins with the comparison between the minimum sea level pressure values reached by the cyclone in these two simulations with the minimum values found in the 1212 run.

In figure 5.20 the plots relative to the comparison are shown. Taking a look at the trends, it can be seen that the 1212 run reaches the lowest sea level pressure value,

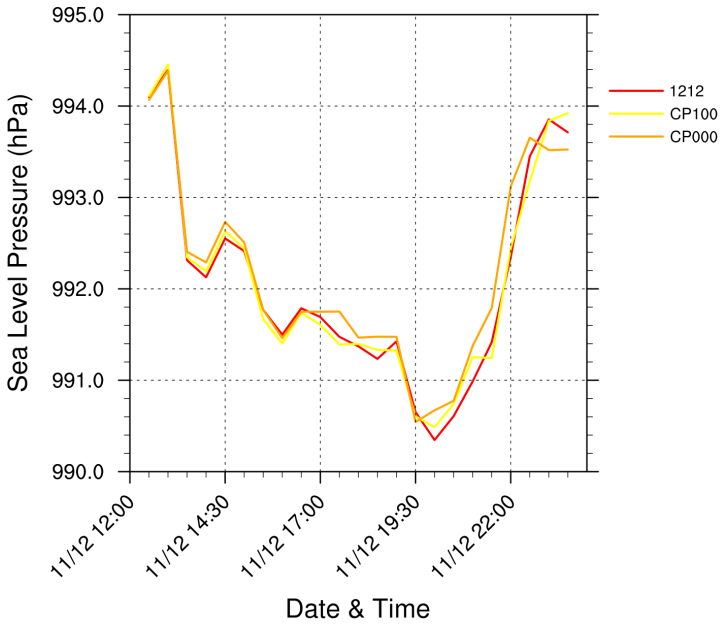

Figure 5.20: *Minimum mean sea level pressure value found at 1 Km grid spacing domain - 1212 control, CP100 and CP000 runs.*

and the two additional simulations are instead generally 0.2 hPa higher than the 1212 run, then a negligible difference is present.

In general, the change in the convection setting does not therefore change the result on the minimum sea level pressure recorded in the cyclone.

5.6 Convection analysis

This section will analyse the 1212 run and the intensity of convection simulated in the Northern Adriatic area for November 12, 2019. The background atmospheric conditions will then be analysed to assess whether there were favorable conditions for convection.

5.6.1 Background atmospheric conditions

The background atmospheric conditions will be presented below, to understand if they are favorable to the initiation and development of deep convection. All fields are taken from the 1212 run of the WRF model.

CAPE and CIN

Convective Available Potential Energy (CAPE) was originally introduced by Moncrieff and Miller (1976) and is commonly used to assess the potential for deep moist convection developing in the atmosphere. CAPE is defined as follows:

$$CAPE = R_d \int_{EL}^{LFC} (T'_v - T_v)\, d\ln p \tag{5.1}$$

where R_d is the gas constant for 1 Kg of dry air, EL is the equilibrium level, LFC is the level of free convection, T_v is the virtual temperature of the environment and T'_v is the virtual temperature of the rising parcel. Ignoring the small virtual temperature correction, the integral in the equation is the area, on a skew-T ln p plot, extending from LFC to EL and bounded by the environental temperature sounding on the left and a moist adiabat on the right (Wallace and Hobbs, 2006). Physically, CAPE measures the maximum kinetic energy per unit air mass (J/Kg) that can be reached within the convection of moist air from the lower layers of the troposphere (under the cloud base), thus it gives an upper limit to the cumulus vertical updraft speed. Convective Inhibition Energy (CIN) is another important variable used to determine the stability of the atmosphere to moist

convection. It is a measure of the energy required by a rising air parcel to reach its level of free convection (LFC).

Figure 5.21 shows the CAPE and CIN fields simulated at 18:00 UTC of November 12, 2019. Recalling the synoptic situation and the 10 m winds at the same time, shown in figure 5.3, the most relevant CAPE values are found in the south-eastern part of the cyclone, affected by the Sirocco winds. CAPE peaks around 800 J/Kg can be seen in the area closer to the cyclone, where Sirocco and Bora winds converge; the maximum values move northward following the cyclone evolution. At the same time, however, a large area of CIN values different from 0 is found in the zone affected by the higher CAPE.

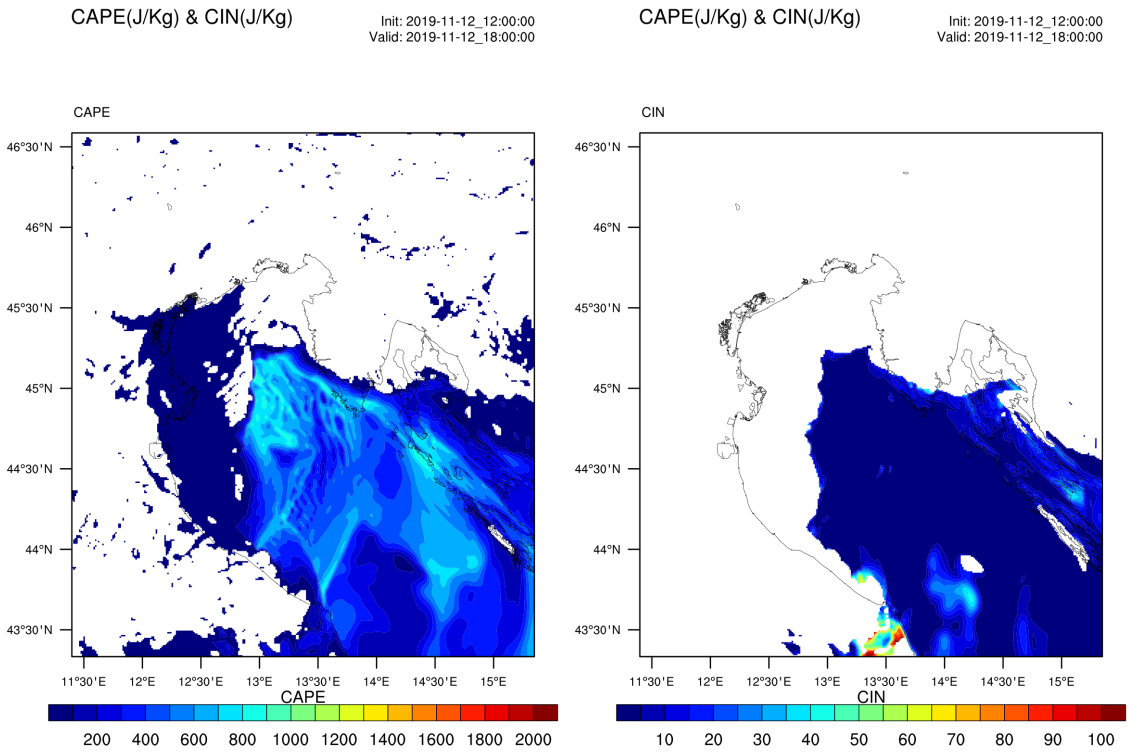

(a) *CAPE* (b) *CIN*

Figure 5.21: a) *CAPE (J/Kg) and* b) *CIN (J/Kg) forecast, valid for 18:00 UTC of November 12, 2019 - 1212 run, 1 Km grid spacing domain.*

In such a situation, convection development is limited. The CAPE values are not high; moreover the non-negligible CIN allows convection to develop only if it is supported

by a strong triggering mechanism. For this reason it appears reasonable that convection was triggered only in presence of obstacles or in the zones of low-level wind convergence. On the other hand, in the north-western part of the cyclone affected by the Bora winds the low values of CAPE can anyway favour some localized and shallow convection, given CIN close to 0.

Wind

The link between deep convection and upper and lower-level jet streams (ULJ and LLJ respectively) has been widely discussed in the literature. Riehl et al. (1952) stated that divergence zones in upper levels associated with velocities maxima (jet streaks) in the ULJ produce upward motion in the left-front (left exit zone) and right-rear (right entrance zone) quadrants of the jet streak. Some years later, the role of interaction between the streaks in LLJ and ULJ in the development of deep convection was emphasized by Beebe and Bates (1955), revealing the development of an area with upward motions at the intersection of LLJ and ULJ in the presence of vertical directional shear.

The analysis of wind fields at different altitudes is discussed in the following. The reference time will always be 18:00 UTC on November 12, two hours before the cyclone reaches the lowest sea level pressure. Figure 5.22 shows the wind speed and direction fields at 700, 500 and 300 hPa, obtained from the 9 Km grid spacing domain. The speed scale is the same for all three maps. Observing the field at 300 hPa we note the presence of two branches of the jet stream: one heading to the south and passing over the western Mediterranean, one heading to the north, positioned on the Adriatic Sea. Observing the fields at 500 and 700 hPa, one immediately observes the drop in wind speed, which in the area affected by the cyclone is around 20 m/s at both levels. So there is a strong intensity shear especially in the upper layers.

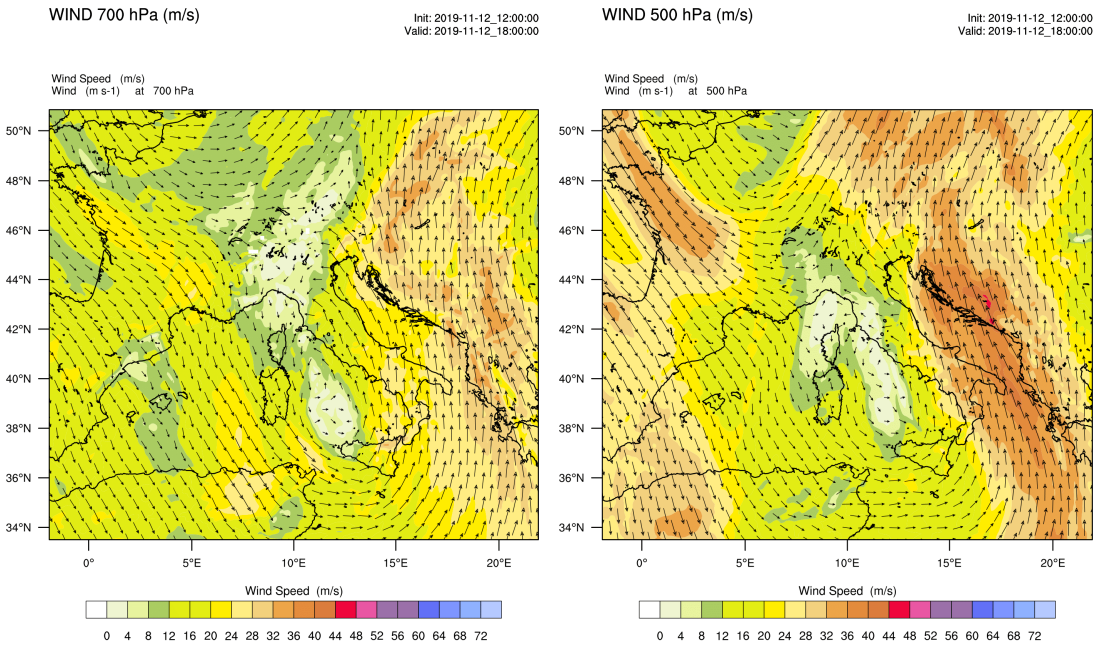

(a) *700 hPa* (b) *500 hPa*

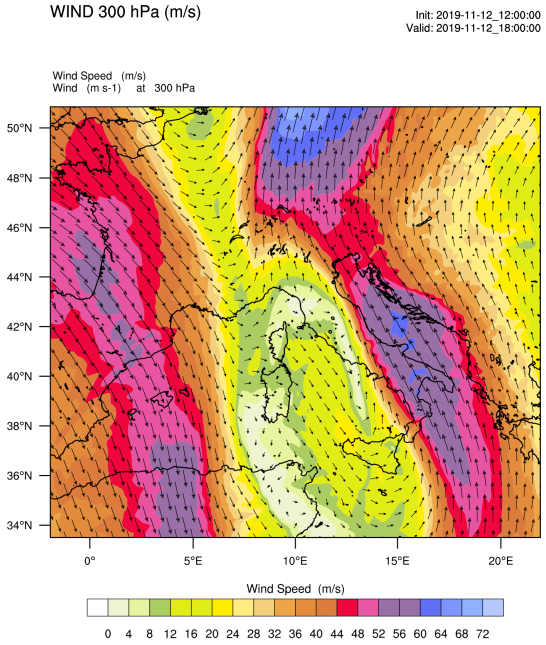

(c) *300 hPa*

Figure 5.22: *Wind speed and direction at* a) *700 hPa,* b) *500 hPa and* c) *300 hPa - 1212 run, 9 Km grid spacing domain forecast.*

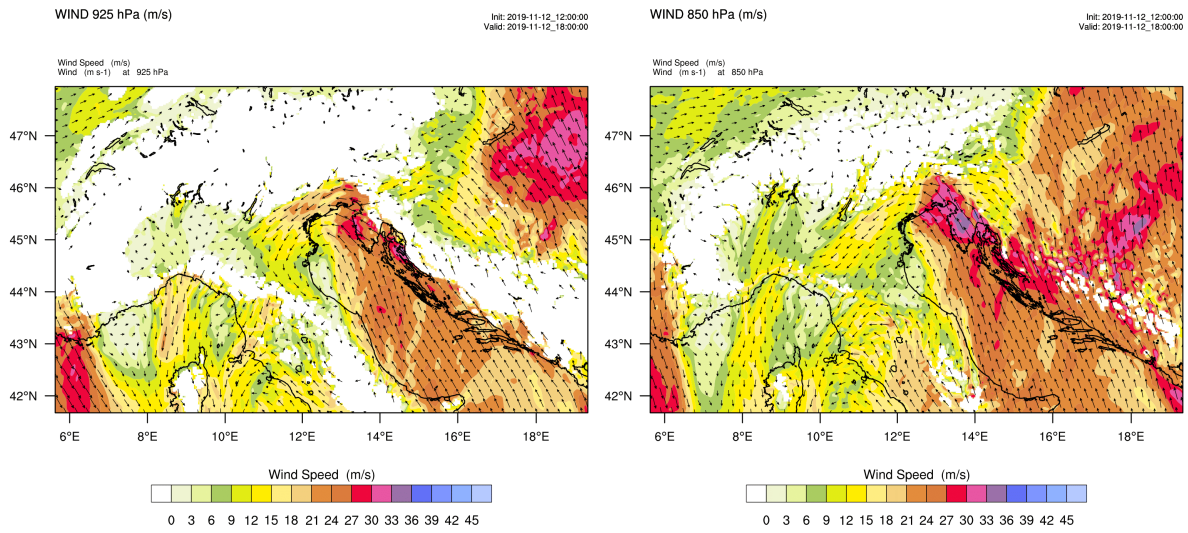

(a) *925 hPa* (b) *850 hPa*

Figure 5.23: *Wind speed and direction at* a) *925 hPa and* b) *850 hPa - 1212 run, 3 Km grid spacing domain forecast.*

On the other hand, observing the maps in figure 5.23 relative to the wind speed and direction fields at 925 and 850 hPa, obtained from the 3 Km grid spacing domain, we note the presence of a LLJ on the most northeastern part of the Adriatic, close to the border between Italy and Slovenia. Note the Sirocco winds in the Adriatic and the rotation around the pressure minimum, with even stronger Bora winds - especially at 925 hPa - on the Triveneto.

Summing up, an ULJ at 300 hPa is found, so that conditions favourable to the cyclone intensification were present in the left side exit area. Furthermore, strong Bora and Sirocco winds in the lower layers converge on the northern Adriatic (also note the configuration at sea level in figure 5.3(b)), creating a favourable situation for the development of positive (cyclonic) vorticity in the lower levels.

Vertical velocity

Vertical velocity provides informations not only on the presence but also on the intensity and elevation of any convective structure.

In figure 5.24 the vertical velocity and wind speed and direction fields are shown, obtained from the 1 Km grid spacing domain, at 850, 700 and 500 hPa. Analysing the maps and remembering that the cyclone at 18:00 UTC in this simulation is positioned off

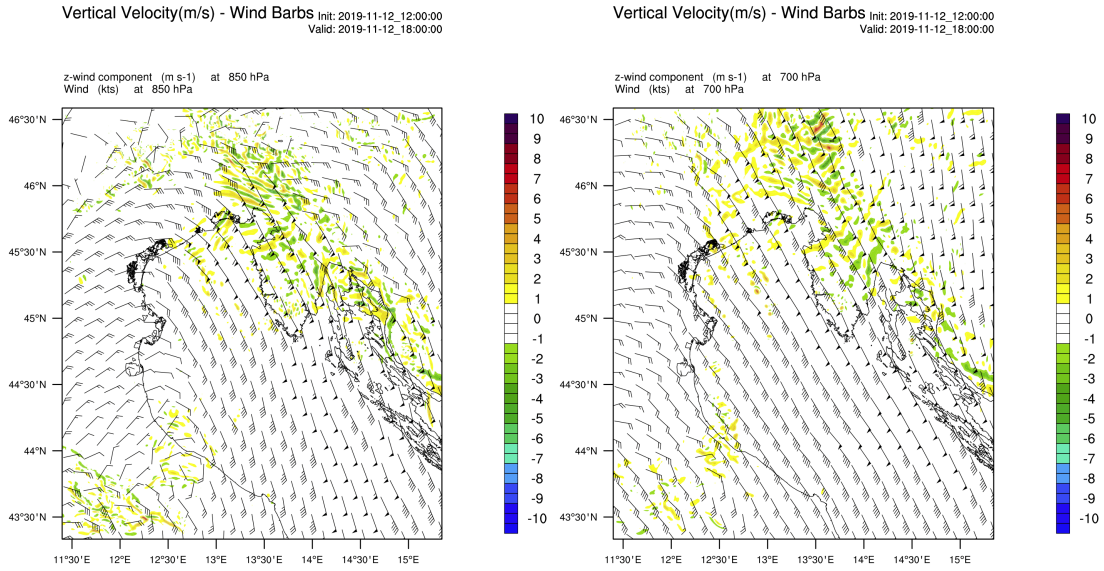

(a) *850 hPa* (b) *700 hPa*

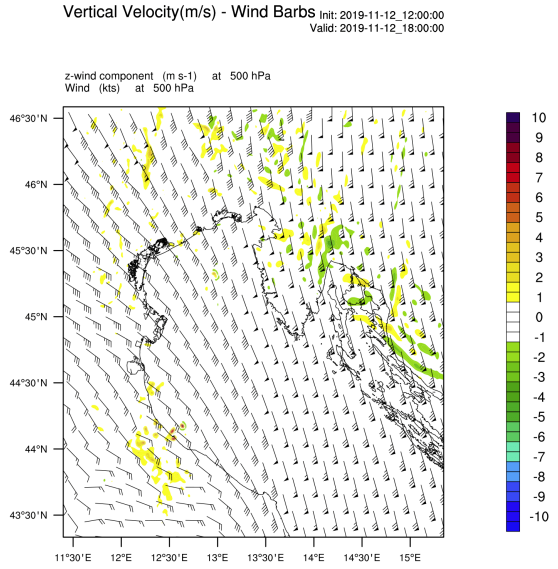

(c) *500 hPa*

Figure 5.24: *Vertical velocity (m/s) at* a) *850 hPa,* b) *700 hPa and* c) *500 hPa - 1212 run, 1 Km grid spacing domain forecast.*

the Po river delta (figure 5.3), we note the scarce presence of weakly positive vertical velocities (updrafts) associated with convective structures, especially near the cyclone. Positive vertical velocities near the cyclone are found mainly on the northern Adriatic, north of the cyclone center, but mainly below 700 hPa, so it is an indication of shallow and weak convection.

In conclusion, convection appears limited and does not seem to play a role in the intensification of the cyclone.

Liquid water mixing ratio

Another major tracer of convection is the liquid water mixing ratio (LWMR). It is defined as the ratio of the mass of liquid water to the mass of dry air in a unit volume of air. The LWMR helps to identify the cloud type, e.g. lower values - around 0.00003 Kg/Kg - identify cirrus clouds, while high values - over 0.001 Kg/Kg - identify cumulonimbus clouds (Thompson, 2007).

In figure 5.25 the LWMR fields at 850, 700 and 500 hPa are shown. Again, one can see that clouds are mainly limited below 700 hPa, suggesting that convection is very weak and shallow.

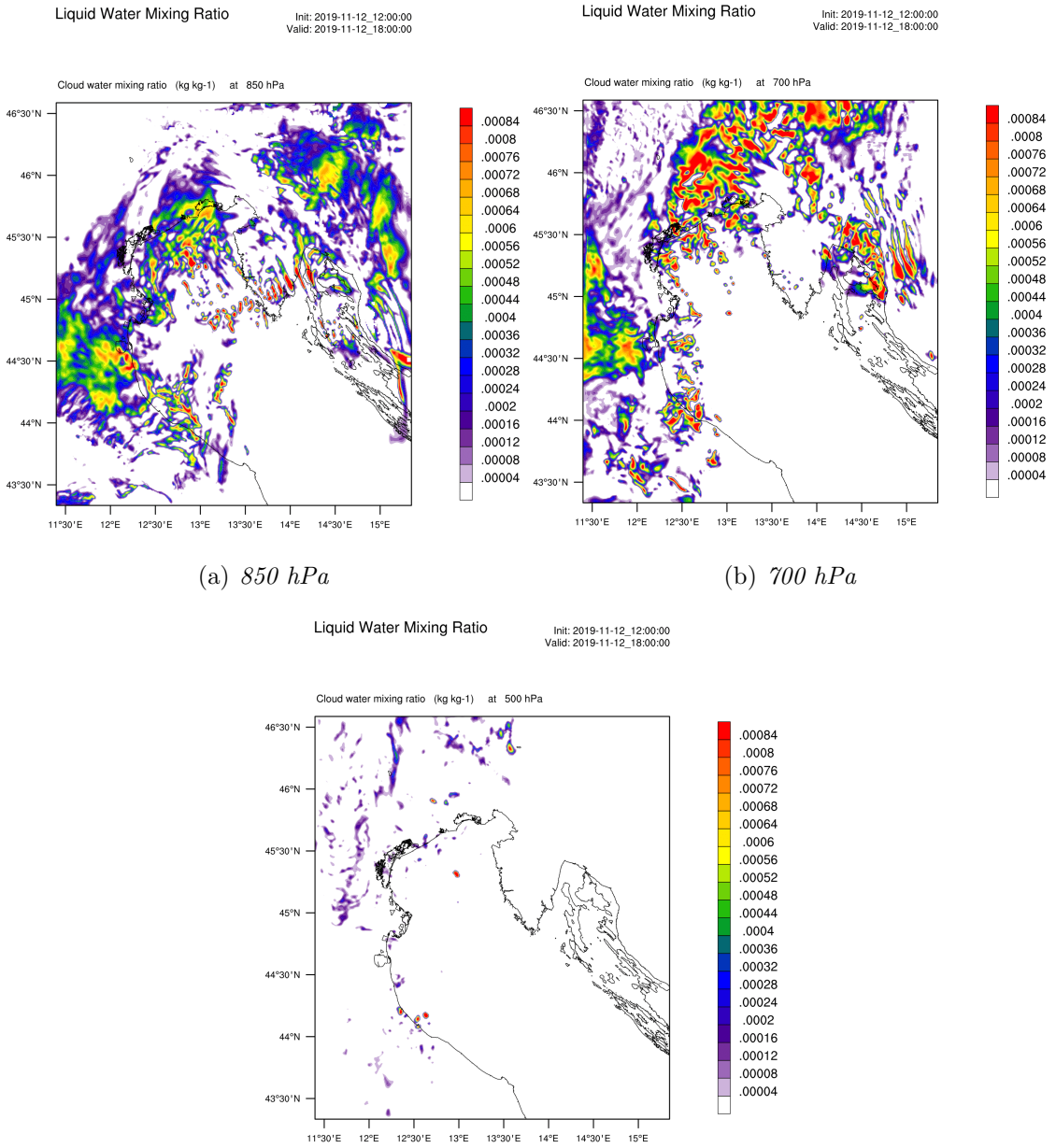

(a) *850 hPa* (b) *700 hPa*

(c) *500 hPa*

Figure 5.25: *Liquid water mixing ratio ($KgKg^{-1}$) at* a) *850 hPa,* b) *700 hPa and* c) *500 hPa - 1212 run, 1 Km grid spacing domain forecast.*

5.6.2 Atmospheric cross sections and soundings

To further analyse the convection simulated by the 1212 run before the cyclone reaches the time of maximum depth, some meteorological fields are analysed in the cross section, whose geographical position is described by the red line in the map in figure 5.26. The cross section analyses the fields relative to 19:00 UTC, one hour before the minimum sea level pressure value was recorded. The center of the cross section (filled red circle) is positioned at the point of maximum vertical velocity in the 1 Km grid spacing domain at that time, while the orientation of the cross section is parallel to the main wind direction.

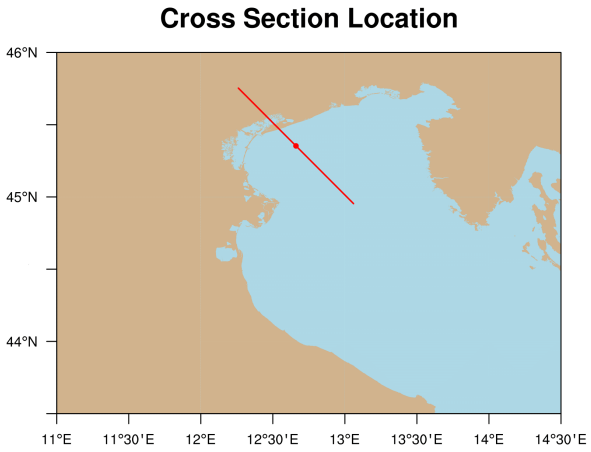

Figure 5.26: *Cross section location on map, centered on the vertical speed maximum (filled red circle).*

Before moving on to the cross section analysis, the skew-T diagram is drawn at the point of maximum vertical velocity. The sounding, in figure 5.27, reports information on the state of the atmosphere at all the levels interpolated by the model, from the surface up to the altitude of 100 hPa. The black line corresponds to the state curve of the environment (air temperature curve), while the blue line is associated with the dew point temperature. The solid green lines are the saturated adiabatics, the gray lines at 45° inclination - bottom right to top left in the graph - are the dry adiabatics, the gray lines at 45° inclination - bottom left to top right in the graph - are the isotherms, the horizontal gray lines are the isobars, while the dashed green lines correspond to the lines with constant mixing ratio. The wind barbs on the right give information on the wind direction and speed. In this situation, the overlap between the dew point curve and the state curve can be seen, reflecting the saturation conditions in that point.

So the presence of a cloud with a base of 950 hPa and a top around 500 hPa can be noted. This can be associated to shallow convection, as the saturation is confined below 500 hPa and does not approach the tropopause. Furthermore, there is no CAPE, one may suppose that it has already been removed previously during convection. There is a layer of thermal inversion near the ground, the reason of which can be probably attributed to the Bora wind in that layer, which drags colder air with it. Above 950 hPa, the rotation of the wind to Sirocco can be identified.

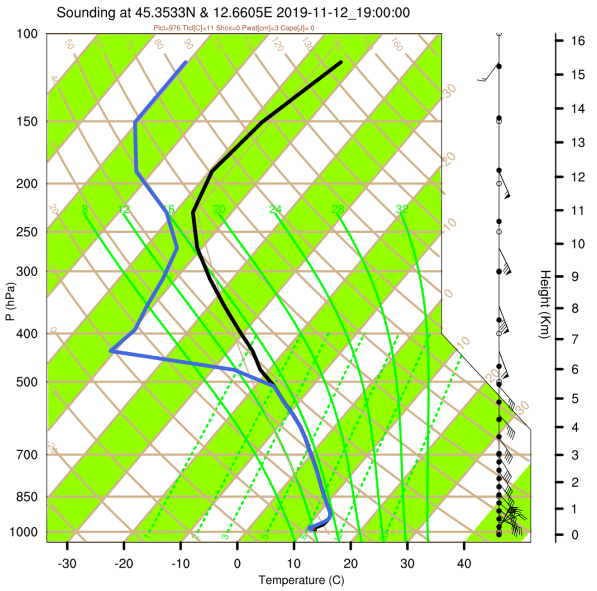

Figure 5.27: *Skew-T diagram on the vertical velocity maximum simulated for 19:00 UTC of November 12, 2019 - 1212 run.*

Moving on to the cross section analysis, some fields are shown in figure 5.28. The fields of wind direction and speed (figure 5.28(a)), of equivalent potential temperature (figure 5.28(b)), of vertical velocity (figure 5.28(c)) and liquid water mixing ratio (figure 5.28(d)) have been processed. From the wind map in figure 5.28(a) we can observe the Sirocco everywhere in the map above 850 hPa, with speeds just above 20 m/s. Beyond 450 hPa the presence of the jet stream is evident, reaching maximum speeds of up to 50 m/s near the tropopause. In the lower levels, on the other hand, we observe the rotation of the wind to the Northwest near the point of maximum vertical speed. The northern part of the lower layers of the cross section is affected by the Bora winds, which carry colder and drier air, as can be seen from the θ_e field in figure 5.28(b). This air is observed with values of θ_e slightly higher than 300 K over which warmer and humid air flows, carried by the Sirocco (θ_e higher than 320 K). Layers of colder and drier air can also be identified at upper levels and are progressively eroded by convection.

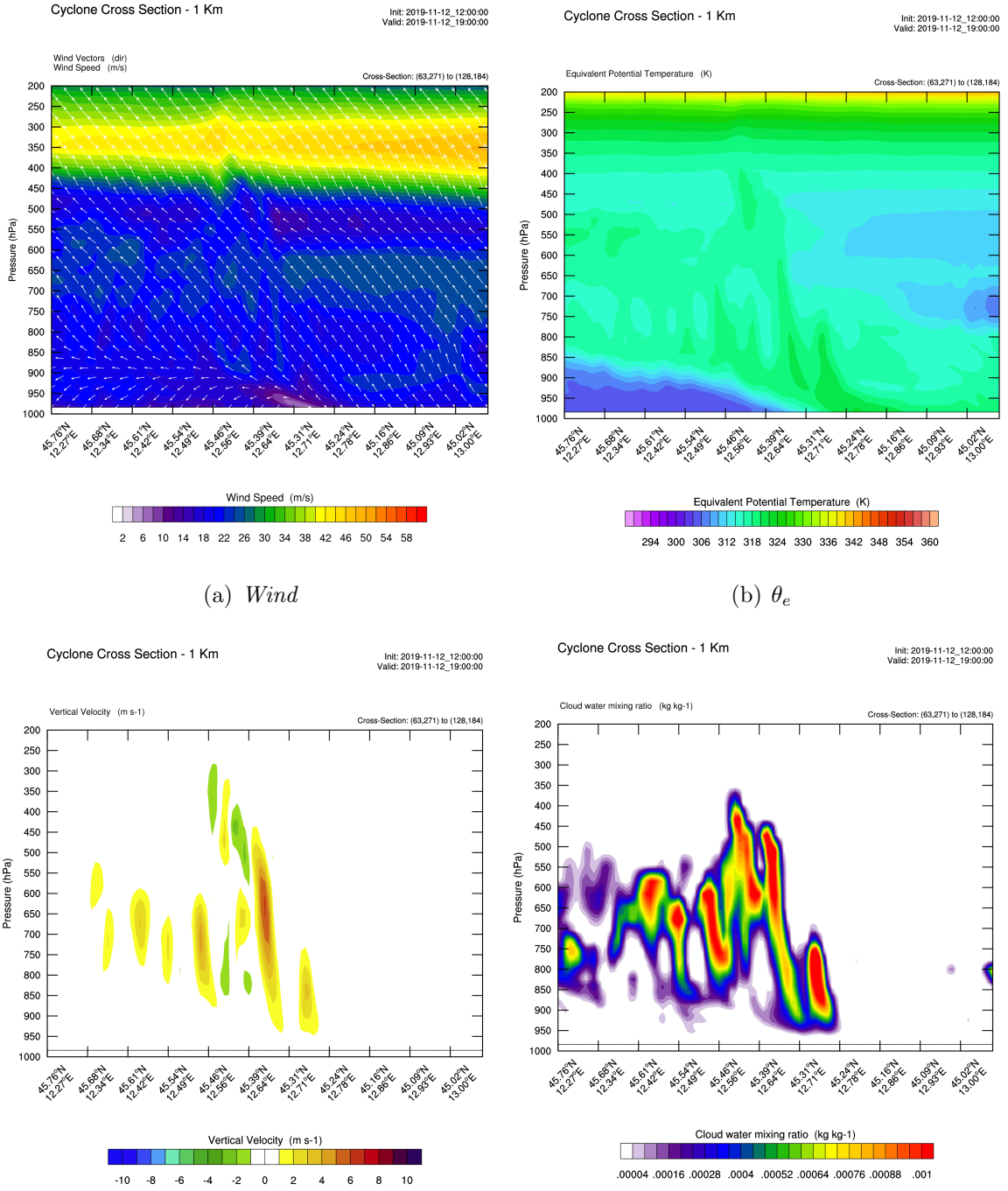

(a) *Wind* (b) θ_e

(c) *Vertical velocity* (d) *LWMR*

Figure 5.28: *Cross sections of fields:* a) *wind speed and direction,* b) *equivalent potential temperature,* c) *vertical velocity and* d) *liquid water mixing ratio - 1212 run, 1 Km grid spacing domain run.*

In fact, convective cells are evident in the center of the figure, with the warmer and humid air being pushed upwards above the colder low level air (figure 5.28(c)). Such convective structures show rather modest vertical speeds, with maximum values of the order of 8 m/s.

From this analysis we understand more about the causes that lead to the development of the (weak) convection. The presence of cold air near the ground, which plays the role of an obstacle to the incoming moist and warm airflow, and the colder and drier air layer at upper altitude favour the development of convection, which however remains rather weak and localized. Figure 5.28(d) relative to the LWMR confirms the presence of some clouds due to this uplift mechanism.

5.6.3 Venice sounding evolution

Skew-T diagrams were drawn up in the geographical coordinate point that corresponds to the city centre of Venice, with the aim of better observing how the atmospheric condition changes with the passage of the cyclone.

Figure 5.24 shows the soundings processed at three crucial times: at 18:00 UTC (figure 5.29(a)), at 20:30 UTC (figure 5.29(b)) and at 22:00 UTC (figure 5.29(c)), respectively before, during and after the passage of the cyclone. Before the passage a thermal inversion in the lower layers can be noted, with cold air on the ground carried by the Bora winds; during the passage we see the rotation of the low-level wind to Sirocco and the generation of CAPE (655 J/Kg), after the cold air near the ground has been removed; immediately after the passage of the cyclone we observe the entry of southwesterly winds on the ground, cooler and drier, which stabilizes the atmosphere again.

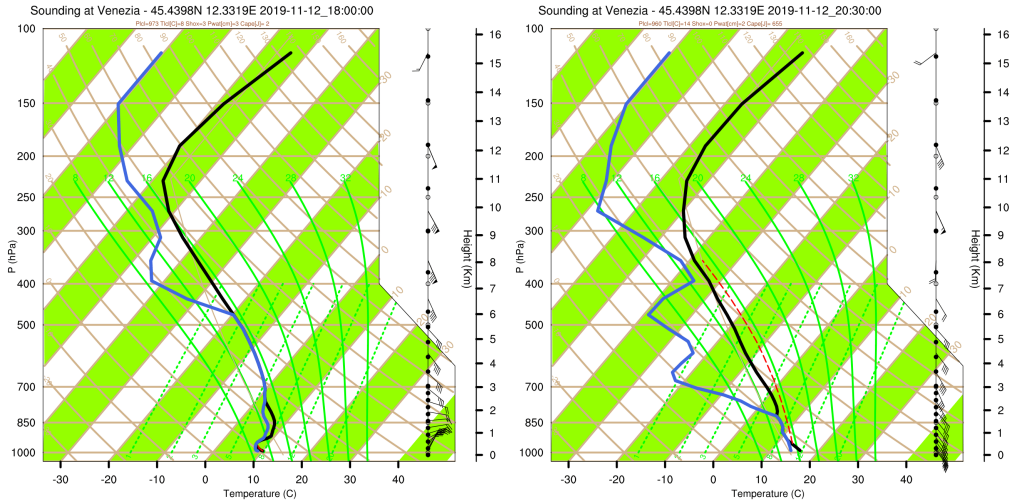

(a) *18:00 UTC* (b) *20:30 UTC*

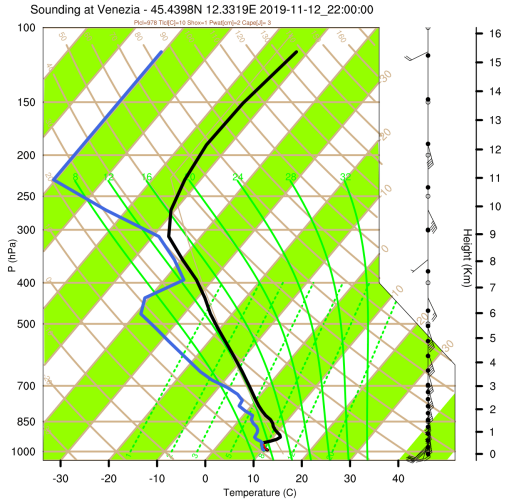

(c) *22:00 UTC*

Figure 5.29: *Skew-T diagram forecasted on Venice at* a) *18:00 UTC,* b) *20:30 UTC and* c) *22:00 UTC of November 12, 2019 - 1212 run.*

5.7 Vorticity analysis

Vorticity plays a very important role in cyclogenesis. It is mathematically defined in a flow as the curl of the velocity, i.e. it represents the tendency of the flow to rotate. In meteorology it is useful to study relative vorticity, i.e. vorticity without the contribution of the Coriolis force (representing the spinning motion created by the Earth's rotation). So we define relative vorticity as:

$$\zeta_r = \frac{\partial v}{\partial x} - \frac{\partial u}{\partial y} \tag{5.2}$$

where u and v are the horizontal Cartesian components of the velocity of a fluid. The unit of measurement is s^{-1}. The absolute vorticity is defined instead as:

$$\zeta_a = \frac{\partial v}{\partial x} - \frac{\partial u}{\partial y} + f \tag{5.3}$$

with f the Coriolis parameter.

Relative vorticity is the sum of two components: the shear vorticity, i.e. the rate of change of wind speed normal to the direction of flow, and the curvature velocity, i.e. the turning of the wind along a streamline. When the wind rotation is counterclockwise (in the Northern hemisphere) or the wind speed increases away from the center point of a trough, the relative vorticity increases. Therefore usually positive relative vorticity is associated with a cyclonic circulation.

The potential vorticity (PV) is a quantity that, following the motion of a particle, can only be varied by diabatic or frictional processes. It is defined, according to Ertel's formalization, as:

$$PV = \frac{\zeta_a \cdot \nabla\theta}{\rho} \tag{5.4}$$

where ζ_a is the absolute vorticity, θ is the potential temperature and ρ is the density. It is expressed in PV, where:

$$1PVU = \frac{10^{-6} \cdot K \cdot m^2}{Kg \cdot s} \tag{5.5}$$

The mean potential vorticity assumes values close to 0 in the lower and middle tropospheric layers and a maximum value of 1 PVU in the upper troposphere. Above it increases with altitude, assuming a value greater than 3 PVU in the lower stratosphere. This climatological distribution is often perturbed by positive anomalies, which can form during a tropopause fold that causes intrusion of stratospheric air at lower altitudes (Whitaker et al., 1988). The cyclonic circulation associated with the positive upper-level anomaly penetrates the troposphere and induces a weak cyclonic circulation near the surface (Hoskins et al., 1985), causing warm advection in the lower-eastern sides of the upper-level vorticity anomaly (Martin, 2013). This can induce a cyclonic circulation which then reinforces the upper-level positive anomaly, allowing mutual amplification and cyclogenesis (Gray and Dacre, 2006).

These properties of PV make it a useful tracer of the dynamics of the upper levels, therefore linked to what happens in the lower levels. For this reason relative vorticity at 950 hPa and the PV fields at 300 hPa will be analysed to understand their role in the deepening of the cyclone to explore the contribution from the upper and the lower layers respectively.

5.7.1 Relative vorticity

The analysis of the relative vorticity fields is based on the 950 hPa maps at 18:00 UTC of the 3 Km grid spacing domains of runs 1112, 1200 and 1212 (figure 5.30), in order to make a comparison between the predictions of the three control runs.

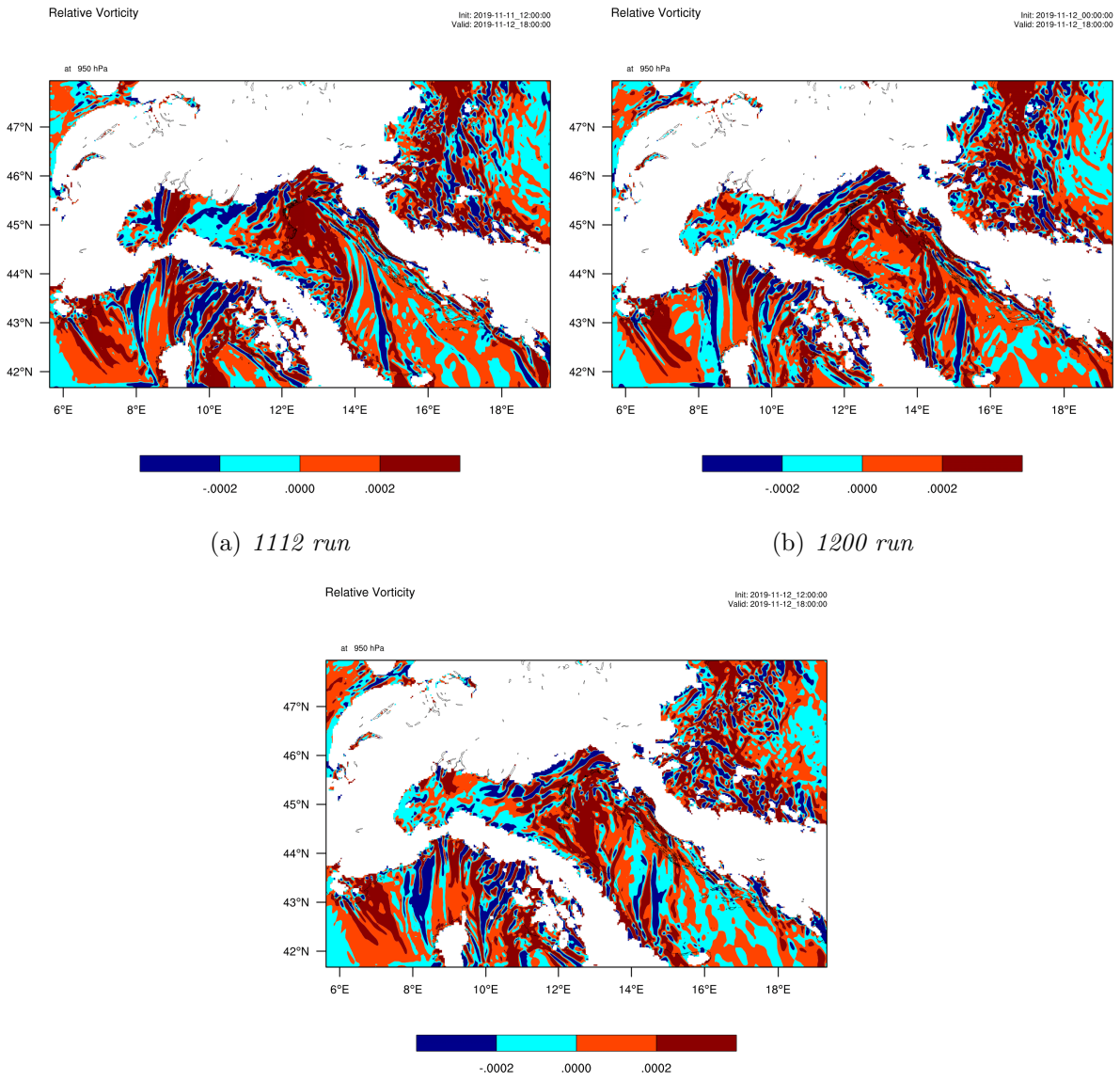

(a) *1112 run*

(b) *1200 run*

(c) *1212 run*

Figure 5.30: *Relative vorticity (s^{-1}) forecasted by* a) *1112 run,* b) *1200 run and* c) *1212 run for 18:00 UTC of November 12, 2019*

The light or dark red colour is associated with positive (cyclonic) vorticity, while the turquoise or blue colour corresponds to negative (anticyclonic) vorticity. Widespread areas of positive cyclonic vorticity are present in the Adriatic. However, differences among the three runs are noted in the positioning of the strongest positive vorticities, following

the positioning of the cyclone (see the trajectories in figure 5.12).

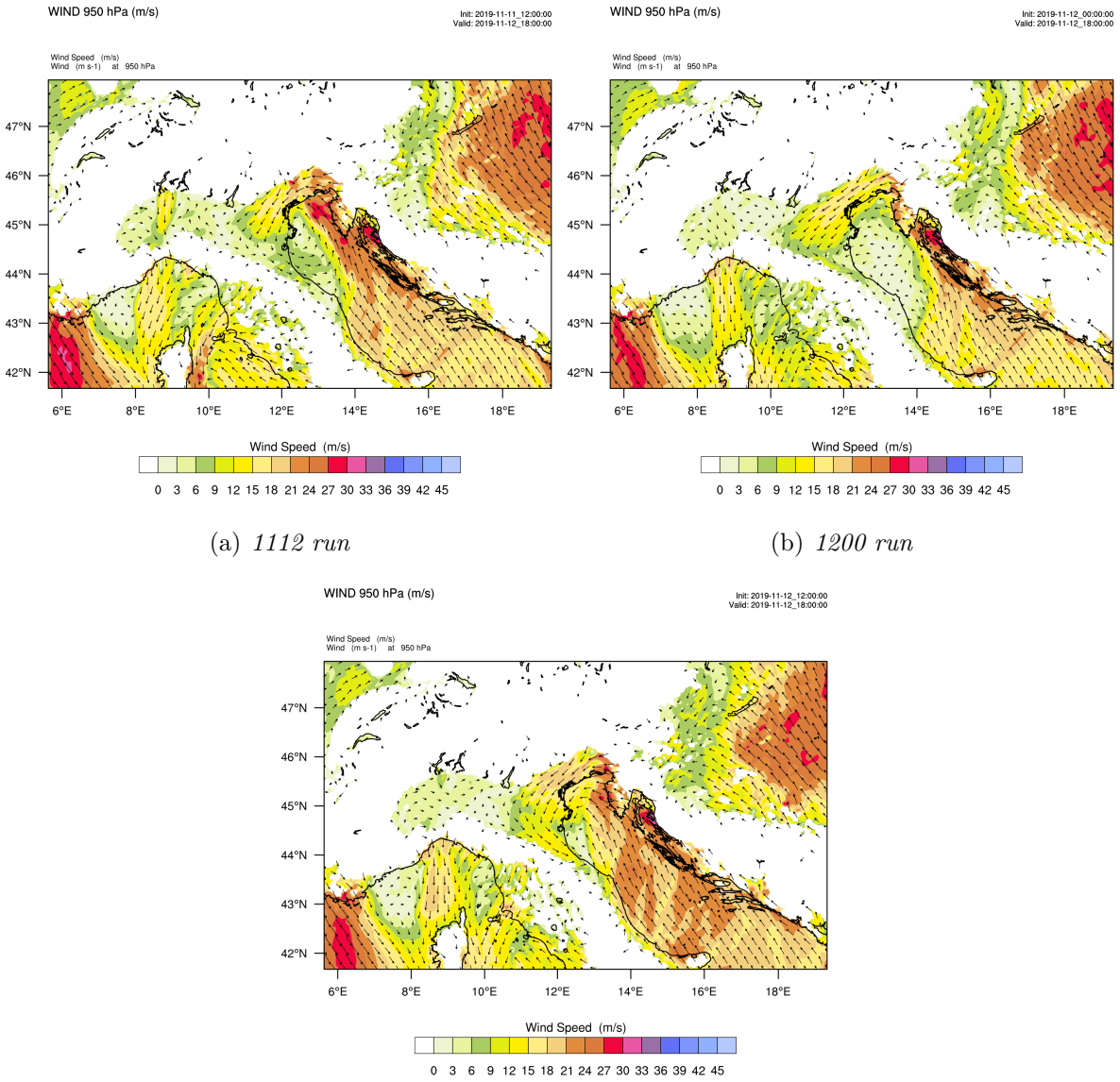

(a) *1112 run*

(b) *1200 run*

(c) *1212 run*

Figure 5.31: *Wind direction and speed at 950 hPa forecasted by* a) *1112 run,* b) *1200 run and* c) *1212 run for 18:00 UTC of November 12, 2019*

In fact, by analysing the wind speed and direction fields at 950 hPa in figure 5.31 the highest values of relative vorticity are found in the areas of convergence between the Bora and Sirocco winds, where the difference in direction and intensity is a source of

positive relative vorticity. One should consider that this environment was present before the development of the cyclone, due to the presence of Bora and Sirocco winds, so the cyclone found an environment favourable to its development before its transit in the northern Adriatic.

5.7.2 Potential vorticity

The potential vorticity fields at 300 hPa of the same three runs are compared.

The forecast for 20:00 UTC is analysed, the time when in the 1212 run (and in reality) the maximum depth of the cyclone was reached. In all three runs there is a strong potential vorticity advection that stretches from central Italy to the northeast of the Italian peninsula. However, there are several differences among them. Starting from the 1112 run (figure 5.32(a)), we can see two filaments of PV: a weak one that enters the Adriatic and the Venice lagoon, and a more intense one that remains confined to the mainland. In 1200 run (figure 5.32(b)), advection shows slightly lower PVU values, with the most intense part remaining on central Italy. The 1212 run (figure 5.32(c)) shows a very intense potential vorticity advection, slightly more eastern and stronger than the other two runs, directed exactly toward the area affected by the cyclone transit.

Given the strong dependence of the simulations on the PV positioning and the secondary role that surface heat and moisture fluxes and convection play, the dynamics of the upper and lower levels, with the intense potential and relative vorticity advection respectively, are probably the main factors responsible for the strong intensification of the cyclone.

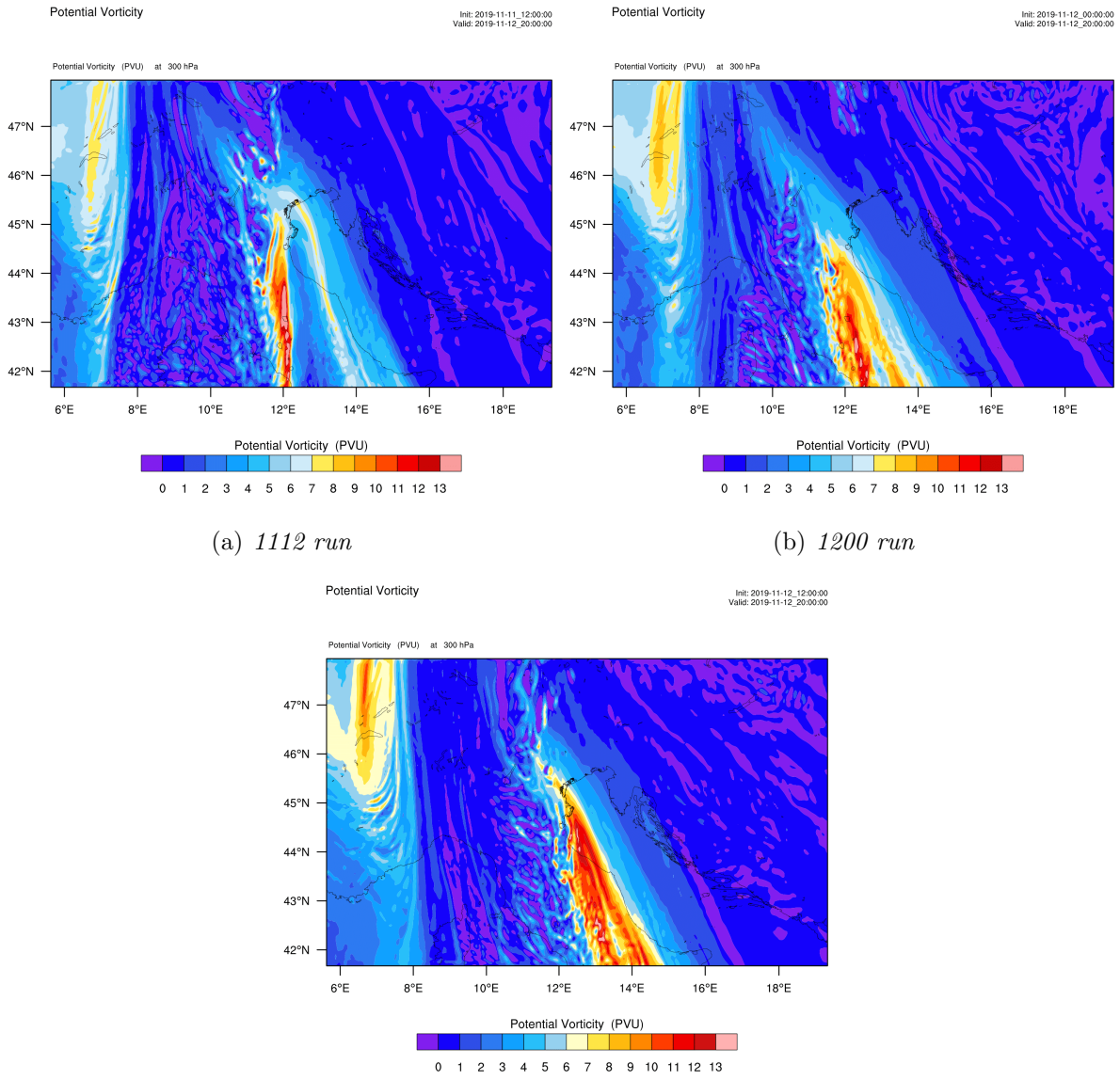

(a) *1112 run*

(b) *1200 run*

(c) *1212 run*

Figure 5.32: *Potential vorticity (PVU) forecasted by* a) *1112 run,* b) *1200 run and* c) *1212 run for 20:00 UTC of November 12, 2019*

Chapter 6

Conclusions

The dynamics that led to the genesis and deepening of the cyclone that hit the Venetian lagoon on November 12, 2019, causing severe wind gusts and an exceptional high tide (CPSM et al., 2020), are certainly particular and rare due to the combination of various factors, concerning both the sea and the atmosphere.

The simulations performed with the WRF-ARW model allow us to understand more about the predictability limits that may occur in the simulation of the genesis and deepening of a cyclone of this type. The 1212 run, initialised at 12:00 UTC of November 12, is accurate both in terms of trajectory and timing, while it misses the fine details of the depth of the cyclone, which was underestimated by a few hPa. The 1112 run (initialised at 12:00 UTC of November 11) correctly predicts the cyclone track at the beginning, supported by a correct transport of warm and humid air from the southern Adriatic. However, the dynamics are excessively rapid, as the cyclone made landfall too early, rapidly losing its strength. The 1200 run (initialised at 00:00 UTC of November 12) simulates a trajectory too close to the Croatian coasts, which affects the evolution of the cyclone, resulting in a weak depression. The 1212 run turns out to be the closest to the observations, predicting the timing and trajectory of the cyclone in an excellent way, very close to the observations, although underestimating its strength.

Subsequently, the cyclone cyclogenesis and deepening mechanism were investigated, especially in light of the warm core structure that it assumes in the lower layers. For this purpose the role of heat and moisture surface fluxes has been studied, carrying out three other simulations (No Fluxes - runs) in which they were switched off. The simulations show that the results do not undergo any significant variation. This is an important result, as it suggests that the cyclonic structure is different compared to, for example, tropical-like cyclones or medicanes, whose intensification mechanism is based on the synergy of sea surface fluxes and latent heat release due to convection (Miglietta and Rotunno, 2019), but also to intense cold-core Mediterranean extra-tropical cyclones, e.g. Vaia storm (Davolio et al., 2020). The low-level warm core seems to be due to the warm and moist tongue moving along the Adriatic and it is not an effect of the dynamics related to the cyclone.

Additional simulations have been undertaken by explicitly solving convection not only in the smaller domain, but also in the intermediate and larger domains respectively (CP100 and CP000), showing that output fields are only marginally affected. The minimum sea level pressure obtained in these runs is very similar to that obtained in the other simulations. Also, the fact that the cyclone depth does not change moving to higher resolution but remains nearly constant, is an indication that convection has no effect on the cyclone intensification (a higher resolution domain should resolve better small-scale convection). This unexpected result is consistent with the outputs obtained from different model runs, thus appearing to be robust and independent of the model (see: https://www.isac.cnr.it/dinamica/projects/forecasts/bolam/).

Then, analysing convection in the 1212 run one may note that the model does not reproduce intense and deep convection, but rather scattered and shallow cells, confirming that convection also plays a minor role in the development of the cyclone.

Afterwards, the potential vorticity at the tropopause and the relative vorticity at lower levels fields were analyzed. In the former case, a strong potential vorticity advection

is apparent over the Venice lagoon at the time of maximum cyclone intensification, with a PV streamer elongated from central Italy to the northern Adriatic. The interaction of this feature with warmer and humid low-level air (identified by higher values of equivalent potential temperature), seems to be the main mechanism of development of the cyclonic structure, which appeared also favoured by the transition from the Bora to Sirocco winds at the lower layers, determining an environment with high low-level relative vorticity.

The differences among the three control runs in the representation of upper level forcing, i.e. potential vorticity advection, could be the reason for the different evolution of the cyclone simulated by the WRF model. Since similar problems came out for other model simulations (see: https://www.isac.cnr.it/dinamica/projects/forecasts/bolam/), one may conclude that the errors can be associated with large-scale forcings, i.e. initial and boundary conditions, supplied by the GFS-model.

In conclusion, the triggering came from a baroclinic instability process, typical of extra-tropical cyclones, but at much smaller scale, producing a mesoscale cyclonic structure. This type of small scale Mediterranean cyclones is rather unusual: that may be related to the conformation of the coastline and to the orography of the area in which they grow, as in the eastern Mediterranean (Alpert et al., 1999), or they are appear as small-scale Medicanes (Moscatello et al., 2008; Ricchi et al., 2019). The path taken by this cyclone is also rare and leaves aside the climatology of cyclones usually observed in the Adriatic. According to the classification by Horvath et al. (2008), this case differentiates from both Adriatic cyclones of B-I type, with cyclogenesis occurring in the north Adriatic, followed by a fast movement towards the southeast along the basin, or of type B-II, with cyclogenesis occurring in the central Adriatic in the lee of the Apennines followed by a rapid eastward shift. For what concerns cyclogenesis, the cyclone may belong to category B-II; however, its movement and the subsequent development do not fall into any of these categories, resulting in a unique event.

From this case study we understand the importance of the initial conditions provided

to limited area models, whose accuracy still remains one of the open problems of meteorological modeling. A great help may come from mesoscale data assimilation, the use and optimization of which could significantly improve short-term predictions. Furthermore, the correct simulation of convection remains one of the most difficult but fundamental challenges of the future of research in the field, whose relevance can be appreciated given the continuous increase in the intensity of extreme atmospheric phenomena due to global warming. Their correct prediction is of fundamental importance, also in terms of impact: the exact location of the cyclone may dramatically affect sensitive areas such as the Venice lagoon, where a variation of even a few kilometers in the positioning of such a small cyclone can completely change the consequent effects on the flooding of the city.

Acronyms

ASCII American Standard Code for Information Interchange

BOLAM Bologna Limited Area Model

C3S Copernicus Climate Change Service

CAPE Convective Available Potential Energy

CCN Cloud Condensation Nucleus

CDS Climate Data Store

CIN Convective Inhibition Energy

CNR Consiglio Nazionale delle Ricerche

COSMO Consortium for Small-scale Modeling

CPSM Centro Previsioni e Segnalazioni Maree

ECMWF European Centre for Medium-range Weather Forecasts

ERA5 ECWWF Reanalysis 5^{th} generation

EUMETSAT European Organization for the Exploitation of Meteorological Satellites

FAA Federal Aviation Administration

FDM Finite Difference Method

FV3 Finite Volume Cubed Sphere

GCM General Circulation Model

GFS Global Forecast System

GIS Geographic Information System

GRIB General Regularly-distributed Information in Binary form

HDF Hierarchical Data Format

HRV High Resolution Visible

IR InfraRed

ISAC Istituto di Scienze dell'Atmosfera e del Clima

ISMAR Istituto di Scienze del Mare

ISPRA Istituto Superiore per la Ricerca e la Protezione Ambientale

KML Keyhole Markup Language

LAM Limited Area Model

LLJ Low Level Jet

LSM Land Surface Model

LWMR Liquid Water Mixing Ratio

MATLAB MATrix LABoratory

NCAR National Center for Atmospheric Researche

NetCDF Network Common Data Form

NF No-Fluxes simulations

NIR Near-IR

NMM Nonhydrostatic Mesoscale WRF Model

NWP Numerical Weather Prediction

NWS National Weather Service

PBL Planetary Boudary Layer

PV Potential Vorticity

SEVIRI Spinning Enhanced Visible and InfraRed Imager

SLP Sea Level Pressure

SST Sea Surface Temperature

ULJ Upper Level Jet

USA United States of America

UTC Universal Time Coordinated

WPS WRF Pre-processing System

WRF-ARW Weather Research and Forecasting model-Advanced Research WRF

Bibliography

Alpert, P., Tsidulko, M., and Itzigsohn, D. (1999). A shallow, short-lived meso-β cyclone over the Gulf of Antalya, eastern Mediterranean. *Tellus A*, 51(2):249–262. https://doi.org/10.3402/tellusa.v51i2.12319.

Aminou, D. (2002). MSG's SEVIRI instrument. *ESA Bulletin(0376-4265)*, (111):15–17.

Beebe, R. G. and Bates, F. C. (1955). A mechanism for assisting in the release of convective instability. *Monthly Weather Review*, 83(1):1–10. https://doi.org/10.1175/1520-0493(1955)083¡0001:AMFAIT¿2.0.CO;2.

Cavaleri, L., Bajo, M., Barbariol, F., Bastianini, M., Benetazzo, A., Bertotti, L., Chiggiato, J., Ferrarin, C., Trincardi, F., and Umgiesser, G. (2020). The 2019 flooding of Venice and its implications for future predictions. *Oceanography, 33(1), 42-49*, 33(1):42–49. https://doi.org/10.5670/oceanog.2020.105.

Chang, E. K., Lee, S., and Swanson, K. L. (2002). Storm track dynamics. *Journal of climate*, 15(16):2163–2183. https://doi.org/10.1175/1520-0442(2002)015¡02163:STD¿2.0.CO;2.

Charney, J. G. (1950). Progress in dynamic meteorology. *Bulletin of the American Meteorological Society*, 31(7):231–236. https://doi.org/10.1175/1520-0477-31.7.231.

CNR-ISAC (2019). Cluster Beowulf for parallel computing LECCE.

CPSM, ISPRA, and CNR (2020). Novembre 2019. Un mese di maree eccezionali. Dinamica e anomalia dell'evento del 12 Novembre 2019. *Report ISPRA, CPSM, CNR-ISMAR*.

Davolio, S., Della Fera, S., Laviola, S., Miglietta, M. M., and Levizzani, V. (2020). Heavy precipitation over Italy from the Mediterranean storm "Vaia" in October 2018: Assessing the role of an atmospheric river. *Monthly Weather Review*, 148(9):3571–3588. https://doi.org/10.1175/MWR-D-20-0021.1.

Dudhia, J. (1989). Numerical study of convection observed during the winter monsoon experiment using a mesoscale two-dimensional model. *Journal of Atmospheric Sciences*, 46(20):3077–3107. https://doi.org/10.1175/1520-0469(1989)046¡3077:NSOCOD¿2.0.CO;2.

EMC-NCEP-NOAA (2021). The Global Forecast System (GFS).

EUMETSAT (2021). EUMETSAT Data Centre.

Ferla, M., Cordella, M., Michielli, L., and Rusconi, A. (2007). Long-term variations on sea level and tidal regime in the lagoon of Venice. *Estuarine, Coastal and Shelf Science*, 75(1-2):214–222. https://doi.org/10.1016/j.ecss.2007.03.037.

Gray, S. L. and Dacre, H. F. (2006). Classifying dynamical forcing mechanisms using a climatology of extratropical cyclones. *Quarterly Journal of the Royal Meteorological Society*, 132(617):1119–1137. https://doi.org/10.1256/qj.05.69.

Harris, D. L. (1963). *Characteristics of the hurricane storm surge*. Number 48. Department of Commerce, Weather Bureau.

Hersbach, H., Bell, B., Berrisford, P., Biavati, G., Horányi, A., Muñoz, S. J., Nicolas, J., Peubey, C., Radu, R., Rozum, I., Schepers, D., Simmons, A., Soci, C., Dee, D., and Thépaut, J.-N. (2018). Era5 hourly data on single levels from 1979 to present.

Copernicus Climate Change Service (C3S) Climate Data Store (CDS). (Accessed on 18-09-2021), 10.24381/cds.adbb2d47.

Holton, J. R. (1992). *An introduction to dynamic meteorology*, volume 48. Elsevier Academic Press, 3rd edition.

Holton, J. R. (2004). *An introduction to dynamic meteorology*, volume 88. Elsevier Academic Press, 4th edition.

Hong, S. Y., Noh, Y., and Dudhia, J. (2006). A new vertical diffusion package with an explicit treatment of entrainment processes. *Monthly Weather Review*, 134(9):2318–2341. https://doi.org/10.1175/MWR3199.1.

Horvath, K., Lin, Y. L., and Ivančan-Picek, B. (2008). Classification of cyclone tracks over the Apennines and the Adriatic Sea. *Monthly weather review*, 136(6):2210–2227. https://doi.org/10.1175/2007MWR2231.1.

Hoskins, B. J., McIntyre, M. E., and Robertson, A. W. (1985). On the use and significance of isentropic potential vorticity maps. *Quarterly Journal of the Royal Meteorological Society*, 111(470):877–946. https://doi.org/10.1002/qj.49711147002.

Jiménez, P. A., Dudhia, J., González-Rouco, J. F., Navarro, J., Montávez, J. P., and García-Bustamante, E. (2012). A revised scheme for the WRF surface layer formulation. *Monthly Weather Review*, 140(3):898–918. https://doi.org/10.1175/MWR-D-11-00056.1.

Kain, J. S. (2004). The Kain–Fritsch convective parameterization: an update. *Journal of applied meteorology*, 43(1):170–181. https://doi.org/10.1175/1520-0450(2004)043¡0170:TKCPAU¿2.0.CO;2.

Martin, J. E. (2013). *Mid-latitude atmospheric dynamics: a first course.* John Wiley & Sons.

Miglietta, M. M. and Rotunno, R. (2019). Development mechanisms for Mediterranean tropical-like cyclones (medicanes). *Quarterly Journal of the Royal Meteorological Society*, 145(721):1444–1460. https://doi.org/10.1002/qj.3503.

Mlawer, E. J., Taubman, S. J., Brown, P. D., Iacono, M. J., and Clough, S. A. (1997). Radiative transfer for inhomogeneous atmospheres: RRTM, a validated correlated-k model for the longwave. *Journal of applied meteorology*, 102(D14):16663–16682. https://doi.org/10.1029/97JD00237.

Moncrieff, M. W. and Miller, M. J. (1976). The dynamics and simulation of tropical cumulonimbus and squall lines. *Quarterly Journal of the Royal Meteorological Society*, 102(432):373–394. https://doi.org/10.1002/qj.49710243208.

Moscatello, A., Miglietta, M. M., and Rotunno, R. (2008). Observational analysis of a Mediterranean'hurricane'over south-eastern Italy. *Weather*, 63(10):306. https://doi.org/10.1002/wea.231.

NASA (2018). Extratropical cyclone - Suomi NPP Reflectance.

NCEP-NOAA (2021a). Climate Data Store.

NCEP-NOAA (2021b). NCEP Products Inventory.

NOAA (2005). Hurricane Katrina.

of Atmospheric Sciences (DAS) University of Illinois, D. (2010). Occluded Front.

Reardon, K. (2016).

Ricchi, A., Miglietta, M. M., Bonaldo, D., Cioni, G., Rizza, U., and Carniel, S. (2019). Multi-physics ensemble versus atmosphere-ocean coupled model simulations for a tropical-like cyclone in the Mediterranean Sea. *Atmosphere*, 10(4):202. https://doi.org/10.3390/atmos10040202.

Riehl, H., La Seur, N. E., Badner, J., Hovde, J. E., Means, L. L., and Palmer, W. C. (1952). Forecasting in Middle Latitudes. pages 1–80.

Rio, C., Del Genio, A. D., and Hourdin, F. (2019). Ongoing breakthroughs in convective parameterization. *Current Climate Change Reports*, 5(2):95–111. https://doi.org/10.1007/s40641-019-00127-w.

Rizzetto, F. and Tosi, L. (2012). Rapid response of tidal channel networks to sea-level variations (Venice Lagoon, Italy). *Global and Planetary Change*, 92:191–197. https://doi.org/10.1016/j.gloplacha.2012.05.022.

Schmid, J. (2000). The SEVIRI instrument. In *Proceedings of the 2000 EUMETSAT meteorological satellite data user's conference, Bologna, Italy*, volume 29.

Sela, J. G. (1980). Spectral modeling at the National Meteorological Center. *Monthly Weather Review*, 108(9):1279–1292. https://doi.org/10.1175/1520-0493(1980)108¡1279:SMATNM¿2.0.CO;2.

Shuman, F. G. and Hovermale, J. B. (1968). An operational six-layer primitive equation model. *Journal of Applied Meteorology and Climatology*, 7(4):525–547. https://doi.org/10.1175/1520-0450(1968)007¡0525:AOSLPE¿2.0.CO;2.

Skamarock, W. C., Klemp, J. B., Dudhia, J., Gill, D. O., Liu, Z., Berner, J., Wang, W., Powers, J. G., Duda, M. G., Barker, D. M., et al. (2019). A description of the advanced research WRF model version 4. *National Center for Atmospheric Research: Boulder, CO, USA*, page 145.

Tewari, M., Chen, F., Wang, W., Dudhia, J., LeMone, M. A., Mitchell, K., Gayno, G., Wegiel, J., and Cuenca, R. H. (2004). Implementation and verification of the unified NOAH land surface model in the WRF model. volume 1115, pages 11–15.

Thompson, A. (2007). Simulating the adiabatic ascent of atmospheric air parcels using the cloud chamber. *Department of Meteorology, Penn State*, pages 121–123.

Thompson, G., Rasmussen, R. M., and Manning, K. (2004). Explicit forecasts of winter precipitation using an improved bulk microphysics scheme. Part I: Description and sensitivity analysis. *Monthly Weather Review*, 132(2):519–542. https://doi.org/10.1175/1520-0493(2004)132¡0519:EFOWPU¿2.0.CO;2.

UCAR/NCAR/CISL/VETS (2016). The NCAR Command Language (Version 6.6.2 [Software]).

Wallace, J. M. and Hobbs, P. V. (2006). *Atmospheric science: an introductory survey*. Elsevier.

Whitaker, J. S., Uccellini, L. W., and Brill, K. F. (1988). A model-based diagnostic study of the rapid development phase of the Presidents's Day cyclone. *Monthly Weather Review*, 116(11):2337–2365. https://doi.org/10.1175/1520-0493(1988)116¡2337:AMBDSO¿2.0.CO;2.

World Meteorological Organization WMO (1992). *International Meteorological Vocabulary*.

Yu, J. Y. (2019). Chapter 24: Tropical Cyclones.